SHELL MODEL HAMILTONIANS FOR THE STRUCTURE AND ELECTROMAGNETIC PROPERTIES OF N=50 ISOTONES

By

Jordan A. Purcell

A DISSERTATION

Submitted to
Michigan State University
in partial fulfillment of the requirements
for the degree of

Physics—Doctor of Philosophy

2025

ABSTRACT

Theorists appeal to a number of different models for describing a nucleus, depending on the phenomenology that they intend to investigate. This work focuses investigating the low-energy nuclear structure of semi-magic isotones with 50 neutrons, in particular their binding energies and excitation energies up to roughly 10 MeV. To this end, we implement the nuclear Shell Model, which utilizes a theory of configuration interactions (CI's) used to generate realistic wavefunctions. With these wavefunctions, one can calculate the observable properties of nuclei by considering overlaps with various operators. Our CI's are first constructed using valence-space in-medium similarity renormalization group (VS-IMSRG) methods by S.R. Stroberg's group at Notre Dame. These VS-IMSRG methods are used to generate one-, two-, and three-body interactions that are based on nucleon-nucleon potentials. These many-body interactions are renormalized to zero-, one-, and two-body interactions for a shell model valence space relevant to the nuclei considered in this thesis. The predictions of binding energies and excitation energies made with these renormalized ab initio interactions have a root-mean squared deviation (RMSD) of nearly one MeV compared to the experimental energy spectra.

When one has access to well-determined experimental data, one can leverage this to fit the two-body matrix elements (TBME's) and produce a more realistic Hamiltonian. These TBME's are highly correlated; one can make use of the singular value decomposition (SVD) method to produce linear combinations of parameters which are uncorrelated, and fit the most well-determined linear combinations of parameters to experiment. One can go further by sampling random batches of experimental data for fitting, and testing the RMSD for data that was not included in the fitting procedure to more rigorously determine the sweet spot in the bias-variance trade-off of the fit.

The SVD fitting method has been used successfully to create gold standard "universal" Hamiltonians in many model spaces, such as the sd model space orbitals $\{0d_{5/2}, 0d_{3/2}, 1s_{1/2}\}$, the fp model space $\{0f_{7/2}, 0f_{5/2}, 1p_{3/2}, 1p_{1/2}\}$, and the $jj44$ model space $\{0f_{5/2}, 1p_{3/2}, 1p_{1/2}, 0g_{9/2}\}$ (for protons and neutrons). This work focuses on the isotones of $N = 50$ in a model space that we call $\pi j4$ - denoting that we are dealing with an interaction applying to proton configurations in the

$j4$ set of orbits $\{0f_{5/2}, 1p_{3/2}, 1p_{1/2}, 0g_{9/2}\}$. We applied this method to different starting interactions, each obtained from different ab initio methods, and were able to diagnose how realistic the interactions produced from these different ab initio methods are. To this end, this thesis demonstrates the results of the first use of batch data sampling in an SVD fit of such Hamiltonians. The implemented sampling method is known as Monte Carlo Cross Validation (MCCV). The effective interaction produced from these methods, called p35-i3 [1], was able to reproduce the data from the known experimental energy spectra data to within a root-mean squared deviation of 150 keV. This interaction makes predictions for many unobserved states in all nuclei within the model space, including a prediction of the single-hole excited states of ^{99}In and the binding energy of the doubly magic ^{100}Sn.

In addition, the wavefunctions produced have allowed us to predict the electromagnetic properties of all nuclei in the $\pi j4$ model space. Here we present predictions of magnetic dipole moments and $B(M1)$ from the $O(M1)$ operator, as well as electric quadrupole moments and $B(E2)$ from the $O(E2)$ operator. We adopt an effective proton charge of $e_p = 1.8$ to account for the fact that our model space is truncated. We observe excellent agreement between the experiment and the p35-i3 theory for magnetic dipole moments and for electric quadrupole moments. In addition, we predict electromagnetic moments and transitions that have yet to be observed in experiment for each nucleus in our model space. These predictions serve as motivation for several new experiments, both on the neutron-rich side of the landscape toward ^{78}Ni and on the proton-rich side toward ^{100}Sn for which electromagnetic data are even more scarce than the energy spectra.

This thesis is dedicated to my parents Keith and Monica, and to my brothers Zac and Jon.
Your love, support, and encouragement of curiosity has made this journey possible for me.

ACKNOWLEDGMENTS

This thesis is the culmination of not only my own life efforts, but the support and guidance of too many individuals to properly credit. I want to thank my parents for providing me with every opportunity in life to explore and realize all the possible visions of the future before me. I could fill books with thanks to both of you, and this acknowledgment could only do a disservice. To my brothers, I thank them for their constant love, encouragement, and humor throughout our lives, I cherish every moment I have gotten to spend with you both. I would also like to thank my oldest friend Jessie Lotz for being so steadfast after almost 30 years of friendship and for accepting a weird kid like me as a friend from day one. To my partner, Chelsea Johnson, thank you for being a safe haven in the most challenging part of my life up to this point. You have encouraged such positive growth and grounded me when I was overwhelmed and despairing in the final days of my graduate studies.

In the academic and professional part of my life, I must thank Alex Brown. Your insight will never cease to amaze, and it has been an honor to be guided by you through my graduate studies. You have been patient, kind, encouraging, and a role model while the world was experiencing a once-in-a-century pandemic. I must also give thanks to Prof. Doug Schumacher at OSU. You introduced me to research in physics and have shown a balance between compassion and professionalism that is inspiring to me. Without the experience working with you and your advice, I would not have gone to graduate school. It is clear that I have been blessed with two advisors who truly care about their students.

Finally, I give thanks to my friends from all parts of my life. My pre-college years were heavily defined by my friendships with Jessie, Nick Fox, and Joel Redick - thank you three for the late night shenanigans out on old country roads. My peers and I collectively came together and made passionate physicists out of one another. We knew we could challenge each other safely and respectfully, and we all learned together from our own respective strengths. These bonds will last our lives, and I will always see our dynamic as a standard of excellence in community building. Lastly, thanks to my cat Miles "Tails" Prower for being the ultimate sidekick and aviation genius.

TABLE OF CONTENTS

LIST OF TABLES

LIST OF FIGURES

LIST OF ABBREVIATIONS

CI	Configuration Interactions
DWBA	Distorted-Wave Born Approximation
ENSDF	Evaluated Nuclear Structure Data File
FRIB	Facility for Rare Isotope Beams
HFB	Hartree-Fock-Bogoliubov
IMSRG	In-Medium Similarity Renormalization Group
LDM	Liquid Drop Model
MCCV	Monte Carlo Cross-Validation
NNDC	National Nuclear Data Center
OBTD	One-Body Transition Density
RMSD	Root-Mean-Squared Deviation
SEMF	Semi-Empirical Mass Formula
SPE	Single-Particle Energy
SPME	Single-Particle Matrix Element
SVD	Singular Value Decomposition
TBME	Two-Body Matrix Elements
VLC	Varied Linear Combinations

CHAPTER 1

FOUNDATIONAL INTRODUCTION

This chapter is meant to briefly introduce the context of this work, both historically and contemporaneously. Depending on the reader's familiarity with each section of this chapter, one may feel free to move on to the next sections as the context narrows. The first section describes the largest scope of known nuclei and gives a very brief history of the conception of the nucleus and its components. The second section gives examples of early models used to describe and predict various observables relevant to nuclear physics, and describes how these models systematically break down in a way that motivates a need for a new model. The third section narrows this discussion to the formalism of the nuclear shell model, its beginnings, its development as a model, and its domain of validity as an effective theory. This section explains how, within this shell model formalism, we describe the interactions and their configurations, and that realistic wavefunctions from these interactions are constructed to predict observable quantities, such as energy spectra and electromagnetic structure.

1.1 The Nuclear Landscape

The origins of nuclear physics are set in the last four years of the 19th to the early 20th century. Henri Becquerel discovered radioactivity while investigating phosphorescence in uranium salts in 1896. With the efforts of physicists such as Marie and Pierre Curie, Ernest Rutherford, and J. J. Thompson, it was soon discovered that there were three types of radioactivity, called α-, β-, and γ-radiation. In 1911 Ernest Rutherford carried out the famous gold foil experiment, in which he discovered that the center of each atom is a dense collection of charges responsible for the deflection of α-particles. He carried out a similar experiment in 1917, only this time he bombarded ^{14}N gas with α-particles and observed that hydrogen nuclei were emitted. He concluded that the emitted Hydrogen nucleus was from the nitrogen and that this Hydrogen nucleus was a part of every atom, marking the discovery of the (later named) proton as a building block of the nucleus. Following inconsistencies with the hypothesis that the nucleus consists of only protons and nuclear electrons, James Chadwick carried out a series of experiments in 1932 wherein he discovered that a new type of uncharged particle with a mass similar to that of a proton was also contained in nuclei - a particle

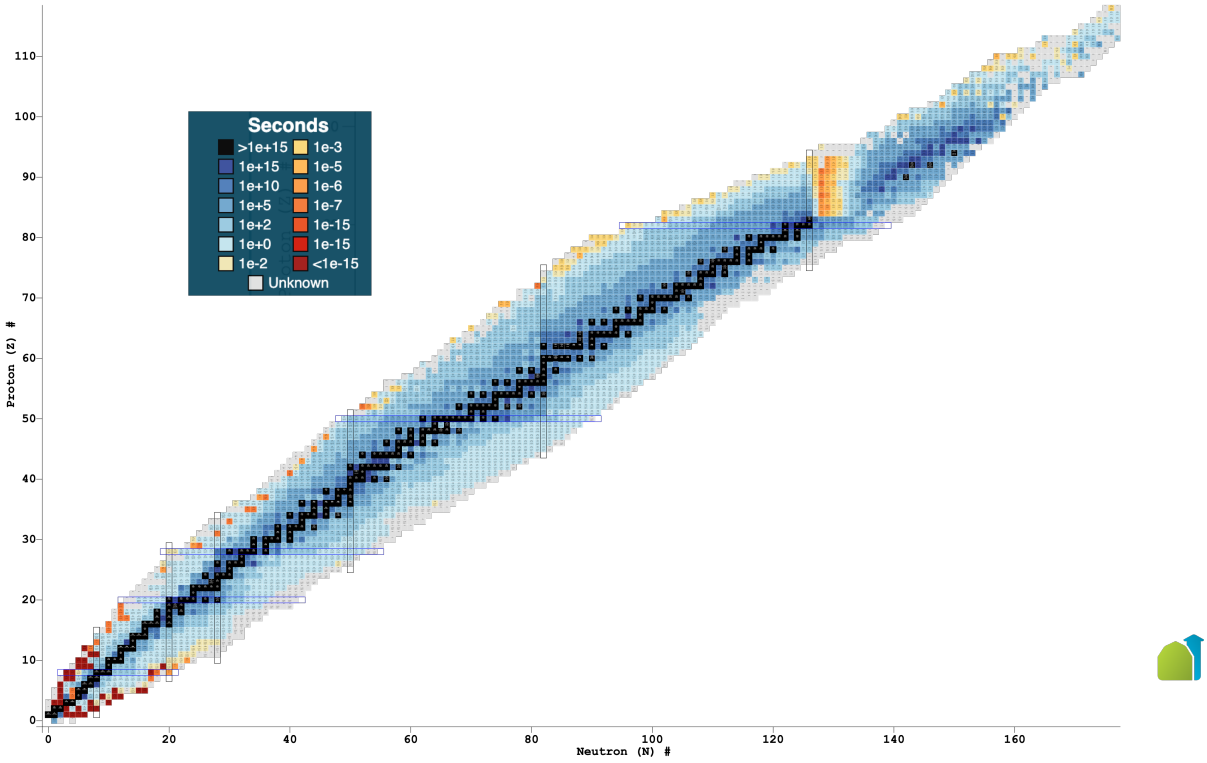

Figure 1.1 Half-Lives of all observed nuclei as a function of proton and neutron number, with a scale given in seconds. [2]

that would be named the neutron for its lack of charge.

Within months of the discovery of the neutron, physicists Werner Heisenberg and Dmitri Ivanenko proposed proton–neutron models for the nucleus, replacing the proton-electron model. With the proton-neutron model in hand, physicists have been able to explain many of the structural properties and reactions between the nuclei in our universe. Shown in Figure 1.1 is the nuclide diagram, given by the NNDC [2]. This chart shows all of the discovered nuclei as a function of proton and neutron number; in particular, it shows the half-lives of the known nuclei, which is related to the stability of each nucleus. The most stable nuclei are shown in black, lying in what is referred to as the "valley of stability", and it is clear from the bend in the landscape that Nature grants stability to nuclei that are rich in neutrons as opposed to protons.

1.2 An Early Empirical Model

One of the earlier models of a nucleus is the Liquid Drop Model (LDM) proposed by George Gamow in 1930 [3]. The LDM is motivated by several general observations about nuclear physics:

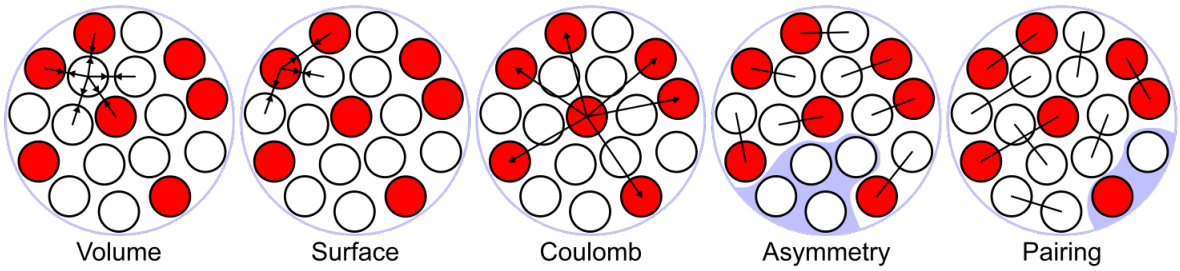

Figure 1.2 The various components of the binding energy in the liquid drop model. [4]

the strong interaction is incredibly short-ranged - only really occurring over a span of femtometers, and primarily between neighboring nucleons (or those with a large degree of spatial overlap in their wavefunctions) - and the density of nucleons in a nucleus saturates to a nearly constant value of $\rho_0 = 0.16$ nucleons/fm^3. In this way, a nucleus is similar to a liquid drop composed of droplets ordinarily held together by electrostatic forces. In this model, the binding energy of a nucleus is described by contributions from several sources:

For a nucleus with N neutrons, and Z protons, and a total nucleon number $A = N + Z$, the binding energy is described by the semi-empirical mass formula (SEMF):

$$BE(N,Z) = a_V A - a_S A^{2/3} - a_C Z(Z-1)A^{-1/3} - a_A (N-Z)^2 A^{-1} + a_P \delta(N,Z) A^{-3/4} \qquad (1.1)$$

where each of the terms in the equation is related in order to the series of figures in Figure 1.2, and the coefficients a_i are obtained from fits of the experimental data.

For some of the most stable nuclei, this model is fairly successful in reproducing the binding energies per nucleon, as shown in Figure 1.3. A broader inspection of the nuclear landscape reveals systematic discrepancies between the SEMF predictions and the experimental results, as can be seen in Figure 1.4. This discrepancy is a strong motivation towards a model that can reproduce the binding energy enhancements of nuclei with a particular combination of (N, Z), toward the nuclear shell model.

1.3 The Nuclear Shell Model

The previous discussion focused on discrepancies between the experimental binding energies and those predicted by the empirical LDM encapsulated by the SEMF. These discrepancies highlight

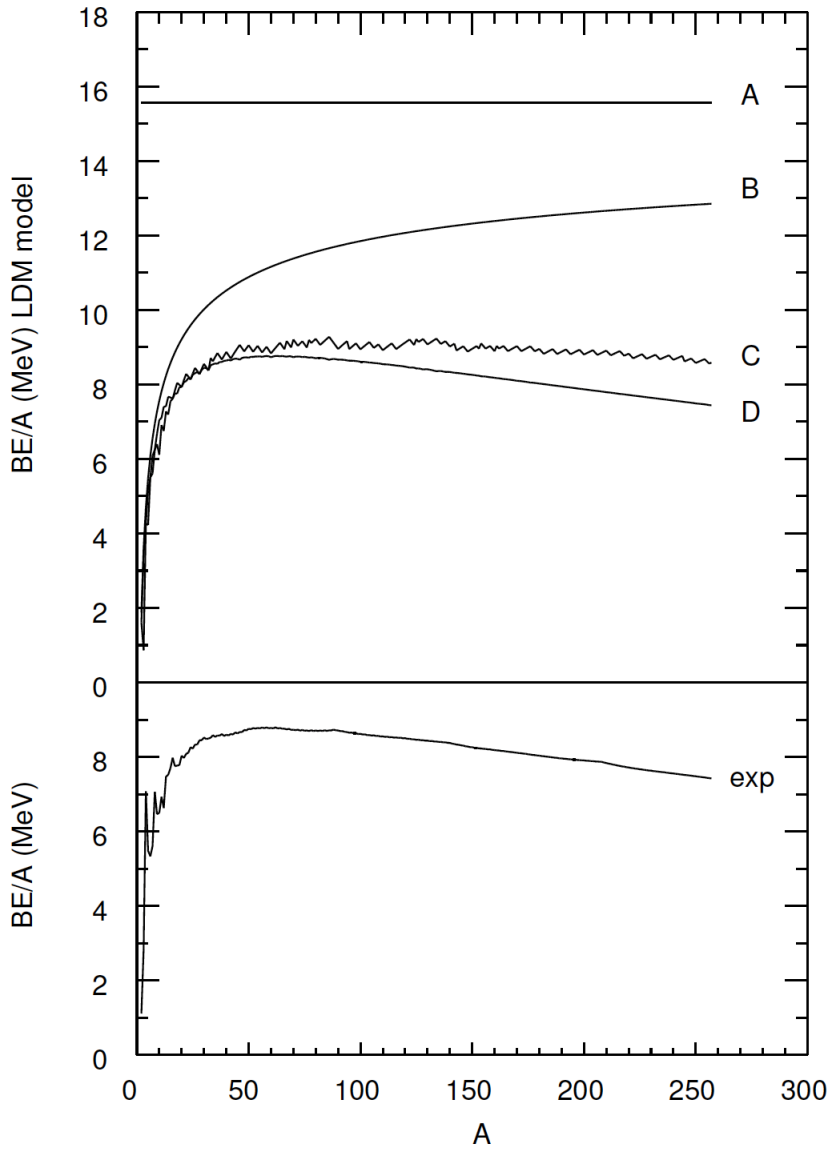

Figure 1.3 The binding energy per nucleon for the most stable nuclei in both the LDM and experiment. The top panel shows the contribution of the volume term (A), plus the surface term (B), plus the Coulumb term (C), all summed to the full LDM (D). [5]

the need for a new model, and one class of experimental observables that motivate what that model should entail are the nucleon separation energies. Figure 1.5 shows the single nucleon separation energies $S_{n,p}$ for a selection of nuclei compared to the calculation using a Hartree-Fock-Bogoliubov (HFB) model. The one-neutron separation energy S_n and one-proton separation energy S_p are defined as the difference between binding energy between a given nucleus and the binding energy

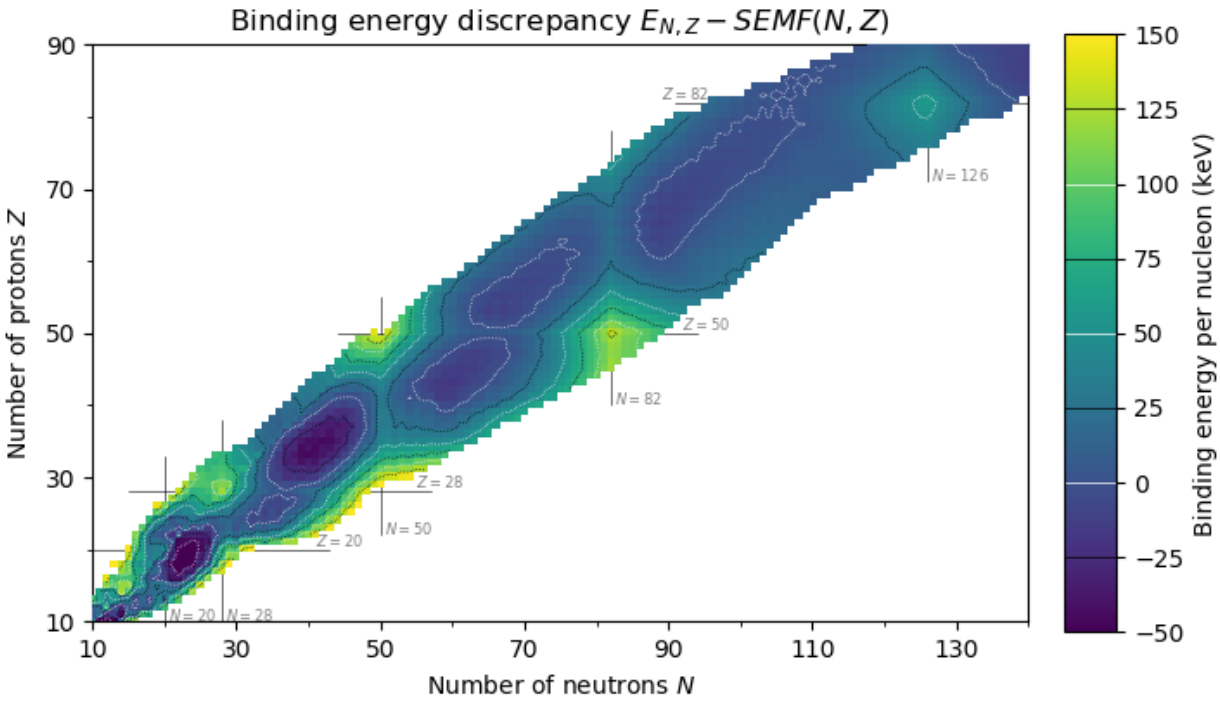

Figure 1.4 The difference in binding energy per nucleon across the nuclear landscape between the LDM and experiment. There is a systematic deviation between the SEMF and experiment toward the magic numbers. Figure sourced in [6].

of a nucleus with one less corresponding nucleon:

$$S_n = BE(N,Z) - BE(N-1,Z)$$
$$S_p = BE(N,Z) - BE(N,Z-1) \tag{1.2}$$

One can see that for a given nucleon number N or Z, the corresponding $S_{n,p}$ oscillates as the independent nucleon variable increases, which is a consequence of the pairing component of the strong interaction. Additionally, one can see that there is a precipitous drop in the separation energy as the independent nucleon variable moves past certain values; these values correspond to the previously mentioned magic numbers, which were the source of the largest deviation between the experiment and the LDM.

As one can see in Figure 1.6, the change in binding energy at the magic numbers can be highlighted by taking the second derivative of the binding energy with respect to nucleon number

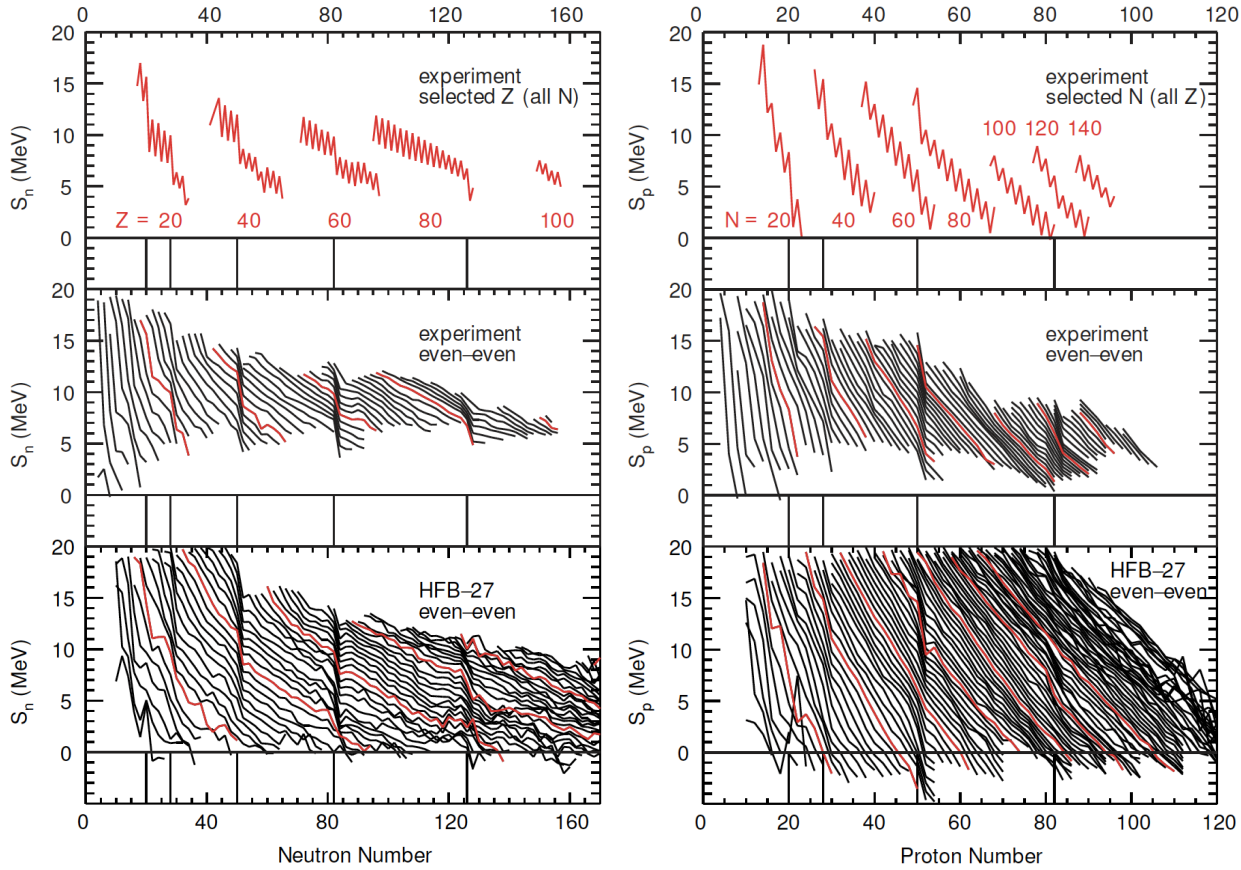

Figure 1.5 Single nucleon separation energy $S_{n,p}$ as a function of Nucleon number (N, Z). The left figure considers 1-neutron separation energies, while the right figure considers 1-proton separation energies. The top panel shows the $S_{n,p}$ values for a a set of isotopes (isotones) of a given proton (neutron) number. The middle panel gives $S_{n,p}$ values for the isotopes (isotones) of several even-even nuclei, and shows the corresponding curves from the top panel in red. The bottom panel gives predictions from a given Hartree-Fock-Bogoliubov (HFB) model for many of the same even-even nuclei. [5]

for both protons and neutrons:

$$D_n = 2BE(N,Z) - BE(N-1,Z) - BE(N+1,Z)$$
$$D_p = 2BE(N,Z) - BE(N,Z-1) - BE(N,Z+1) \tag{1.3}$$

The existence of nuclei with particular nucleon numbers that are exceptionally bound relative to nearby nuclei hearkens back to the observation that some atoms have electrons with exceptionally high ionization energies. These atoms are noble gasses and their large ionization energies are explained in the atomic shell model by filling electron orbital shells separated by large energy gaps. Maria Göppert Mayer developed the nuclear shell model in 1949 and published the work in 1950

[7], and in this formalism the magic numbers of nuclei correspond to the filling of proton and neutron orbits separated by large gaps in energy.

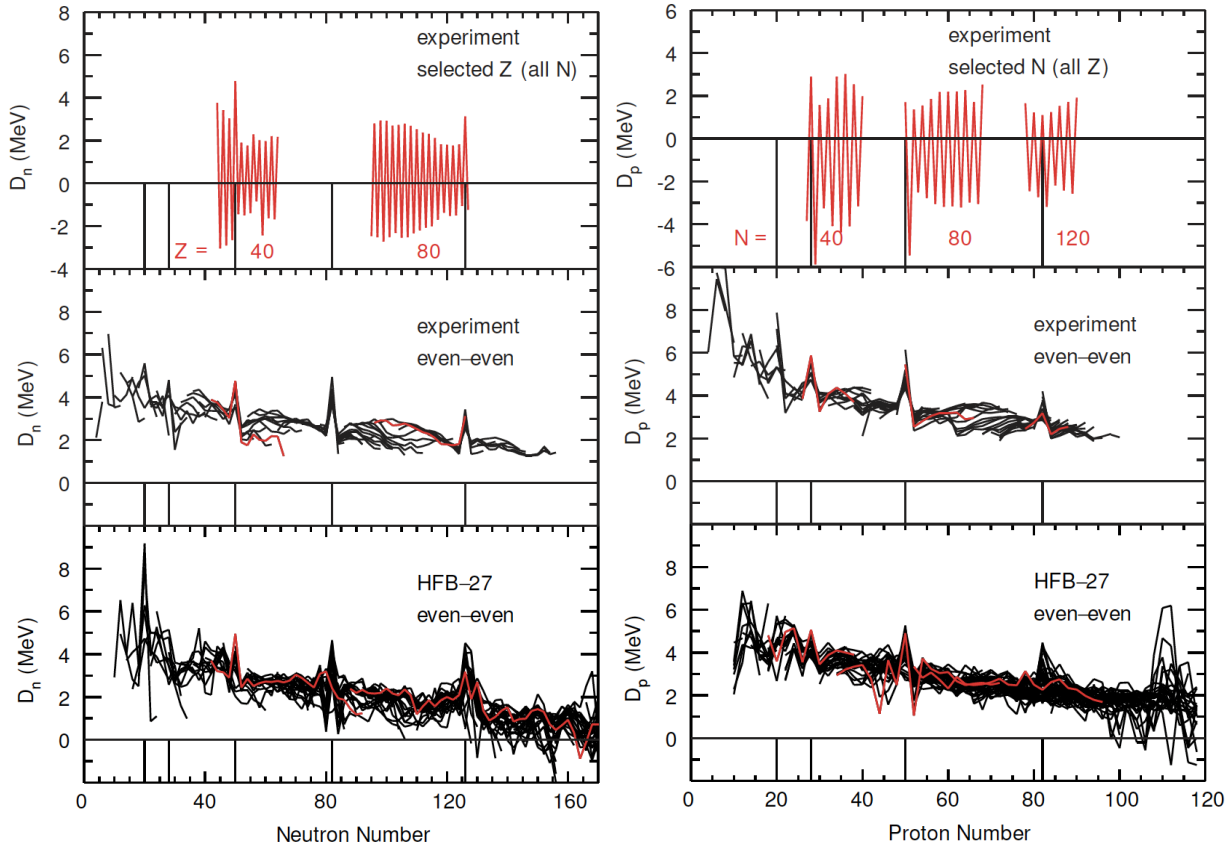

Figure 1.6 Second derivative of single nucleon separation energy $D_{n,p}$ as a function of Nucleon number (N, Z). The left and right figures are organized in a fashion analogous to Figure 1.5. [5]

Since its inception, the nuclear shell model has made steps toward increasing complexity and realism. One of the simplest versions of the shell model treats the strong interaction as a harmonic oscillator problem; the issue with this model is that it treats the shell gap spacings as equal when we can observe the magic numbers are not evenly spaced in energy. A more complex model is the Woods-Saxon potential, which does approach the spacing seen in the magic numbers. Adding in spin-orbit coupling provides level splitting for a given orbital angular momentum quantum number. An account of these potentials is shown in Figure 1.7. Modern day shell model interactions involve a basis of occupational configuration states in some truncated model space of orbits relevant to the nuclei under investigation, and an effective interaction is tuned specifically to each model space.

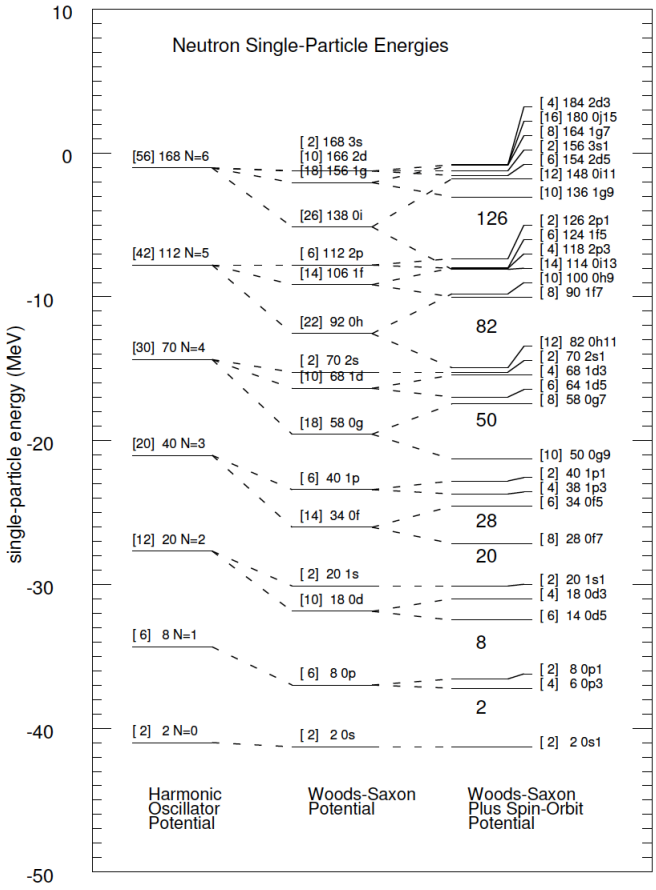

Figure 1.7 The single-particle energies of neutrons in three different potentials: the harmonic oscillator on the left, the Woods-Saxon in the middle, and a Woods-Saxon with spin-coupling added on the right. [5]

1.3.1 Model Spaces

A model space is a selected set of single-particle orbits for protons or neutrons inclusively, and by its nature excludes all orbits outside of the model space. This truncation is necessary to reduce the complexity of the calculations to a feasible computational time-frame; in principle, there are an infinite number of single-particle orbits that would need to be included in any calculation, and in practice no computer has infinite memory. An example of a model space relevant to this work is shown in Figure 1.8, where one can see the four orbits used in our model contained in a dashed black box. Given the truncated nature of these model spaces, one must take care when selecting data to incorporate into a fit of an interaction because some experimental data contain information from configurations involving orbits outside of the model space. We refer to such states as intruder

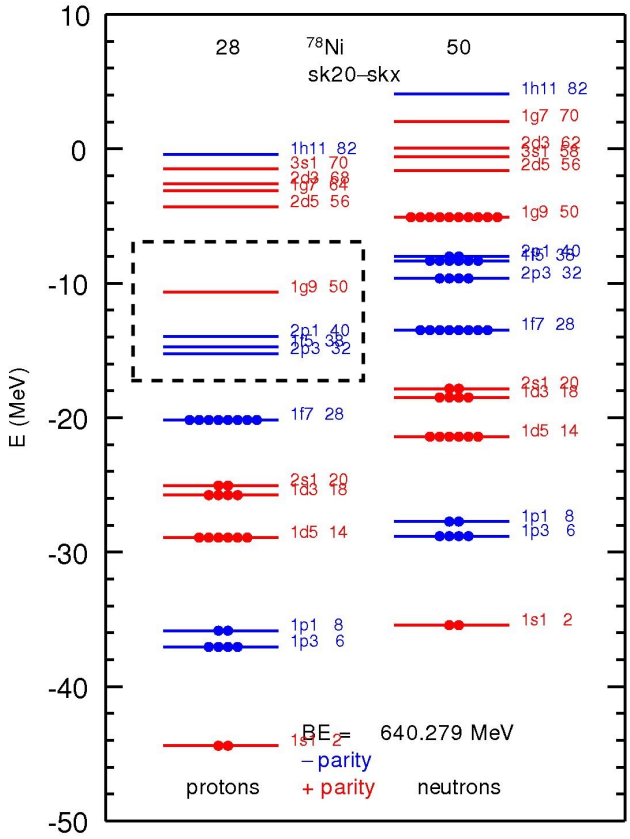

Figure 1.8 The single-particle orbits for the ground state of ^{78}Ni. The left and right columns correspond to proton and neutron single-particle orbits, respectively. The circles show the occupations of protons and neutrons in the ground state, and the orbits contained in the dashed box show the $\pi j4$ model space orbits. This calculation was performed with an SKX Skyrme interaction using the DENS program contained in NuShellX.

states and they will be the subject of discussion later on.

Model spaces tend to span the range of orbits contained within a major shell because these orbits tend to be clustered together in energy, and interactions between nucleons in their configurations influence a wide array of nuclear spectra, while the major shells themselves are separated by comparatively larger amounts of energy. Provided one is interested in low-lying spectra, this truncation tends to produce very accurate reproductions of known data and predictions for unobserved data.

Figure 1.9 shows the comparison in proton separation energy between experiment and theory for the nuclei considered in this thesis. From the top panel, we see that there is an abrupt drop

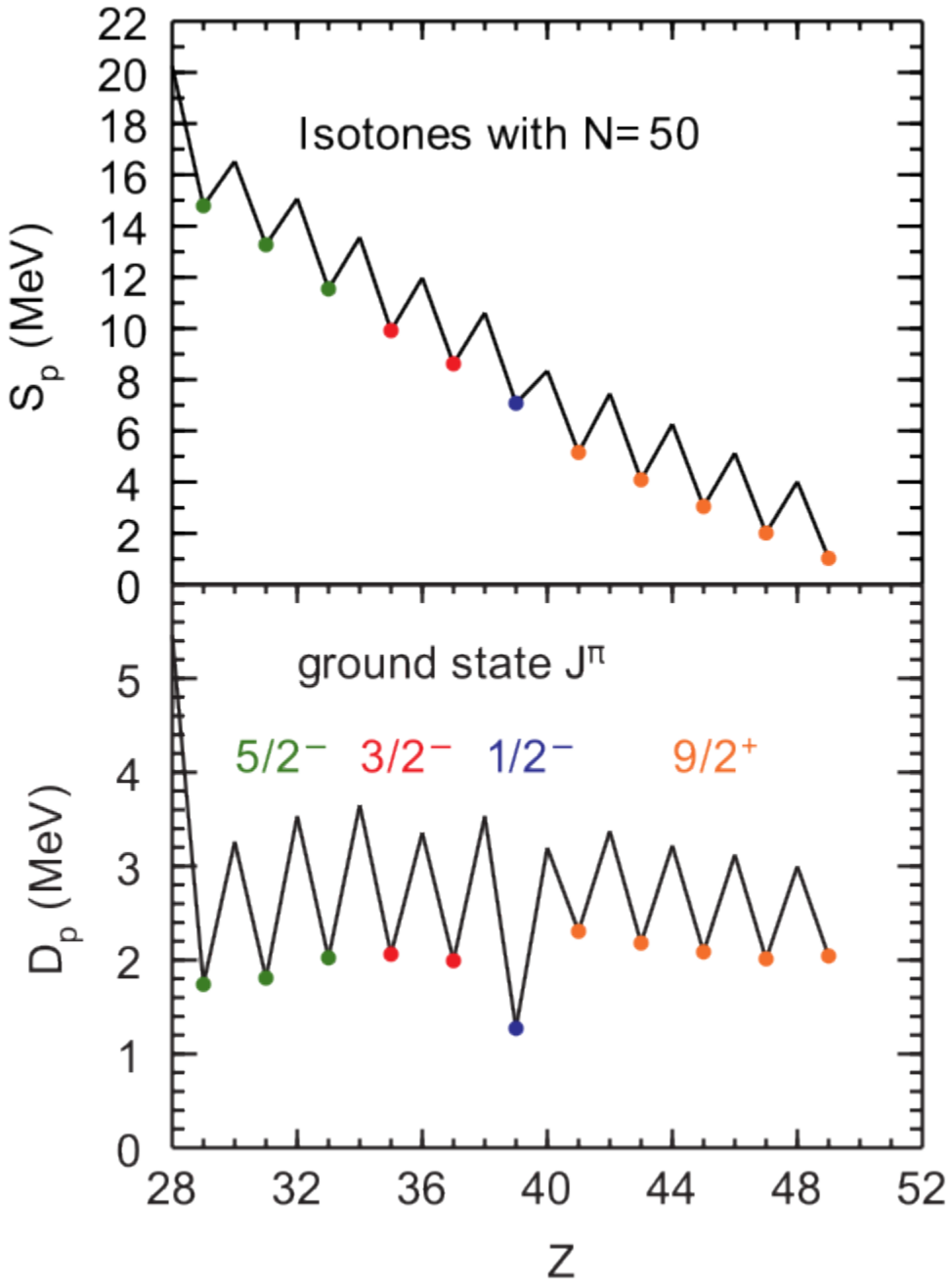

Figure 1.9 Top panel: Single-proton separation energy as a function of proton number (Z). Bottom Pane: Second derivative of top panel using equation 1.3. The oscillation is a hallmark of the pairing interaction, with the even-even nuclei having a larger single-proton separation energy than the odd-even nuclei. For the nuclei with odd Z, the ground-state spin from the unpaired proton is color-coded.

in binding separation energy going from ^{78}Ni to ^{79}Cu, and we observe the odd-even oscillations that are hallmark of the pairing interaction that enhances the binding energy of even-even nuclei. The bottom panel illustrates the second derivative of the proton separation energy with respect to the proton number, as described by Equation 1.3, and serves to illustrate shell gaps within the $\pi j4$ model space. Focusing only on the odd-even nuclei in the figure (colored points), one can see three distinct regions of the D_p values: the ^{89}Y nucleus with $Z = 39$, and the collections of nuclei with $Z < 39$ and $Z > 39$. As discussed in [8], the relatively low value of D_p centered on ^{89}Y is a consequence of the fully occupied valence orbit $1p_{1/2}$ in the ground state that has a sizable shell gap between the $\{0f_{5/2}, 1p_{3/2}\}$ orbits below and the $0g_{9/2}$ orbit above. The relatively constant value of D_p for nuclei with $Z < 39$ indicates a relatively small shell gap between the orbits $0f_{5/2}$ and $1p_{3/2}$.

1.3.2 Effective Interactions

In the context of the nuclear shell model, effective interactions are interactions that are effective in a given model space. Modern effective interactions are expressed in the second quantization formalism, and in a simplified form can be expressed as the sum:

$$H = H_0 + H_1 + H_2 \tag{1.4}$$

where H_0 is the binding energy of the closed shell of occupied orbits outside the model space - the ground state configuration of ^{78}Ni in this thesis - H_1 are the single-particle energies of the orbits defining the model space, and H_2 are two-body matrix elements describing the interaction between the orbital configuration states in each nucleus. A more in-depth description of the formalism of these effective interactions will be given in the following chapters.

CHAPTER 2

FORMALISM

2.1 Many-body Wavefunctions

The nucleus is a system of many interacting particles, therefore investigations in nuclear physics are inherently many-body problems in nature. To this end, we employ many-body wavefunctions to represent the nuclear system, and our operators are many-body expansions at the zero-body, one-body, and two-body levels. The wavefunctions and operators are constructed in second-quantization in terms of creation and annihilation operators. In this thesis, we are concerned with the following quantum numbers: the principal quantum number n, the orbital angular momentum ℓ, the coupled angular momentum $j = \ell + s$, the projections of the coupled angular momentum m, and the projection of the isospin quantum number t_z. Since we are dealing with only proton wavefunctions, we know that $t_z = -1/2$, and because protons are fermions, we also know that the spin quantum number is $s = 1/2$. The many-body wavefunctions are constructed as product states, for example the n-body wavefunction where each particle has quantum numbers $a_i = (n, \ell, j, m, t_z)_i$ has the form:

$$|\Psi\rangle = |a_\alpha a_\beta \dots a_\omega\rangle = \prod_{i=\omega}^{\alpha} |a_i\rangle = \prod_{i=\omega}^{\alpha} a_i^\dagger |0\rangle \tag{2.1}$$

where $|0\rangle$ denotes the vacuum state with 0 particles. Similarly he complex conjugate states are:

$$\langle\Psi| = \langle a_\omega \dots a_\beta a_\alpha| = \prod_{i=\omega}^{\alpha} \langle a_i| = \langle 0| \prod_{i=\omega}^{\alpha} a_i \tag{2.2}$$

Because the particles involved in our system are fermions, the usual anti-commutation relations are applied to the creation and annihilation operators to establish anti-symmetry in the wavefunctions describing the system:

$$\begin{aligned} \{a_\alpha^\dagger, a_\beta^\dagger\} &= a_\alpha^\dagger a_\beta^\dagger + a_\beta^\dagger a_\alpha^\dagger = 0 \\ \{a_\alpha, a_\beta\} &= a_\alpha a_\beta + a_\beta a_\alpha = 0 \\ \{a_\alpha^\dagger, a_\beta\} &= a_\alpha^\dagger a_\beta + a_\beta a_\alpha^\dagger = \delta_{\alpha\beta} \end{aligned} \tag{2.3}$$

We will see in the following section that expressing an operator in second-quantization requires the specification of some single-particle basis, as the creation and annihilation operators contained

within the expression are scaled by a matrix element of the given operator.

2.2 Symmetries and Choosing a Basis

As with any quantum mechanical system, one desires a basis that will respect symmetries of the Hamiltonian and naturally give rise to eigenstates and eigenvalues corresponding to quantities conserved in the interaction. Decades of observation of the nuclear reactions and decays reveal that some quantities such as total angular momentum and parity are conserved, while other quantities such as isospin are partially conserved under the strong interaction. The following sections discuss the conserved quantities that are used to build a natural basis for representing the nuclear system.

2.2.1 Rotational Symmetry and Angular Momentum

The Hamiltonian used to describe the nuclear system is scalar in spatial coordinates and is invariant under changes in the orientation of the nuclear system. The consequence of this rotational symmetry is that the total coupled orbital and spin angular momentum of the system $\hat{J} = \hat{L} + \hat{S}$ is a conserved quantity, and therefore the Hamiltonian commutes with the total angular momentum operators:

$$\left[H, \hat{J}^2\right] = \left[H, \hat{J}_z\right] = 0 \tag{2.4}$$

This means that the many-body energy eigenstates of the Hamiltonian are also eigenstates of the total angular momentum J, and have conserved quantum numbers:

$$\begin{aligned} \hat{J}^2|\Psi\rangle &= J(J+1)|\Psi\rangle \\ \hat{J}_z|\Psi\rangle &= M|\Psi\rangle \end{aligned} \tag{2.5}$$

where for a given total J there are $(2J+1)$ values of the projection M ranging from $M = \{-J, -J+1, \cdots, J-1, J\}$ in integer steps. A basis construction which has good J and J_z is called the J-scheme; a basis which has good J_z but not good J is called the M-scheme. Our goal is to construct a basis that has good J and J_z, therefore, when possible, the J-scheme should be utilized to represent the nuclear system; If the M-scheme basis is complete with respect to rotations in the J-space, then the M-scheme basis will also have good J in addition to J_z.

2.2.2 Mirror Symmetry and Parity

The strong and electromagnetic interactions are invariant under reflection, and because they obey this mirror symmetry the parity π of the system is a conserved quantity. The eigenstates of the Hamiltonian can have even parity $\pi = +1$ or odd parity $\pi = -1$, and the Hamiltonian does not mix the parity of a state with known initial parity. The total parity of a nucleus is obtained from the intrinsic parity of each nucleon $\pi_{int} = +1$ and the parities arising from the orbital angular momenta ℓ of each nucleon in the nucleus $\pi_\ell = (-1)^\ell$. The total parity of a physical system is the product over all sources of parity in the physical system, and because all nucleons possess even parity, the total parity is due to the product of all parities due to orbital angular momentum from each nucleon. This means that the parity of a nucleus with N nucleons represented in the many-body wavefunction is given by:

$$\pi = \prod_{i=1}^{N} \pi_{int}(i)\pi_\ell(i) = \prod_{i=1}^{N} (-1)^{\ell_i} \tag{2.6}$$

The conservation of parity under the strong and electromagnetic interactions puts restrictions on the types of electromagnetic transitions that can occur when a nucleus decays from one state to another.

2.3 Isospin

The proton mass is 938.27 Mev/c^2, the neutron mass is 939.57 MeV/c^2, and both particles are spin $s = 1/2$. Because their masses are within 0.1% and share the same spin, protons and neutrons can be thought of as doublets of the same generalized nucleon particle with a quantum number $t = 1/2$ called isospin, where the proton and neutron are described as isospin projections of $t_z = -1/2$ and $t_z = +1/2$, respectively. Though isospin is described by an algebraic structure similar to angular momentum, it is a dimensionless quantity and does not describe physical rotations. For a nucleus composed of n nucleons, the total isospin (T) and it's projection (T_z) of the nucleus are simply the sum of the individual respective isospins and projections of the n nucleons:

$$T = \sum_{i=1}^{n} t(i) \qquad \text{and} \qquad T_z = \sum_{i=1}^{n} t_z(i) \tag{2.7}$$

Isospin is only an approximate symmetry of the strong interaction, an effect that can be seen by comparing the proton-proton, neutron-neutron, and proton-neutron binding energies, each of which are progressively more bound in the order listed. One source of isospin symmetry breaking is the obvious difference in which the proton is charged and the neutron is neutral, manifesting in a break in symmetry through the Coulomb interaction. Even when the Coulomb effects are taken into account, isospin is not an exact symmetry of the strong interaction itself and can be encapsulated in addition of isotensor interactions to the Hamiltonian, as has been demonstrated in USD-type Hamiltonians [9]. This work is concerned with a model space and Hamiltonian that involve only interactions between configurations of protons. For our Hamiltonian, all particles under consideration have $t_z(i) = -1/2$, and so the TBME all involve isospins coupled to $T = 1$ with a projection $T_z = -1$.

2.4 Operators

A given operator can be expressed in second-quantization through pairs of creation and annihilation operators multiplied by a matrix element. For example, we can express an operator F in second-quantization as a one-body operator with:

$$\hat{F} = \sum_{\alpha\beta}^{n} \langle \alpha | F | \beta \rangle a_\alpha^\dagger a_\beta \tag{2.8}$$

The tensor-coupled form of the one-body transition operator of tensor rank λ is given by:

$$\begin{aligned} \hat{O}_\mu^\lambda &= \sum_{k_\alpha k_\beta} \sum_{m_\alpha m_\beta} \left\langle k_\alpha \left\| O^\lambda \right\| k_\beta \right\rangle (-1)^{j_\alpha - m_\alpha} \begin{pmatrix} j_\alpha & \lambda & j_\beta \\ -m_\alpha & \mu & m_\beta \end{pmatrix} a_\alpha^\dagger a_\beta \\ &= \sum_{k_\alpha k_\beta} \left\langle k_\alpha \left\| O^\lambda \right\| k_\beta \right\rangle \frac{\left[a_{k_\alpha}^\dagger \otimes \tilde{a}_{k_\beta} \right]_\mu^\lambda}{\sqrt{2\lambda + 1}} \end{aligned} \tag{2.9}$$

where k_α stands for the single-particle quantum numbers $(n_\alpha, l_\alpha, j_\alpha)$. In practice, one is interested in calculating an observable property represented by an operator $\hat{O}$ given some realistic wavefunction that represents the nuclear system in some initial state $|\Psi_i\rangle$ and some final state $|\Psi_f\rangle$. This is accomplished by taking the overlap $\langle \Psi_f | \hat{O} | \Psi_i \rangle$. With this goal in mind, one can calculate the reduced matrix element for the n-particle wavefunction as the sum over the product of one-body

transition densities (OBTD) with their corresponding single-particle reduced matrix elements:

$$\left\langle \Psi_f \left\| \hat{O}^\lambda \right\| \Psi_i \right\rangle = \sum_{k_\alpha k_\beta} \mathrm{OBTD}\left(f, i, k_\alpha, k_\beta, \lambda\right) \left\langle k_\alpha \left\| O^\lambda \right\| k_\beta \right\rangle \tag{2.10}$$

where the OBTD is given by:

$$\mathrm{OBTD}\left(f, i, k_\alpha, k_\beta, \lambda\right) = \frac{\left\langle \Psi_f \left\| \left[a^\dagger_{k_\alpha} \otimes \tilde{a}_{k_\beta} \right]^\lambda_\mu \right\| \Psi_i \right\rangle}{\sqrt{2\lambda + 1}} \tag{2.11}$$

Similarly, we can express a tensor operator T^λ_μ of rank λ in second-quantization as a two-body operator with:

$$\hat{T}^\lambda_\mu = \frac{1}{4} \sum_{\alpha\beta\gamma\delta} \left\langle \alpha\beta \left| T^\lambda_\mu \right| \gamma\delta \right\rangle a^\dagger_\alpha a^\dagger_\beta a_\delta a_\gamma \tag{2.12}$$

In the above equations, the indices in the sums represent sets of quantum numbers, for example $\alpha = (n_\alpha, l_\alpha, j_\alpha, \dots)$, and in principle there are an infinite number of terms in the sum. In practical applications, finite memory in computers restricts us to use some truncated amount of levels. The amount of levels required is usually motivated by the nuclei under investigation - for example, one might truncate to the orbitals within some major shell.

2.5 Configuration Interactions

2.5.1 Formulation of the Hamiltonian

The Hamiltonian for CI can be expressed as the sum of zero-body, one-body, and two-body operators:

$$H = E_0 + \sum_\alpha \epsilon_\alpha \hat{n}_\alpha + \sum_{\alpha \le \beta, \gamma \le \delta} \sum_{JM} V_J(\alpha\beta; \gamma\delta) \hat{T}_J(\alpha\beta; \gamma\delta) \tag{2.13}$$

where E_0 is the binding energy of the closed shell with 0 valence nucleons, and ϵ_α are single-particle energies corresponding to a particle in orbital α and $\hat{n}_\alpha$ are the number operators for particles in these orbitals (given by quantum numbers $n_\alpha, l_\alpha, j_\alpha$). $V_J(\alpha\beta; \gamma\delta)$ are the two-body scalar matrix elements for nucleon pairs in orbital states α, β, γ, and δ coupled to total angular momentum quantum number J.

$$\hat{T}_J(\alpha\beta; \gamma\delta) = A^\dagger_{JM}(\alpha\beta) A_{JM}(\gamma\delta) \tag{2.14}$$

is the two-body scalar density operator for nucleon pairs in orbits α, β, γ, and δ coupled to spin quantum numbers J and M, where $A^{\dagger}_{JM}(\alpha\beta)$ creates an antisymmetric state of two particles in orbital states α and β coupled to the quantum numbers in the subscript. The single particle energies and two-body matrix elements are the parameters of our effective interaction; if we choose to keep some of these parameters fixed, we can break the Hamiltonian into a fixed part H^0 and a term H^1 that depends on the variable parameters p_i:

$$H = H^0 + H^1(\vec{p}) = H^0 + \sum_{i=1}^{N_p} p_i \hat{O}_i \tag{2.15}$$

where p_i represents either the single-particle energies ϵ_α or the two-body matrix elements $V_J(\alpha\beta;\gamma\delta)$, N_p represents the number of parameters we allow to vary in our fit, and $\hat{O}_i$ represents the associated number operator or the scalar two-body density operator. If the k'th energy eigenvector of the Hamiltonian is given by $|\phi_k\rangle$ then the corresponding energy eigenvalue is:

$$\lambda_k = \langle\phi_k|H|\phi_k\rangle = \langle\phi_k|H^0|\phi_k\rangle + \sum_{i=1}^{N_p} p_i \beta_i^k = E_k^0 + \epsilon_k(\vec{p}) \tag{2.16}$$

where $\beta_i^k = \langle\phi_k|\hat{O}_i|\phi_k\rangle$ and $\vec{p} = (p_1, \cdots, p_{N_p})$ is the vector of Hamiltonian parameters defining the Hamiltonian, E_k^0 is the contribution to the calculated energy of eigenstate $|\phi_k\rangle$ due to the fixed portion of the interaction H^0, and $\epsilon_k(\vec{p})$ is the contribution from the fitted portion of the interaction $H^1(\vec{p})$.

2.6 Electromagnetic Operators

Following the conventional definitions and assumptions for electromagnetic operators laid out in [10], the electric multipole operator $O(E, \lambda M)$ is given by:

$$O(E, \lambda M) = \int \rho(\mathbf{r}) \mathbf{r}^L Y_M^L(\theta, \phi) d\mathbf{r} = \sum_k e(k) r_k^L Y_M^L(\theta, \phi) \tag{2.17}$$

where $\rho(\mathbf{r})$ is the charge-density operator and $e(k)$ is the charge of the k'th nucleon. Analogous to the electric multipole operator, the magnetic multipole operator $O(M, \lambda M)$ is given by:

$$\begin{aligned} O(M, \lambda M) &= \int \rho_m(\mathbf{r}) \mathbf{r}^\lambda Y_M^\lambda(\theta, \phi) d\mathbf{r} \\ &= \sum_k \mu_N \left[\nabla_k \mathbf{r}_k^\lambda Y_M^\lambda(\theta, \phi)\right] \left[\frac{2g_\ell(k)}{\lambda+1}\mathbf{L}_k + g_s(k)\mathbf{S}_k\right] \end{aligned} \tag{2.18}$$

where μ_N is the nuclear magneton and the sum over k includes all particles in the nucleus. The reduced transition rate $B(\pi\lambda)$ for an electromagnetic λ'th pole transition from an initial state $|J_i M_i\rangle$ to a final state $|J_f M_f\rangle$ is defined by:

$$B(\pi\lambda) = \frac{|\langle J_f||O(\pi\lambda)||J_i\rangle|^2}{(2J_i+1)} \tag{2.19}$$

where π is either E for electric transitions or M for magnetic transitions, and λ gives the multipolarity of the transition: $\lambda = 1$ for dipole transitions, $\lambda = 2$ for quadrupole, and so on. The double vertibar indicates that the transition is reduced with respect to angular momentum. The predictions of the Shell model for electromagnetic transition rates and multipole moments of a nuclear system require calculations of the reduced matrix elements of the $O(\pi\lambda)$ operators between the many-body shell model wave functions. These matrix elements are obtained by expanding the $O(\pi\lambda)$ operators in the second-quantized form, using single-particle basis states $|k\rangle = a_k^\dagger|0\rangle$ with $k = (n, \ell, j)$ which define the shell-model basis. With this expansion, the matrix elements are obtained using Equations 2.10 and 2.11. The single-particle matrix elements (SPME) of the electric transition operator $O(E, \lambda M)$ can be factorized into a radial and an angular part:

$$\left\langle nlj \left\| \mathbf{r}^L Y_M^L(\theta,\phi) \right\| n'l'j' \right\rangle = \left\langle nl \left| \mathbf{r}^L \right| n'l' \right\rangle f_L(j,j') \tag{2.20}$$

The radial integrals used in the present work are calculated with skyrme wavefunctions [11]. From Equation 2.10 we see that the matrix elements of the $(a_j^\dagger a_{j'})^{\lambda M}$ operators between initial/final shell-model wavefunctions contain the many-body results, independent of the detailed form of the shell-model wavefunctions $|k\rangle$. These matrix elements are the one-body transition densities given by equation 2.11, while the remaining factor in equation 2.10 is called the single-particle matrix element $S_{jj'}$:

$$S_{kk'} = \langle k\|O(\pi\lambda)\|k'\rangle \tag{2.21}$$

Combining the OBTD with the single-particle matrix elements, we arrive at the shell-model expression for the reduced transition strength:

$$B(\pi\lambda) = \frac{\left|\sum_{k_\alpha,k_\beta} \mathrm{OBTD}(f,i,k_\alpha,k_\beta,\lambda) S_{k_\alpha k_\beta}\right|^2}{2J_i+1} \tag{2.22}$$

Electromagnetic moments $\mathcal{M}(\pi\lambda)$ are defined by the diagonal matrix element of the one-body electromagnetic operator in a state with $M = J$:

$$\begin{aligned}\mathcal{M}(\pi\lambda) &\equiv \sqrt{\frac{4\pi}{2\lambda+1}}\langle\Psi, J, M = J|\mathcal{O}(\pi\lambda)|\Psi, J, M = J\rangle \\ &= \sqrt{\frac{4\pi}{2\lambda+1}}\begin{pmatrix} J & \lambda & J \\ -J & 0 & J \end{pmatrix}\langle\Psi, J\|\mathcal{O}(\pi\lambda)\|\Psi, J\rangle\end{aligned} \tag{2.23}$$

where the term in parentheses is the $3-j$ symbol, and $\langle\Psi, J||\mathcal{O}(\pi\lambda)||\Psi, J\rangle$ is the reduced matrix element for this moment.

2.6.1 Magnetic Dipole Moments and $M1$ Transitions

One of our aims is to investigate the properties of the magnetic dipole moments ($\lambda = 1$) and the $M1$ transitions in nuclei with 50 neutrons in the $\pi j4$ model space. Both of these observables depend on the matrix elements of the $\mathcal{O}(M1)$ operator. The magnetic charge density of the nucleus arises from both the orbital motion of the nucleons in the nucleus and their individual spin magnetic moments. The magnetic dipole moment is given by the diagonal matrix element of the $\mathcal{O}(M1)$ operator, this operator is written as:

$$\mathcal{O}(M1) = \sum_k [g_l(k)\mathbf{L}_k + g_s(k)\mathbf{S}_k] \tag{2.24}$$

where g_l and g_s are the orbital and spin g-factors, respectively, of the k'th nucleon, and $\mathbf{L}$ and $\mathbf{S}$ are the orbital and spin operators, respectively. For a state with total angular momentum J and a maximum magnetic quantum number $M = J$, the magnetic dipole moment is:

$$\begin{aligned}\mu &= \langle J, M = J|\mathcal{O}(M1)|J, M = J\rangle \\ &= \sqrt{\frac{J}{(J+1)(2J+1)}}\langle J\|\mathcal{O}(M1)\|J\rangle\end{aligned} \tag{2.25}$$

Following the expansion of Eq. 2.10 the calculation of the matrix elements of the $\mathcal{O}(M1)$ operator amounts to calculating OBTD's and single-particle matrix elements. Comparisons between our predictions and the experimental values of several nuclei are shown and discussed in Chapter 5. For example, comparisons are shown in FIG. 5.6, and a detailed comparison of these results for several different interactions is shown in Tables 5.1 and 5.2.

The $B(M1)$ values are also calculated from the $O(M1)$ operator; unlike the magnetic dipole moment, these values correspond to off-diagonal matrix elements connecting different initial and final states. From Equations 2.21 and 2.22, we can express the reduced transition strength for $M1$ transitions from state $|J_i\rangle$ to state $|J_f\rangle$ as:

$$B(M1) = \frac{\left|\langle J_f \| O(M1) \| J_i \rangle\right|^2}{2J_i + 1} \tag{2.26}$$

The reduced single-particle matrix element of $O(M1)$ can be separated into orbital ($\hat{\ell}$) and spin ($\hat{s}$) components from Equation 2.24. For single-particle states with $k = [nlj]$, the orbital reduced matrix element is given by:

$$\begin{aligned}\left\langle k_\alpha \| O(M1,\ell) \| k_\beta \right\rangle &= \sqrt{\frac{3}{4\pi}} \left\langle j_\alpha \left\| \hat{\ell} \right\| j_\beta \right\rangle \delta_{n_\alpha, n_\beta} g_\ell \mu_N \\ &= \sqrt{\frac{3}{4\pi}} (-1)^{\ell_\alpha + \ell_\beta + 3/2} \sqrt{\ell_\alpha(\ell_\alpha+1)(2\ell_\alpha+1)(2j_\alpha+1(2j_\beta+1)} \\ &\times \begin{Bmatrix} \ell_\alpha & \ell_\beta & 1 \\ j_\beta & j_\alpha & 1/2 \end{Bmatrix} \delta_{n_\alpha, n_\beta} \delta_{\ell_\alpha, \ell_\beta} g_\ell \mu_N\end{aligned} \tag{2.27}$$

Similarly, the spin reduced matrix element is given by:

$$\begin{aligned}\left\langle k_\alpha \| O(M1,s) \| k_\beta \right\rangle &= \sqrt{\frac{3}{4\pi}} \left\langle j_\alpha \left\| \hat{s} \right\| j_\beta \right\rangle \delta_{n_\alpha, n_\beta} g_s \mu_N \\ &= \sqrt{\frac{3}{4\pi}} (-1)^{\ell_\alpha + \ell_\beta + 3/2} \sqrt{\frac{3}{2}(2j_\alpha+1)(2j_\beta+1)} \\ &\times \begin{Bmatrix} 1/2 & 1/2 & 1 \\ j_\beta & j_\alpha & 1/2 \end{Bmatrix} \delta_{n_\alpha, n_\beta} \delta_{\ell_\alpha, \ell_\beta} g_\ell \mu_N\end{aligned} \tag{2.28}$$

where the term in curly braces is the Wigner $6-j$ symbol. These results can be added to give the full reduced single-particle matrix element of the $O(M1)$ operator and can also be used to evaluate the SPME for μ using $k_\alpha = k_\beta$. An immediate consequence of this is that $M1$ transitions can only connect single-particle states with the same principle (n) and orbital (l) quantum numbers.

2.6.2 Electric Quadrupole Moments and $E2$ Transitions

Another aim of this work was to investigate the properties of the electric quadrupole moment ($\lambda = 2$) and the $E2$ transitions in the $\pi j4$ model space. Both of these observables depend on the

matrix elements of the $O(E2)$ operator. The electric quadrupole moment is the diagonal matrix element of the $O(E2)$ operator for the state with $|J, M = J\rangle$, given by:

$$\begin{aligned} Q &= \sqrt{\frac{16\pi}{5}}\langle J, M = J|O(E2)|J, M = J\rangle \\ &= \sqrt{\frac{16\pi J(2J-1)}{5(2J+1)(J+1)(2J+3)}}\langle J||O(E2)||J\rangle \\ &= \sqrt{\frac{16\pi J(2J-1)}{5(2J+1)(J+1)(2J+3)}}\sum_k \mathrm{OBTD}(f, i, k, \lambda = 2)\langle k||O(E2)||k\rangle \end{aligned} \tag{2.29}$$

As in the case of magnetic dipole calculations, calculations of the $O(E2)$ matrix elements amount to calculating OBTD's and single-particle matrix elements.

The $B(E2)$ values are also calculated from the $O(E2)$ operator, and are the off-diagonal matrix elements connecting different initial and final states. The $B(E2)$ is calculated from Equation 2.22:

$$\begin{aligned} B(E2) &= \frac{\left|\langle J_f\|O(E2)\|J_i\rangle\right|^2}{2J_i+1} \\ &= \frac{1}{2J_i+1}\left|\sum_{k_\alpha,k_\beta}\mathrm{OBTD}(f, i, k_\alpha, k_\beta, \lambda = 2)\langle k_\alpha\|O(E2)\|k_\beta\rangle\right|^2 \end{aligned} \tag{2.30}$$

With single-particle orbitals $k = [nlj]$, the reduced single-particle matrix elements for the $O(E2)$ operator are given by:

$$\begin{aligned} \langle k_\alpha\|O(E2)\|k_\beta\rangle &= (-1)^{j_\alpha+1/2}\frac{\left[1+(-1)^{l_\alpha+l_\beta+2}\right]}{2} \\ &\times\sqrt{\frac{5(2j_\alpha+1)(2j_\beta+1)}{4\pi}}\begin{pmatrix} j_\alpha & \lambda = 2 & j_\beta \\ 1/2 & 0 & -1/2 \end{pmatrix}\left\langle k_\alpha\left|r^2\right|k_\beta\right\rangle e_q e \end{aligned} \tag{2.31}$$

The final step is to evaluate the overlap of r^2 between the initial and final single-particle states. This is accomplished by choosing a single-particle potential for expressing these states in position representation. This result can also be used to evaluate the SPME for Q using $k_\alpha = k_\beta$.

CHAPTER 3

HAMILTONIANS IN THE N=50 REGION

3.1 A Brief History of History of Hamiltonians for the $\pi j4$ Model Space

Configuration mixing effective interactions for isotones with 50 neutrons have a history dating back over 60 years; the first treatment of N=50 nuclei was given in 1960 by Talmi and Unna [12]. Effective interactions in this period used model spaces consisting only of the $1p_{1/2}$ and $0g_{9/2}$ proton orbits, requiring only 9 TBME to fit to experimental data, and so the nuclei that could be modeled were typically restricted to have masses at or above ^{88}Sr. Advances in computational capacity and many-body techniques allowed for the expansion of the model space to include more single-particle orbits in the calculations, and eventually the ability to construct a model space spanning the range of nuclei between the doubly magic ^{78}Ni and ^{100}Sn nuclei became possible, as was carried out by Ji and Wildenthal in 1988 [13], and later by Lisetskiy and collaborators in 2004 [14], the latter of which allowed for neutron orbits in addition to proton orbits.

In addition to restrictions imposed by computational capacity, these earlier types of effective interactions were limited by the availability of experimental data. The physical stability of the nuclei in the vicinity of ^{89}Y leads to ease of production and excellent characterization of the observable properties of these nuclei compared to regions away from stability; for example, all N=50 isotones between ^{86}Kr and ^{92}Mo were discovered between 1920 and 1930 (with the exception of ^{91}Nb which was discovered in 1951 [15]). Away from the valley of stability toward the doubly magic bookends of the model space, data have been historically sparse to non-existent; for example, ^{79}Cu was not formally discovered until 1991 [16], and ^{99}In (along with ^{100}Sn) was not discovered until 1994 [17]. The experimental energy spectra for these two nuclei are crucial for determining the 4 SPE parameters for the $\pi j4$ model space and how those parameters evolve across the model space.

Each iteration of these interactions has been the result of advances in computational capacity, improvements in fitting methods, and the growing body of experimental data to fit the model parameters to; the work outlined in this thesis is a natural continuation of this history.

3.2 Nuclear Data

For the experimental data used as input to our SVD fits, we chose nuclear spectra that have observed excitation energies with uncertainties generally at or below 2 keV and J^π values that are well determined by various types of experiments. Exceptions were made to the energy uncertainty criterion: for the binding energy of ^{79}Cu (100 keV uncertainty), the binding energy and the first excitation energy of ^{99}In (77 keV and 37 keV uncertainties, respectively), as well as the binding energy of ^{100}Sn (240 keV uncertainty). In addition, there are experimentally observed data that are not included in the SVD fits; those with large uncertainties on the energy or uncertain J^π values, and those that can be considered as intruder states in the $\pi j4$ model space; a discussion on intruder states and how they are determined is given in the following subsection. The experimental data used were obtained from the Evaluated Nuclear Structure Data Files (ENSDF) [18] motivated by a series of discussions with W. B. Walters of the University of Maryland.

3.2.1 Intruder States

When selecting the experimental data to be used in a fit, one has to consider the scope of the model space, as well as the configuration space content that may be contained in the experimental data. As mentioned, our model space consists only of 4 proton orbits on top of the closed ^{78}Ni core, and any ground state or excited state that we can predict can only be composed of configurations that lie within this model space. In a real nuclear ground state or excited state, the wavefunction will generally include contributions from single-particle configurations involving single-particle orbitals below our model space (particle-hole excitations of the ^{78}Ni core) or above it (particle-hole excitations above the $0g_{9/2}$ orbit). These particle-hole excitations can occur in experiments from both protons and neutrons and become an increasingly likely cause of concern as one approaches nuclear excitations comparable to the shell gap between the lower $0g_{9/2}$ orbit and the $0g_{7/2}$ orbit or the gap between the lower $0f_{7/2}$ orbit and the $0f_{5/2}$ orbit - both of these gaps are around 3 to 4 MeV. For this reason, the bulk of the experimental data used in our fits are ground states and low-lying excited states with an excitation energy below 3 MeV.

With these precautions being taken into account, it is important to know that the experimental

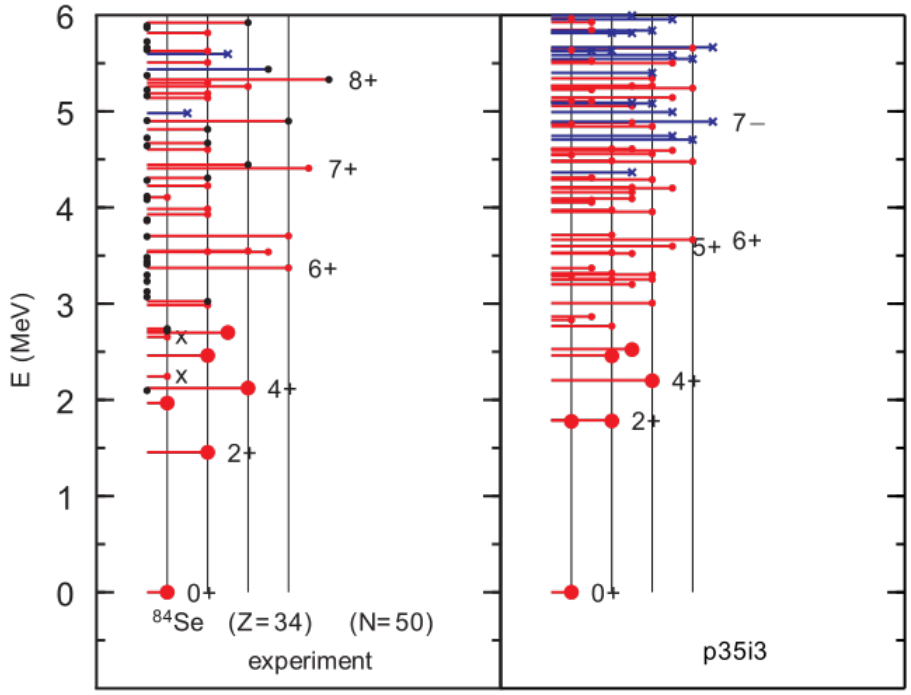

Figure 3.1 The energy spectrum of ^{84}Se. The left panel shows the experimental energies and spins, while the right panel shows the same content as predicted by our p35-i3 Hamiltonian. The spin of each state is given by the length of each line, and the parity is given by the color (red for even and blue for odd). The two states marked with an X are believed to be intruder states due to their enhanced cross-section in a (t, p) reaction [19]

states that we use in our fits are not devoid of influence beyond our model space by restricting to low-lying spectra. Consider Figure 3.1 as an example of how one must go beyond the restriction of low excitation and uncertainty as qualifications to select the appropriate fitting data. Some nuclear reactions provide excellent probes into the configuration content of a given experimental nuclear state. Mullins, Watson, and Fortune carried out an experiment in 1987 [19] involving the ^{82}Se$(t, p)^{84}$Se reaction as a means of investigating the structure of ^{84}Se. By analyzing the cross-section strengths into each excited state of ^{84}Se and comparing to predictions using a Distorted-Wave Born Approximation (DWBA), they found cross-sectional enhancements for the first two excited 0^+ states of the nucleus; those two states are shown in Figure 3.1 as the 0^+ states with black X's next to them in the left column (experiment). The low-lying spectrum for ^{84}Se is expected to be

dominated by proton particle-hole excitations; these cross-sectional enhancements are explained by contributions from 2-neutron excitations across the N=50 shell gap. Details of this comparison for the first two 0^+ states are given in Table I of [19]. With this discussion in mind, the existence of intruder states requires their careful consideration when selecting candidate data appropriate for a fit. Without such consideration, the fitting procedure would put inappropriate weights on the model parameters toward configurations beyond the scope of the model, resulting in a Hamiltonian that is less prescriptive and predictive.

3.3 Ab Initio Interactions

Ab initio is Latin for "from the beginning," and in this context it often means that the interactions are constructed from a microscopic (particle-based) interaction tuned to some experimental data, such as nucleon scattering data. The SPE and TBME used to generate wavefunctions for nuclear structure calculations can be obtained from a realistic nucleon-nucleon (NN) interaction, possibly including a 3-nucleon (3N) interaction, and then renormalized to the valence space relevant to investigation through various techniques. Modern techniques for renormalization include: many-body perturbation theory [20], shell-model coupled-cluster methods [21], valence-space in-medium similarity renormalization group (VS-IMSRG) methods [22], and others. The results of this work were obtained with the aid of VS-IMSRG methods.

In the process of producing our final effective interaction, we sampled an array of various ab initio interactions and ultimately settled on a choice of two for comparative purposes. Both of the chosen interactions were obtained in collaboration with B.C. He and S. R. Stroberg at the University of Notre Dame from the EM 1.8/2.0 NN+3N interaction [23] in a harmonic oscillator basis with frequency $\hbar\omega = 12$ MeV, truncated to 13 major shells ($2n + l \leq e_{max} = 12$). He and Stroberg normal-ordered with respect to the Hartree-Fock ground state of the reference and discarded the residual 3N interaction. They then decoupled the $\pi j4$ valence space using the Magnus formulation of the IMSRG. The results labeled IMSRG(2) are obtained with the standard approximation [22], truncating all operators at the two-body level throughout the flow, including inside the nested commutators. This IMSRG(2) served as the first ab initio interaction as input to our data fit

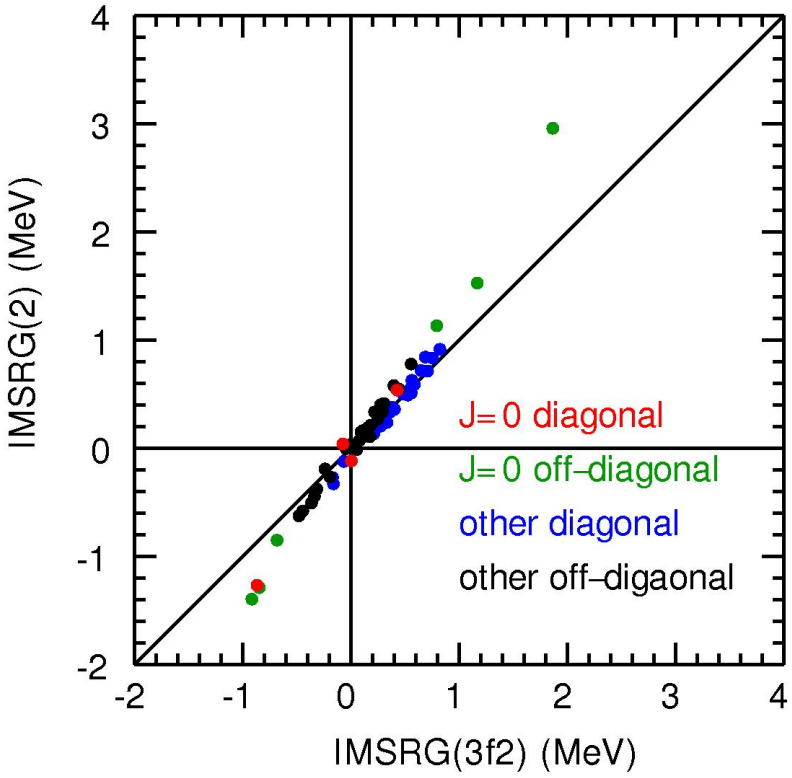

Figure 3.2 Comparison of the TBME obtained with the two versions of the IMSRG method - the y-axis involves the two-body truncation and the x-axis involves the factorized approximation. The TBME are colored according to the type of overlap that they describe.

program.

In the process of analyzing the results of our fit of this starting IMSRG(2) interaction, He and Stroberg introduced a correction in which intermediate three-body operators arising in nested commutators are incorporated by rewriting the double commutator in a factorized form while maintaining the same computational scaling as the IMSRG(2) approximation [24]. As in ref. [24], He and Stroberg included factorized terms with a one-body intermediate during the flow, and included terms with a two-body intermediate at the end of the flow. They performed the procedure for two different references, ^{78}Ni and ^{100}Sn, corresponding to empty and full valence spaces, respectively, and we took the average of the two resulting valence space Hamiltonians as our starting point for the fitting procedure. This interaction called IMSRG(3f2) served as the second ab initio interaction as input in our data fit program.

The development of this factorization method served as an opportunity to evaluate several things at once: the efficacy of the method in producing a more realistic ab initio interaction, an estimation of the uncertainty of the model parameters used for fitting, and an estimation of the uncertainty of observables predicted by our Hamiltonian as a function of the ab initio parameter values. Intuitively, the more realistic the ab initio Hamiltonian is, the less it needs to be modified to produce results that agree with experimental results. Shown in FIG. 3.2 is a comparison of the TBME obtained with the IMSRG(2) and IMSRG(3f2) approximations, indicating the magnitude of the uncertainty due to the many-body truncation. These uncertainties propagate into our effective Hamiltonians, and ultimately the resulting wavefunctions and calculations made with them. The main difference between these initial interactions is that the $J = 0$, $T = 1$ TBME are about 30 percent weaker for IMSRG(3f2) compared to those of IMSRG(2).

3.4 The p35-i3 Hamiltonian

This thesis is focused on the state-of-the-art effective interaction for the N=50 nuclei, encapsulated in a Hamiltonian that we have named p35-i3 for the model space called $\pi j4$. This model space name is a nod to a much larger model space called the $jj44$ space, which contains the same single-particle orbits for neutrons in addition to protons, and for which another class of Hamiltonians has been developed; an early example of such a Hamiltonian is given in [14]. Here, π indicates that the Hamiltonian is applied to a model space consisting only of proton orbits (not neutrons), and $j4$ indicates that these orbits are the four j orbits $\{0f_{5/2}, 1p_{3/2}, 1p_{1/2}, 0g_{9/2}\}$. The structure of all nuclei between ^{78}Ni and ^{100}Sn is described by filling these orbits with protons, and realistic wavefunctions for their states are comprised of linear combinations of the various configurations that these protons can make in these 4 orbits.

Figure 1.8 shows a calculation of single-particle occupations in the ground state of ^{78}Ni; the purpose of this figure is to illustrate the orbits of our model space (contained in the dashed box) and the occupied and unoccupied orbits that lie outside the model space. There are two columns of orbits, one for protons and one for neutrons, and the orbits with circles in them are filled orbits outside of the model space; these filled orbits give us the binding energy of ^{78}Ni and serve as the E_0

zero-body scalar term in our Hamiltonian. The four orbits in the dashed box have single-particle energies ϵ_α, which are scalars that multiply the one-body number operator of our Hamiltonian. Both the filled and unfilled orbits outside of the dashed box are inactive in our model space in the sense that our model contains no information on configurations involved with these orbits and no information about interaction between these configurations. In a real nucleus every orbit outside of the dashed box contributes to the observed properties of the nuclei we discuss here; the computational cost of including all orbits into a calculation is infeasible, which is why we use a truncated model space and why our interactions are called "effective." It is the influence of these orbits outside the model space that leads to the notion of intruder states - their influence intrudes upon the model space.

The p35-i3 interaction contains 65 scalar TBME $V_J(\alpha\beta;\gamma\delta)$ that multiply the two-body transition density operators described in Section 2.2.1. Together, the 4 single-particle energies and the 65 TBME comprise the set of parameters that can be fitted to experimental data. These parameters are first calculated and renormalized to our truncated model space using the ab initio methods described in the previous section, and these tend to provide wavefunctions that have substantial deviations with experiment. The starting Hamiltonian ultimately depends on the ab initio methods used to calculate the TBME, and in this thesis we examine and discuss the results of two different ab initio methods. The final result of the fitting yields two different Hamiltonians: p35-i2 and p35-i3. The characters i2 and i3 denote which ab initio were used to obtain the starting Hamiltonian, while p35 denotes how many linear combinations of parameters were varied to obtain the fitted Hamiltonian. The reasoning and method for varying linear combinations of parameters (and this many specifically) are discussed in the following chapter.

CHAPTER 4

FITTING METHODS

This chapter outlines the fitting procedure used to update the parameters of our Hamiltonian and quantify the uncertainty of predictions. The first section outlines the χ^2 fitting procedure for the parameters of our Hamiltonian, as well as the reformulation of the minimization solution in terms of the Singular Value Decomposition method (SVD). The second section expands on the first by describing the process by which we fit linear combinations of parameters to experimental data and use an inverse transformation to recover the updated Hamiltonian parameters. The third section introduces the Monte Carlo Cross-Validation method (MCCV) as a means of model evaluation, in particular MCCV is used to indicate the optimal number of VLC's to fit to experimental data in our fitting algorithm, and the RMSD between our Hamiltonian predictions and the validation data gives a measure of the theoretical uncertainty. Historically in fits to nuclear shell model Hamiltonians such as this, the uncertainty estimates have been quoted as the RMSD between the fitted Hamiltonian predictions and the full data (including the data used to fit the training set) [14]; this provides a potentially large underestimate of the uncertainty of the Hamiltonian to predict data that were not part of the training set.

4.1 Singular Value Decomposition (SVD) Method

Initial Procedure: χ^2 Minimization

Our starting Hamiltonian has a set of parameters $\vec{p}^{\,s} = (p_1^s, \cdots, p_{N_p}^s)$. This Hamiltonian defines a starting set of eigenvectors $|\phi_k^s\rangle$ that can be used to calculate operator overlaps β_i^k so that each associated eigenvalue λ_k can be calculated in Equation 2.16. Then we seek to minimize the ℓ^2-norm of the residual ($\vec{\chi}$) between the N_d measured experimental energies and calculated energy eigenvalues:

$$\min_{\vec{p}\in\mathbb{R}^{N_p}} \chi^2 = \min_{\vec{p}\in\mathbb{R}^{N_p}} \sum_{k=1}^{N_d} \left(\frac{E_k^{exp} - \lambda_k(\vec{p})}{\sigma_k} \right)^2 \tag{4.1}$$

where $\sigma_k^2 = \left(\sigma_k^{exp}\right)^2 + \left(\sigma_k^{th}\right)^2$. We can reorganize the fitting by expanding λ_k and defining the expected energy contribution from $H^1(\vec{p})$ in Equation 2.15 to be $\epsilon_k^{exp} \coloneqq E_k^{exp} - E_k^0$. Now, our χ^2

minimization looks like:

$$\min_{\vec{p}\in\mathbb{R}^{N_p}} \chi^2 = \min_{\vec{p}\in\mathbb{R}^{N_p}} \sum_{k=1}^{N_d} \left(\frac{\epsilon_k^{exp} - \epsilon_k(\vec{p})}{\sigma_k} \right)^2 \tag{4.2}$$

We further simplify the notation by rewriting our data components $z_k^{exp} \coloneqq \epsilon_k^{exp}/\sigma_k$ and then considering the model components:

$$z_k(\vec{p}) = \frac{\epsilon_k(\vec{p})}{\sigma_k} = \sum_{i=1}^{N_p} p_i \frac{\beta_i^k}{\sigma_k} \tag{4.3}$$

We can arrange the components of the experimental data in a data vector $\vec{z}^{exp} = [z_1^{exp}, \cdots, z_{N_d}^{exp}]^T$, and similarly for the model components, we can represent a model vector through matrix-vector multiplication:

$$\begin{bmatrix} z_1(\vec{p}) \\ \vdots \\ z_{N_d}(\vec{p}) \end{bmatrix} = \begin{bmatrix} \beta_1^1/\sigma_1 & \beta_2^1/\sigma_1 & \cdots & \beta_{N_p}^1/\sigma_1 \\ \beta_1^2/\sigma_2 & \beta_2^2/\sigma_2 & \cdots & \beta_{N_p}^2/\sigma_2 \\ \vdots & \vdots & \ddots & \vdots \\ \beta_1^{N_d}/\sigma_{N_d} & \beta_2^{N_d}/\sigma_{N_d} & \cdots & \beta_{N_p}^{N_d}/\sigma_{N_d} \end{bmatrix} \begin{bmatrix} p_1 \\ \vdots \\ p_{N_p} \end{bmatrix} \tag{4.4}$$

If we recognize that $\frac{\beta_j^k}{\sigma_k} = \frac{\partial z_k(\vec{p})}{\partial p_j}$ then the matrix above must by definition be the transposed Jacobian (J^T) of the vector-valued function $\vec{z}(\vec{p}) = [z_1(\vec{p}), \cdots, z_{N_d}(\vec{p})]^T$. This allows us to re-express our χ^2 minimization as:

$$\min_{\vec{p}\in\mathbb{R}^{N_p}} \chi^2 = \min_{\vec{p}\in\mathbb{R}^{N_p}} \|\vec{z}^{exp} - J^T\vec{p}\|^2 \tag{4.5}$$

Minimizing this with respect to each parameter p_j gives N_p equations of the form:

$$\begin{aligned} \frac{\partial \chi^2}{\partial p_j} &= 2 \sum_{k=1}^{N_d} \left(\frac{\epsilon_k^{exp} - \epsilon_k(\vec{p})}{\sigma_k} \right) \left(-\frac{1}{\sigma_k} \frac{\partial \epsilon_k(\vec{p})}{\partial p_j} \right) \\ &= -2 \sum_{k=1}^{N_d} \left(\frac{\epsilon_k^{exp} \beta_j^k}{\sigma_k^2} - \sum_{i=1}^{N_p} p_i \frac{\beta_i^k \beta_j^k}{\sigma_k^2} \right) = 0 \end{aligned} \tag{4.6}$$

which leaves us with the condition that:

$$\sum_{k=1}^{N_d} \frac{\epsilon_k^{exp} \beta_j^k}{\sigma_k^2} = \sum_{k=1}^{N_d} \sum_{i=1}^{N_p} p_i \frac{\beta_i^k \beta_j^k}{\sigma_k^2} \tag{4.7}$$

Notice that if we now define the quantities:

$$e_j \coloneqq \sum_{k=1}^{N_d} \frac{E_{exp}^k \beta_j^k}{\left(\sigma^k\right)^2} \quad \text{and} \quad G = \begin{bmatrix} \gamma_{11} & \cdots & \gamma_{1p} \\ \vdots & \ddots & \vdots \\ \gamma_{p1} & \cdots & \gamma_{pp} \end{bmatrix} \tag{4.8}$$

where

$$\gamma_{ij} \coloneqq \sum_{k=1}^{N_d} \frac{\beta_i^k \beta_j^k}{\left(\sigma^k\right)^2} = \sum_{k=1}^{N_d} \frac{\beta_j^k \beta_i^k}{\left(\sigma^k\right)^2} = \gamma_{ji} \in \mathbb{R} \tag{4.9}$$

we can rewrite the N_p equations as a single vector equation:

$$\vec{e} - G\vec{x} = 0 \quad \longrightarrow \quad \vec{x} = G^{-1}\vec{e} \tag{4.10}$$

Since the matrix G is real and symmetric, it is diagonalizable. The step of solving for $\vec{x}$ shown in equation 4.10 is only possible if G is invertible, meaning that none of the eigenvalues of the matrix G are 0. This process can be used to find a new $\vec{x}$ that can be used to calculate new eigenvalues for the new eigenstates $|\phi'_k\rangle$, repeating until convergence.

Note : G^{-1} is referred to as the error matrix because its diagonal entries are the square of parameter errors and the off-diagonals are related to correlations between parameters.

SVD

The Hamiltonian parameters are often highly correlated, and updated parameters obtained from Equation 4.10 will not only be dramatically different from their *ab initio* values, but will result in a Hamiltonian that generally performs quite poorly on data outside of the training set. In other words, the solution in Equation 4.10 results in a overfitting of the Hamiltonian, as can be seen on the right extremes of both graphs in Figure 4.1. One method of ameliorating this situation is to use the SVD of the G^{-1} matrix, allowing the fit to be re-expressed in terms of an orthonormal basis of uncorrelated SVD parameters. Since G is real and symmetric, its SVD is identical to an eigendecomposition; the SVD for G and G^{-1} are:

$$G = ADA^T \quad \text{and} \quad G^{-1} = AD^{-1}A^T \tag{4.11}$$

where:

- $D \in \mathbb{R}^{p\times p}$ is a matrix of diagonal positive elements $D_{ii} > 0$.
- $A \in \mathbb{R}^{p\times p}$ is a rotation matrix whose columns form an orthonormal basis of our SVD parameter space.
- D^{-1} is a diagonal matrix whose elements are inverses of the elements of D - that is:

$$\left[D^{-1}\right]_{ii} = d_i = \frac{1}{D_{ii}} \tag{4.12}$$

With these substitutions in the result of our minimization, we have the following:

$$\vec{x} = AD^{-1}A^T\vec{e} \quad \longrightarrow \quad A^T\vec{x} = D^{-1}A^T\vec{e} \tag{4.13}$$

Now we express the rotations of $\vec{x}$ and $\vec{e}$

$$\vec{y} = A^T\vec{x} \quad \text{and} \quad \vec{c} = A^T\vec{e} \tag{4.14}$$

resulting in

$$\vec{y} = D^{-1}\vec{c} \quad \longrightarrow \quad y_i = d_i c_i \tag{4.15}$$

Here the uncorrelated SVD parameters y_i are expressed as a linear combination of the Hamiltonian parameters x_i with associated errors d_i - explicitly:

$$\vec{y} = A^T\vec{x} = \sum_{l=1}^{p} x_l \vec{a}_l^T \quad \longrightarrow \quad y_i = \sum_{l=1}^{p} x_l \left[A^T\right]_{il} \tag{4.16}$$

where $\vec{a}_l^T$ is the l'th column of A^T. When d_i is large, the SVD parameters y_i experience a large change from a correspondingly small change in the data c_i, meaning that the corresponding linear combination of Hamiltonian parameters y_i is poorly determined by the given data set. We can establish a cutoff criterion on what is poorly determined linear combination of Hamiltonian parameters y_i based on the magnitude of the corresponding d_i

4.2 Fitting Algorithm

1. Starting from the best available Hamiltonian parameters $\vec{x}^s$ we construct and diagonalize the matrix G to obtain D_{ii} eigenvalues and the orthonormal basis for our parameter space.

2. The mutually independent SVD parameters y_i are determined in the fit of equation 4.15 (and 4.16). Explicitly:

$$y_i = d_i c_i = d_i \sum_{l=1}^{p} e_l \left[A^T\right]_{il} \tag{4.17}$$

Concurrently, linear combinations of the starting Hamiltonian parameters are determined from the equation (5). Explicitly:

$$\vec{y}^s = A^T \vec{x}^s \quad \longrightarrow \quad y_i^s = \sum_{l=1}^{p} x_l^s \left[A^T\right]_{il} \tag{4.18}$$

3. One defines a cut-off criterion δ, and updated linear combinations $\vec{y}^a$ are defined by only adopting well-determined values y_i with respect to this cut-off and leaving starting values for the rest:

$$y_i^a = \begin{cases} y_i & (d_i \leq \delta) \\ y_i^s & (d_i > \delta) \end{cases} \tag{4.19}$$

The number of well-determined linear combinations is N_d. The cutoff criterion is established through the process of bootstrap sampling of batch data discussed in Section 4.3.

4. With the updated set of model parameters $\vec{y}^a$ one recovers the Hamiltonian parameters by inverting the rotation:

$$\vec{x}^a = (A^T)^{-1} \vec{y}^a \tag{4.20}$$

5. This set of Hamiltonian parameters takes the place of $\vec{x}^s$ as input to the first step of this algorithm and is used to obtain the next set of parameters $\vec{x}^b$. This process is repeated until convergence.

4.3 Monte Carlo Cross-Validation and Uncertainty Estimation

An essential purpose of these effective Hamiltonians is to achieve some level of predictive power; this is clearly illustrated in Figure 4.1. To obtain the scatter of points around the central fit values as well as the green points in this figure, we use the Monte Carlo cross-validation technique (MCCV) based on the work of Xu and Liang in 2001 [25]. The underlying objective of MCCV

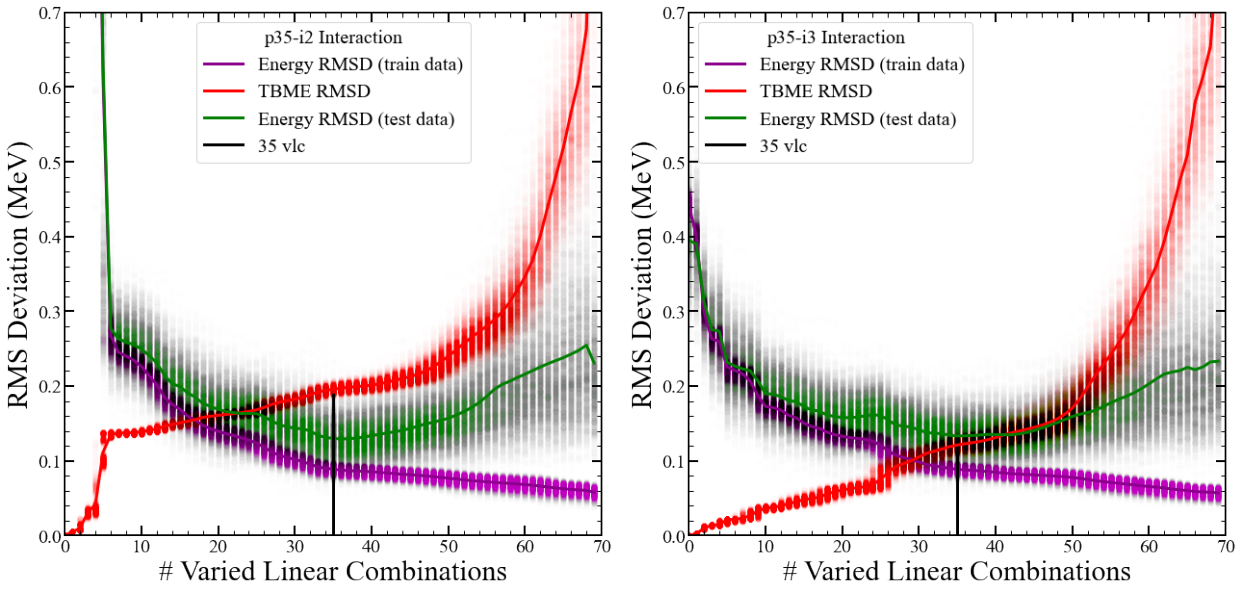

Figure 4.1 Results of the SVD fits as a function of the number of varied linear combinations (VLC) of parameters. The left-hand side shows results used to obtain the p35-i2 Hamiltonian, and the right-hand side shows results used to obtain the p35-i3 Hamiltonian. The purple points show the energy-RMSD between theory and experiment as a function of the number of VLC, and the red points show the TBME-RMSD between the IMSRG and fitted Hamiltonians. The lines are the results for the pn-i2 and pn-i3 Hamiltonians. We also show points for the 2000 batches of randomly sampled experimental training data discussed in the text, purple points for the training energy data set, and green points for the predicted data set.

is to perform calibration of the model hyperparameters (the number of VLC in this case) with the aim of improving the predictive capacity of the model. If the global data set is sufficiently large, an ensemble of replacement subsets can be sampled from the global set. The sampling is generally performed by splitting the global data set into training and validation sets randomly using Monte Carlo methods. MCCV differs from the nonparametric bootstrap sampling method in that the sampling is done without replacement, meaning that within one of training partitions each data is unique and not repeated, and the training/validation sets are generally smaller than the global set in MCCV. Unlike k-fold cross-validation, the same data can occur in different partitions of the global set, and because the training sets are not limited by the number of folds, the number of possible partitions of the data is greater in MCCV. For a global set with N_d data elements and a training set

with N_t training data, the possible number of unique training sets accessible to MCCV is:

$$\binom{N_d}{N_t} = \frac{N_d!}{N_t!(N_d - N_t)!} \tag{4.21}$$

For a data set of size N_d, Zhang [26] showed that running MCCV over $O(N_d^2)$ iterations produces results close to the result of Equation 4.21.

All known experimental data for this model space were randomly partitioned into training batches (80%) and testing batches (20%). The sampling method was as follows: All ground states were included in the training set, and a random double between 0.0 and 1.0 was drawn from a uniform probability distribution for each excited state in the complete set of available data. If the random number was between 0.0 and 0.8, the excited state was included in the training set; otherwise, it was included in the test set. This method of sampling is a modification of traditional partitioning, where the splits strictly enforce the ratio of training to validation data. Relaxation of this condition allows our algorithm to sample a larger set of possible training/validation partitions, since N_t is no longer a fixed number for each cross-validation fold. The purpose of this implementation is to augment the advantage that MCCV already has over other cross-validation methods: a larger number of unique training partitions will lead to more robust estimates of model performance. This is because a larger variety in the training data provides a more accurate indicator of how the model will generalize to data that weren't included in the training partition. In situations where the total available data is small (this work being such a case), the choice of specific data for a training partition can have a strong impact on model performance, and a different choice of training data can result in drastically different results. This method results in a distribution of possible training and testing splits shown in Figure 4.2.

The training batch was used to vary the parameters of our Hamiltonian, and the validation set was used in the calculation of RMSD - in this way our fitted Hamiltonian is predicting the results of data that it had not seen in the fitting procedure. The sampling process was repeated 2000 times to generate a distribution of calculations for each VLC and for each set of starting Hamiltonian parameters. The ensemble of Hamiltonians generated by this cross-validation method allows for calibration of the model hyperparameters (the number of VLC in this work) and provides a more

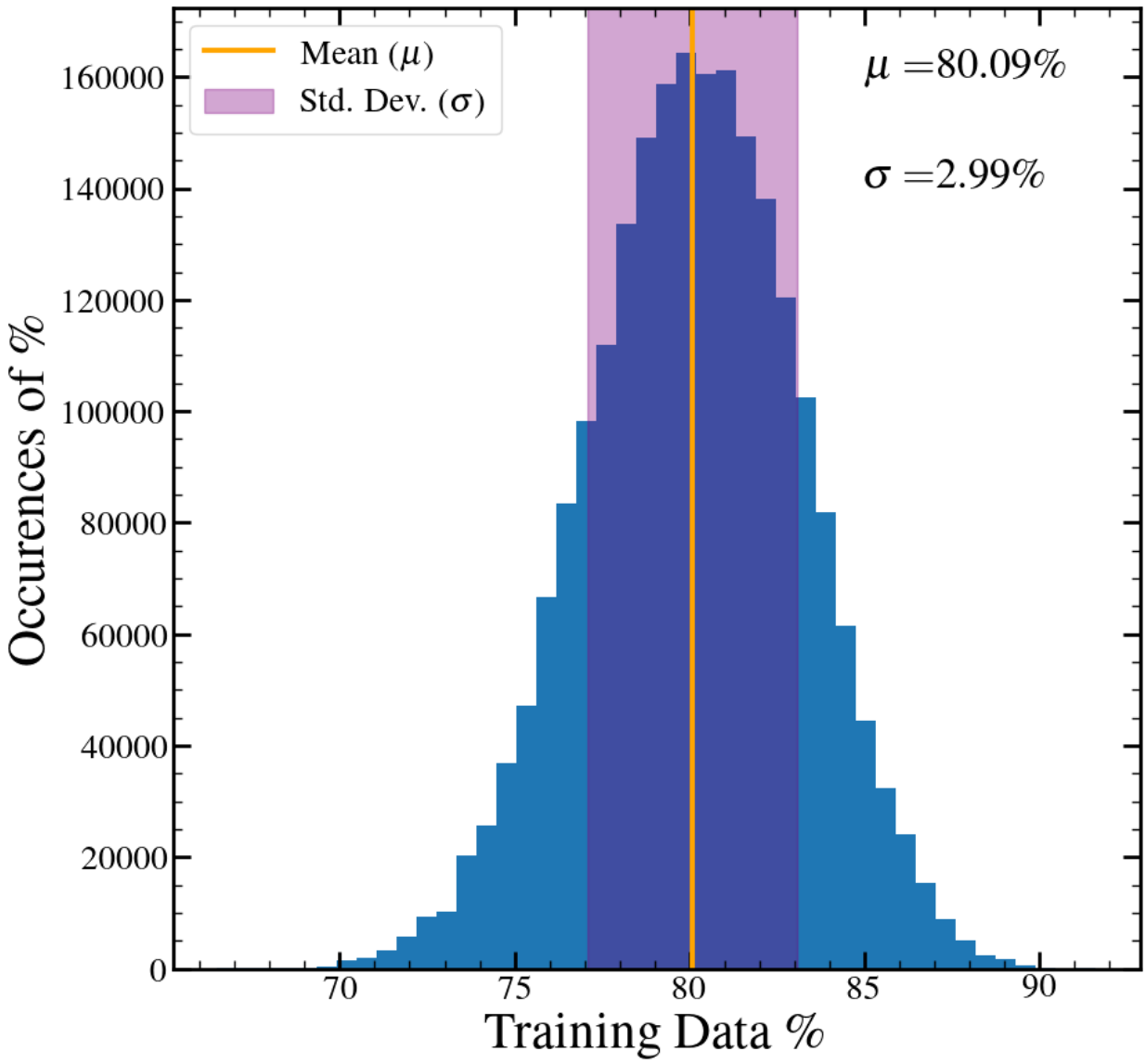

Figure 4.2 The percentage of excitation energy data used in the training set relative to all known excitation energy data. One can see that the sampling method results in a distribution of training sets that is roughly Gaussian with a mean centered on the chosen splitting criterion of 80% with a standard deviation of σ = 2.99%. The occurrences in this plot are added over all VLC iterations, so the average number of occurrences within a given VLC should be all counts in this graph divided by 70. This distribution comes from performing 32,000 cross-validations for each VLC.

robust metric for estimating model uncertainty than a calculation of the RMSD between experiment and theory for a fit involving the full set of known data.

The green curve highlights the predictive capacity of each Hamiltonian as the number of VLC's is increased. It can be seen that each Hamiltonian approaches an energy-RMSD minimum (a maximum for the predictive power) at about 35 VLC. In fact, the RMSD is reasonably small in the range of 15-35 VLC. This is significant because it indicates that we can achieve some benchmark level of predictive power with fewer modifications to our initial Hamiltonian with the factorization method given by [24]. This becomes critically significant when one considers effective Hamiltonians for larger model spaces where producing these effective Hamiltonians and using them to make predictions becomes computationally intensive, or where data are sparse or redundant in terms of constrained parameters (as is the case described in this thesis).

4.4 Algorithm Workflow

This section serves to visually show the algorithm for producing our fitted Hamiltonian. The number of batches for the MCCV algorithm is specified in advance as N_b, while the maximum number of singular values and linear combinations of parameters to fit in the SVD is N_s. For the purposes of this diagram, s refers to the number of singular values (VLC's) involved in the current loop of the fitting process, while b indicates how many batches of training/validation split have been used for a given s. The MCCV loop closes when $b = N_b$, and the larger loop over singular values closes when $s = N_s$. The total number of SVD fits carried out by this algorithm is generally $(N_s + 1) \times N_b$, and for the work considered here, we have $N_s = 69$ and $N_b = 2000$. The stage of identifying the optimal value of s involves collecting the RMSD calculations performed by all MCCV splits and identifying the global minimum. The information contained in the RMSD allows for uncertainty quantification as well: For a given number of VLC, one simply takes the average of the N_b RMSD calculations between the predictions and the validation data set. The inverse transformation of the SVD allows one to obtain the updated Hamiltonian parameters that are used to generate new wavefunctions and new overlaps (β). This process is repeated until the wavefunctions have converged, and the Hamiltonian becomes self-consistent.

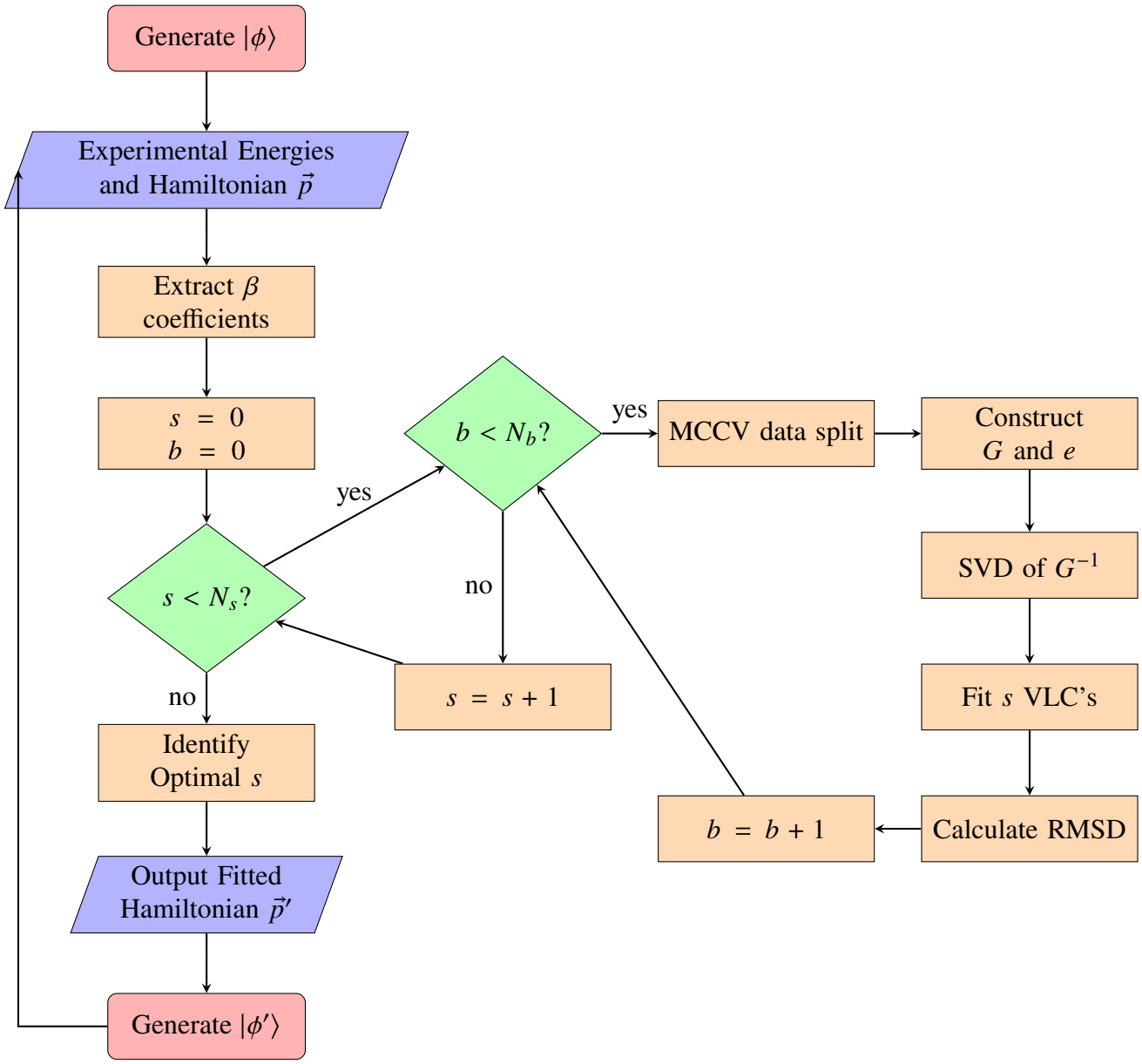

Figure 4.3 The algorithm starts with wavefunctions $|\phi\rangle$ generated from an older set of Hamiltonian parameters $\vec{p}$. These are used to generate a set of operator overlaps β associated with $\vec{p}$ (see Equation 2.16). The end result is a new set of Hamiltonian parameters $\vec{p}'$ used to generate a new set of wavefunctions $|\phi'\rangle$, which are used to generate a new set of overlaps β' and the algorithm is run again until convergence. The index s indicates the number of singular values being fitted, and the index b indicates and the batch iteration for fitting. N_s indicates the total number of singular values and N_b indicates total number of batches.

CHAPTER 5

RESULTS AND DISCUSSION OF FITTED HAMILTONIAN

5.1 Energy Spectra

The 65 TBME of our starting IMSRG(3f2) Hamiltonian and 4 SPE parameters were fitted to the experimental data to produce the p35-i3 Hamiltonian and its corresponding wavefunctions [1]. In particular, the data used were the well-determined binding energies and energy levels (with corresponding spins) of nuclear states in all nuclei relevant to the $\pi j4$ model space. Naturally, the first set of results we want to compare with experiment will be the binding energies and energy spectra predicted by the p35-i3 Hamiltonian. One of the significant binding energies predicted in our Hamiltonian is of ^{100}Sn with a value of -825.120 MeV, which is within the experimental uncertainty of -825.163 ± 0.283 MeV.

Rather than going through and examining each nucleus exhaustively, in this section, we will show a few examples which highlight interesting results. A complete collection of diagrams comparing the experimental data and our predictions is given in Appendix A. It should be noted that all such diagrams only show excitations up to 6 MeV; The predictions of excitations from the p35-i3 Hamiltonian (and indeed the experimental excitations for some nuclei) extend well beyond this purely visual limit. It should be noted that every state appearing on the theory side of these panels must exist experimentally. However, as discussed in Section 3.2.1 there will also be experimental intruder states that are not contained in the $\pi j4$ theory.

There is excellent agreement between the experimentally known spectra for all nuclei within uncertainty across a range of excitation energies. The energy RMSD between the predictions from p35-i3 wavefunctions and the experimentally well-determined states whose values were not used in the fitting procedure is roughly 150 keV. In addition to agreeing well with experimentally well-determined energy states, we predict states whose energies and/or spins are either not well-determined experimentally, or not known in experiment at all.

Looking at Figure 5.1, we see the comparison between experiment and theory for the spectrum of ^{79}Cu. There are many states in this nucleus that we do not predict because they are intruder states,

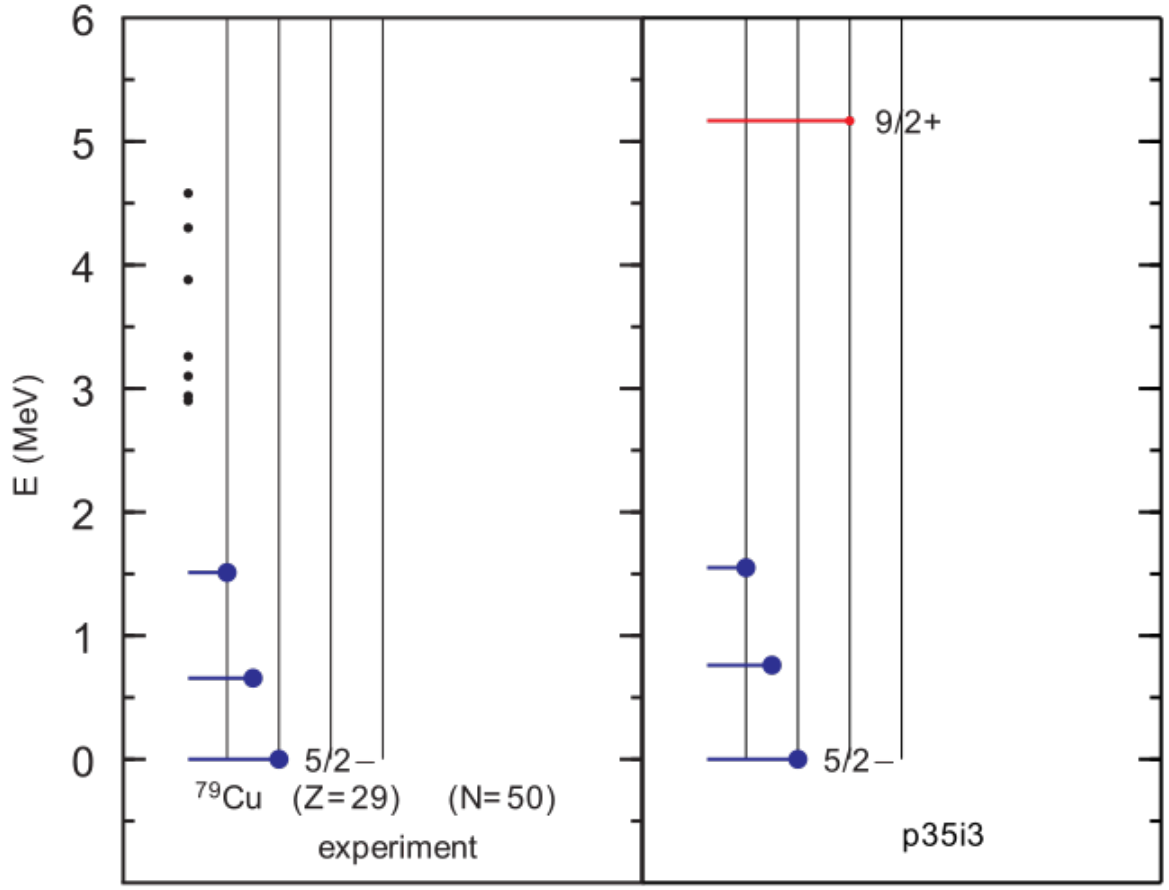

Figure 5.1 A comparison of the energy spectra between experiment and theory for ^{79}Cu. The length of each line indicates the spin, the red/blue color indicates positive/negative parity, a large dot indicates that an experimental state was used in the fit, and a black dot indicates that the energy of the state is determined but the J-value is not.

arising from particle-hole excitations of neutrons involving transitions between orbital configurations $\{1p_{1/2}, 0g_{9/2}\} \rightarrow \{0g_{7/2}, 1d_{5/2}\}$ across the $N = 50$ shell gap, and particle-hole excitations of protons involving transitions $0f_{7/2} \rightarrow 0f_{5/2}$ across the $Z = 28$ shell gap, as discussed in Sect. 3.2.1. The spin-parity of the ground state is not measured; we extrapolate the spin value from the lighter odd-even isotopes of Copper [18]. Additionally, we predict the $9/2^+$ state, which is significant because it is used to determine the single-particle energy of the $0g_{9/2}$ orbital. This nucleus is the most sensitive probe of the $0g_{9/2}$ single-particle energy because the ^{79}Cu contains only one valence proton in our model space, and as a result the evaluation of Equation 2.16 does not involve any two-body matrix elements, only single-particle energies with the background binding energy of ^{78}Ni. Additionally, we predict the analogous spectrum of ^{99}In, whose structure is a single-hole in ^{100}Sn, resulting in an energy spectrum whose excited states have spins ordered opposite to ^{79}Cu. The spectral comparison of ^{99}In is shown in Figure A21 which is found in Appendix A. The $1/2^-$ and $3/2^-$ states in ^{99}In are based on the observed states in ^{131}In [27], which is an analogous semi-magic Indium nucleus with neutrons filled up to the $N = 82$ shell gap. Experimental verification of the extrapolations of these excited states in ^{79}Cu and ^{99}In is needed.

Figure 5.2 shows a similar comparison of the structure of the even-even ^{80}Zn nucleus. In our model, this nucleus is two valence protons, making it the first nucleus in our model space to be impacted by TBME. Aside from the excellent agreement between experiment and theory, we see that there are many states predicted that are unobserved or undetermined from experiment. An interesting observation is the prediction of a second 4^+ state nearly coincident with the predicted second 2^+ state. The absence of negative parity states in this plot is solely to do with the axis scale. Negative parity states only begin to appear in this nucleus when pairing between the protons is broken, allowing for configurations in which one of the protons is excited into the $0g_{9/2}$ coupled to the other in the fp shell, and this occurs a little after 6 MeV in energy.

Figure 5.3 shows the spectral comparison between experiment and theory for the odd-even ^{97}Ag nucleus, which is 19 valence protons in our model. The larger number of active protons in this nucleus along with a large amount of configuration mixing between the fp shell and $0g_{9/2}$

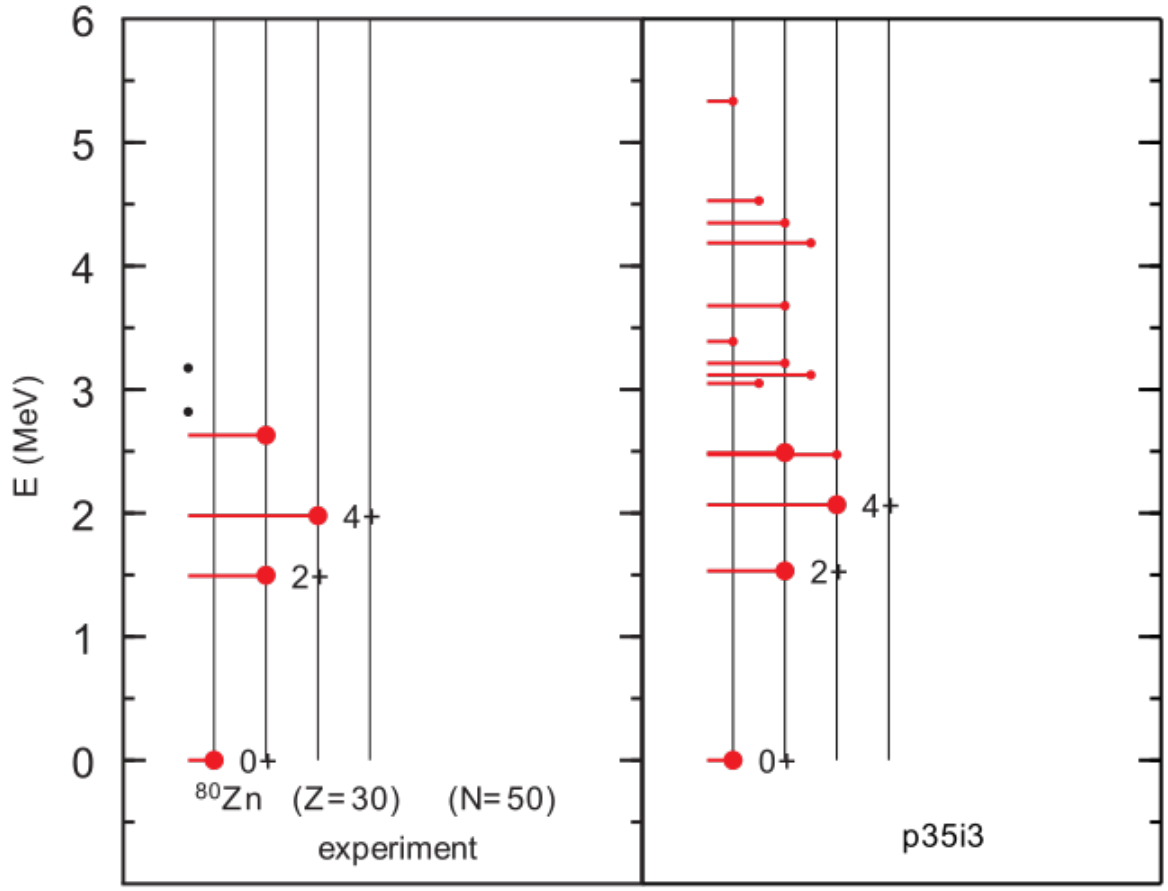

Figure 5.2 A comparison of the energy spectra between experiment and theory for ^{80}Zn.

orbit leads to a rich low-lying spectrum for this nucleus, with a mingling of positive and negative parity energy states. The ordering and energy values predicted for this nucleus agree very well with what has been measured experimentally. Given the orbits in our model space and the number of protons in ^{97}Ag, the largest spin that we can predict for this nucleus is $J^{\pi} = 21/2^{+}$, the lowest energy one corresponding to a seniority $v = 3$ configuration of the $0g_{9/2}$ orbit on a filled fp shell, which means that the $23/2^{+}$ state observed in the experiment must be an intruder state involving transitions between orbital configurations $\{1p_{1/2}, 0g_{9/2}\} \rightarrow \{0g_{7/2}, 1d_{5/2}\}$ across the $N = 50$ shell gap.

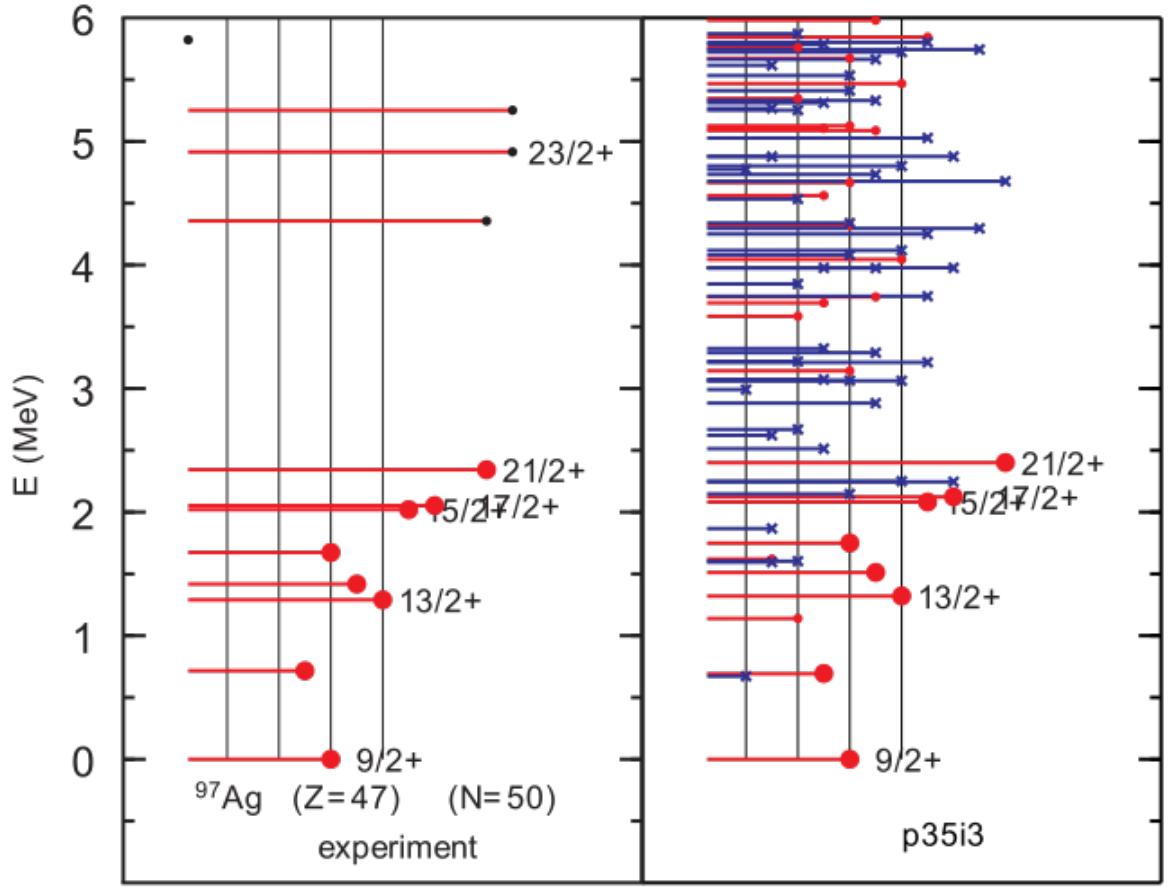

Figure 5.3 A comparison of the energy spectra between experiment and theory for ^{97}Ag. The high-spin states above 4 MeV on the experiment side which have a black dot at the end of the line indicate that the spin is tentatively assigned.

These selected nuclei serve to illustrate the variety of complexity captured by the p35-i3 Hamiltonian, but also the amount that we still need to know about these nuclei.

5.2 Electromagnetic Properties

Equipped with the wavefunctions of the p35-i3 Hamiltonian, electromagnetic observables corresponding to various operators, such as the $M1$ and $E2$ operators, can be calculated and compared to experiment. These observables include magnetic dipole moments, electric quadrupole moments, $M1$ transitions, and $E2$ transitions between states. In the following sections, we will first present the means used to quantify theoretical uncertainty, and then we will discuss some of the comparisons to experimental data. There are many more calculations and predictions made from these wavefunctions than could reasonably be shown in this thesis; these are illustrative of some of the more motivating examples for future experiments and also serve to interpret the structure of some of the known electromagnetic observables in the literature. A specific example of the results that we calculate from these wavefunctions is given in Appendix B for ^{81}Ga. There is such a .deo file for every nucleus in the $\pi j4$ model space.

5.2.1 Uncertainty Quantification

As mentioned in Section 3.3, the various ab initio methods used to construct and truncate ab initio Hamiltonians induce uncertainty in the wavefunctions associated with them and, by extension, in all of the predictions made using those wavefunctions. We can quantify this uncertainty by generating a series of calculations for a given operator using effective Hamiltonians constructed from different ab initio starting points. These ab initio starting points are the IMSRG(2) and IMSRG(3f2) discussed in Section 3.3, and the effective Hamiltonians constructed from the fitting procedure are the p35-i2 and p35-i3 Hamiltonians, respectively. From these Hamiltonians, a root-mean squared deviation (RMSD) between the various calculations is used as an estimate of the theoretical uncertainty in their associated observables.

As shown in Figures 5.4 and 5.5, the theoretical uncertainty can be stratified for different nuclei or regions of nuclei. This is an important consideration, as the nuclear wavefunctions for states with $A < 88$ involve a large number of TBME that are not well-determined by the known experimental

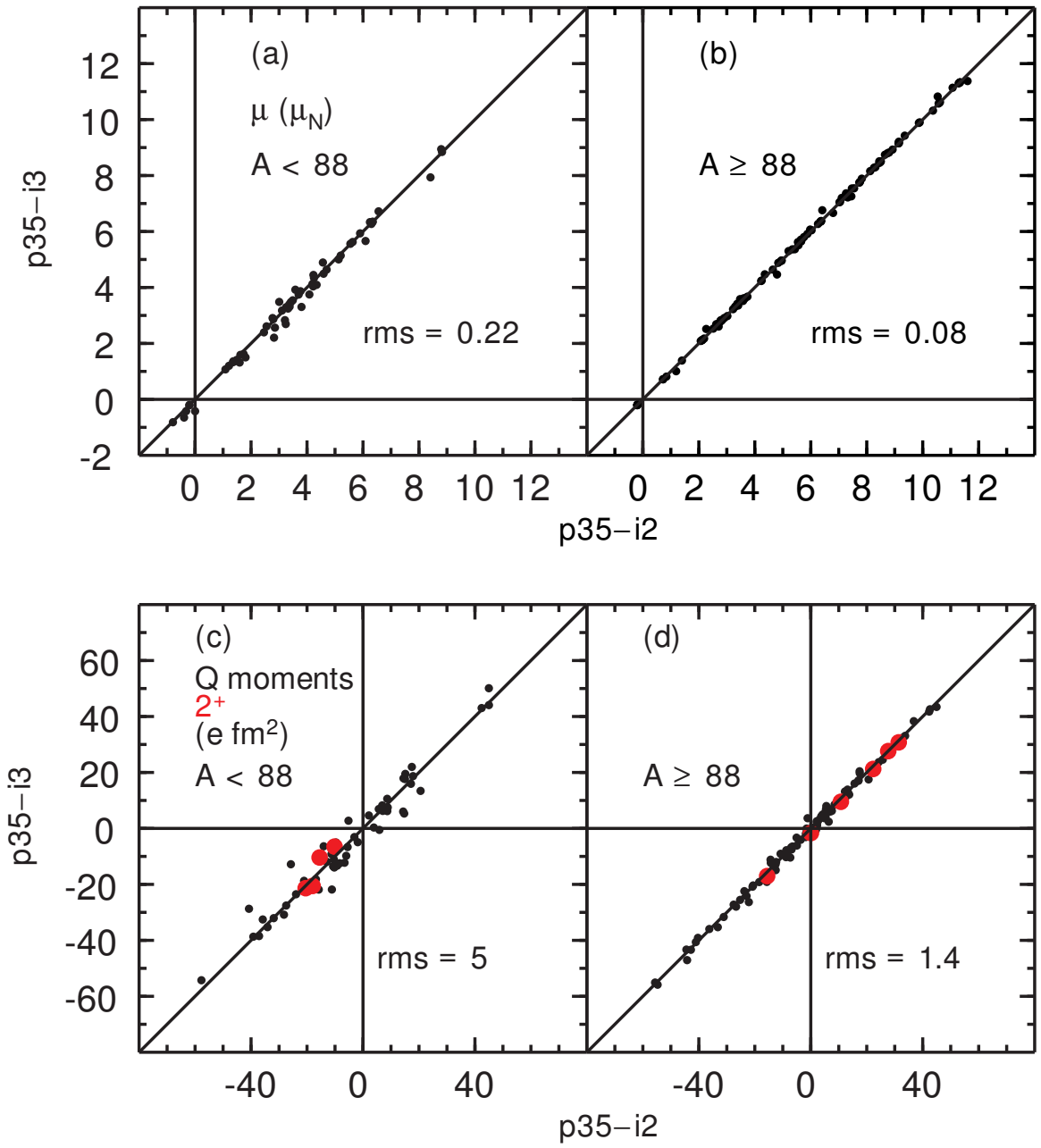

Figure 5.4 (a) and (b) show comparisons of low-lying magnetic dipole moments, while (c) and (d) show low-lying electric quadrupole moments. The red circles in (c) and (d) show the quadrupole moments of low-lying 2^+ states in even-even nuclei. The diagonal line of slope 1 represents a perfect agreement between the two Hamiltonians. The rms values shown in each figure are the values used for theoretical uncertainty in shown associated calculations.

data, while the wavefunctions for nuclei with $A \geq 88$ tend to be influenced more by fewer TBME's which are well-determined by experimental data.

Figure 5.4 shows the comparisons between the electromagnetic moments predicted by the p35-i2 and p35-i3 ab initio interactions. These electromagnetic moments correspond to the low-lying states in all nuclei involved in the $\pi j4$ model space. Panels (a) and (b) show the magnetic dipole moment with a theoretical uncertainty of 0.22 μ_N for nuclei with $A < 88$, and 0.08 μ_N for those with $A \geq 88$. Panels (c) and (d) show the electric quadrupole moments with theoretical uncertainties of 5 $e \cdot \text{fm}^2$ and 1.4 $e \cdot \text{fm}^2$ for $A < 88$ and $A \geq 88$, respectively. The 2^+ states are colored red, and these are usually the first states in even-even nuclei to demonstrate collectivity.

Figure 5.5 shows comparisons between the electromagnetic transitions predicted by the same Hamiltonians, and as in the case of the electromagnetic moments, these transitions are between low-lying states in all nuclei in the $\pi j4$ model space. In this figure, panels (a) and (b) give the $B(M1)$ values, with a theoretical uncertainty of 0.09 (μ_N^2) and 0.023 (μ_N^2) for $A < 88$ and $A \geq 88$, respectively; Panels (c) and (d) show the values of $B(E2)$ with a theoretical uncertainty of 31 $e^2 \cdot \text{fm}^4$ and 8 $e^2 \cdot \text{fm}^4$ for $A < 88$ and $A \geq 88$, respectively. The $2^+ \rightarrow 0^+$ transitions are shown in red for even-even nuclei, and these generally involve the most collectivity among the transitions that occur in a nucleus.

5.2.2 Magnetic Dipole Moments

The magnetic dipole moments are calculated by Eq. 2.25, where the $O(M1)$ operator is given by Eq. 2.24. Shown in Figure 5.6 are comparisons of the magnetic dipole moments for the nuclei in the $\pi j4$ model space. Here we use the p35-i3 Hamiltonian and compare the results with it's corresponding experimental measurements, and the experimental data shown comprise a complete set of the well-determined low-lying magnetic moments in nuclei across the $\pi j4$ model space. From this figure, we see that the agreement between experiment and theory is excellent within the uncertainties in both quantities. This data is also shown in Tables 5.1 and 5.2 together with calculations using the older n50j (1988) [13] and jj44a (2004) [14] Hamiltonians. A more detailed display of a subset of these magnetic moments is shown in Figure 5.7.

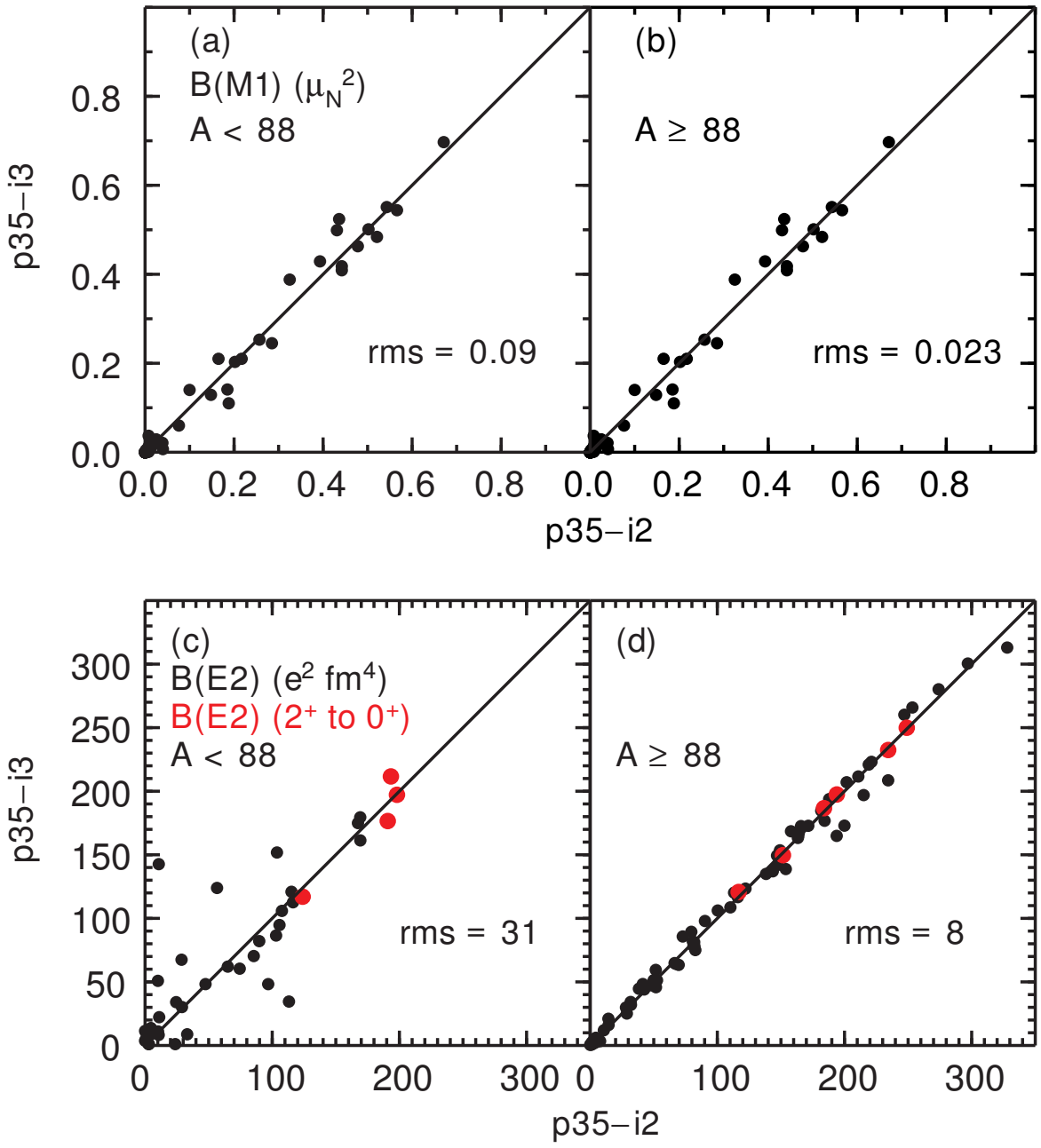

Figure 5.5 (a) and (b) show comparisons of low-lying $M1$ transition strengths, while (c) and (d) show low-lying $E2$ transition strengths. The red circles in (c) and (d) show the $B(E2; 2_1^+ \rightarrow 0_1^+)$ transitions in even-even nuclei. The diagonal line of slope 1 represents a perfect agreement between the two Hamiltonians. The rms values shown in each figure are the values used for theoretical uncertainty in shown associated calculations.

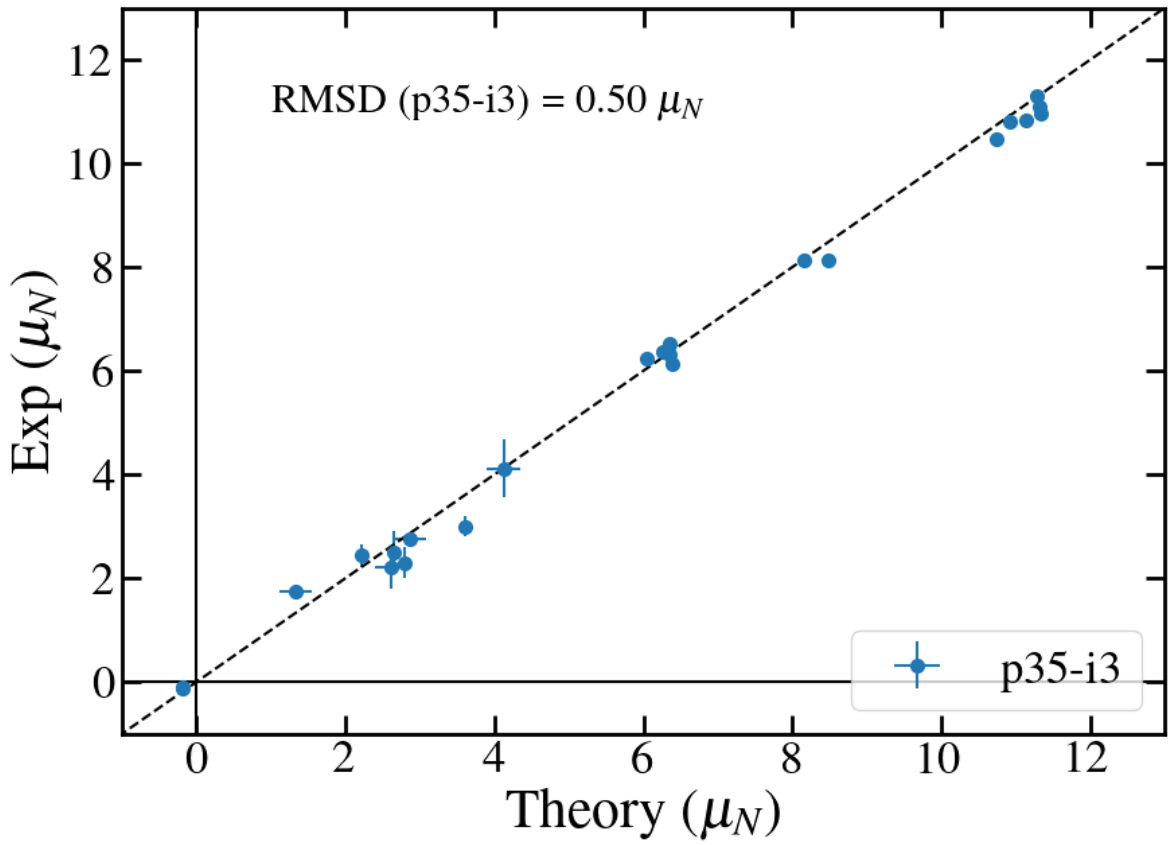

Figure 5.6 A comparison of predicted dipole values between the p35-i3 Hamiltonian and experiment. The diagonal line represents perfect agreement between theory and experiment. Theory error bars adopted from rms values in panels (a) and (b) of Figure 5.4.

Figure 5.7 shows the magnetic moments of the low-lying states in odd-even nuclei across the model space. With the exception of the $9/2^+$ state in ^{89}Y, all of these states are ground states; the excited state of ^{89}Y was included because it is structurally similar to the ground states of the odd-even nuclei with $A \geq 91$. In Figure 5.7 we observe that the nuclei in a given J^π state all have roughly the same magnetic moment, and this is in agreement with the magnetic moments experimentally observed across the model space. The relative uniformity of the magnetic moments for all nuclei of a given J^π value is due to the nature of the configurations involved in these wavefunctions. Many of the configurations involved in the wavefunctions describing these states contain even numbers of protons in single-particle orbitals having spins coupled to $J = 0^+$, and an odd number of n protons in an orbital $k = [nlj]$; these are called $[nlj]^n$ (or k^n) configurations. For example, consider the $9/2^+$ excited state of ^{89}Y shown in Figure 5.7. If we denote the configurations

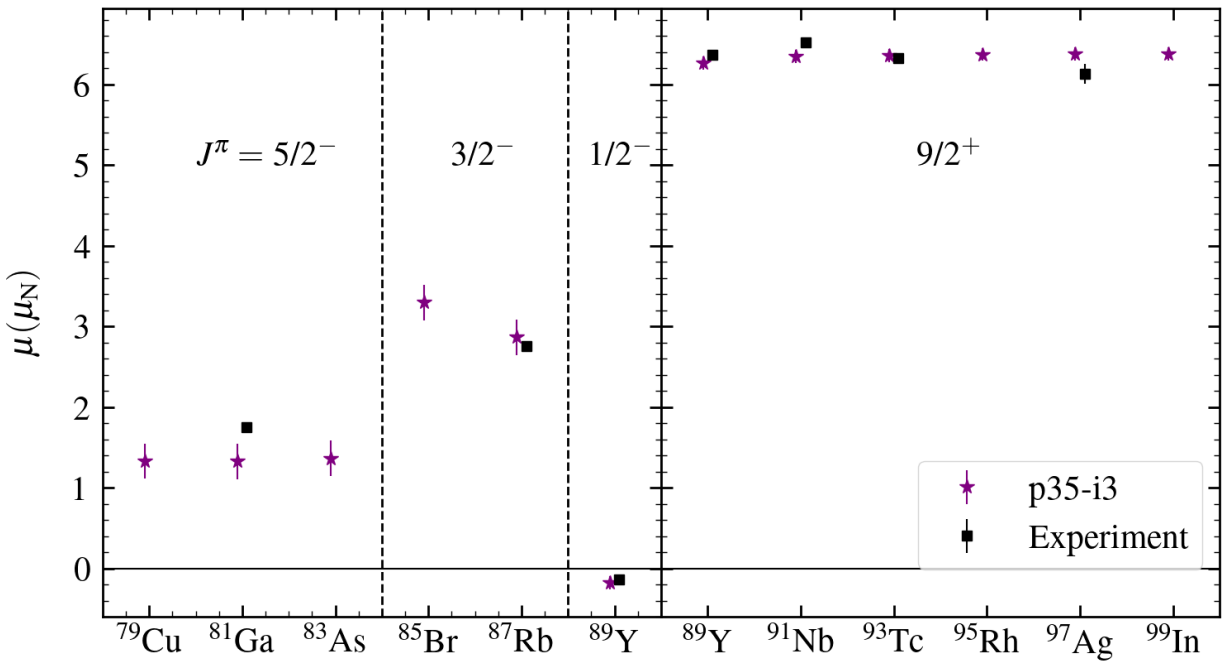

Figure 5.7 A comparison between the experiment and theory for the low-lying magnetic dipole moments in odd-even nuclei from ^{79}Cu to ^{99}In. The vertical separators indicate the nuclear spins of each of these states, and with the exception of the $9/2^+$ state in ^{89}Y, all of the shown values correspond to the ground state.

involved as the partitions $[n_{5/2}, n_{3/2}, n_{1/2}, n_{9/2}] = [n_{fp}, n_{9/2}]$ corresponding to the occupancies of the $\{0f_{5/2}, 1p_{3/2}, 1p_{1/2}, 0g_{9/2}\}$ orbitals, then the wavefunction of the $9/2^+_1$ state in ^{89}Y is composed of:

$$
\begin{aligned}
&[6, 4, 0, 1] && \rightarrow (43\%) \\
&\left[n_{fp} = \text{even}, n_{9/2} = 1\right] && \rightarrow (16\%) \\
&\left[n_{fp} = \text{even}, n_{9/2} = 3\right] && \rightarrow (22\%) \\
&\left[n_{fp} = \text{even}, n_{9/2} = 5\right] && \rightarrow (3\%) \\
&[\text{All Other}] && \rightarrow (16\%)
\end{aligned}
$$

where $n_{fp} = \text{even}$ indicates that the fp orbitals below $0g_{9/2}$ all have an even orbital occupancy number, and couple primarily to $J = 0^+$ in these orbitals. We see that this $9/2^+$ excited state is dominated by $[0g_{9/2}]^n$ (odd n) configurations, with 84% of the wavefunction being described by them.

The nuclei with $J^\pi = 3/2^-$ are less uniform as a result of their wavefunctions containing a larger

amount of configuration mixing between the $1p_{3/2}$ and $1p_{1/2}$ orbitals. To elaborate more on the meaning of this, consider the magnetic moment operator defined by the rank-1 tensor:

$$T^{\lambda=1}_{\mu=0} = \hat{\mu}_z = \left[\hat{\ell}_z g^\ell + \hat{s}_z g^s\right] \mu_N \tag{5.1}$$

where g^ℓ and g^s are the corresponding g-factors for each of these operators. The free-proton values for the proton g-factors are $g^\ell_{free} = 1$ and $g^s_{free} = 5.586$; The protons we consider are in the nuclear medium, and due to working within a truncated model space, we must assign them effective g-factors to account for various effects such as polarization of the nuclear core by our valence protons and meson exchange currents. We adopt two sets of spin g-factors corresponding to the fp orbitals and the $0g_{9/2}$ orbital, and a single orbital g-factor for the entire model space, which were obtained from fits to the data in [28]. The effective spin g-factors are $g^s_{fp} = 4.694$ and $g^s_{0g9/2} = 3.593$, while the effective orbital g-factor is $g^\ell_{eff} = 1.10$. The expectation value of the single-particle magnetic moment is:

$$\begin{aligned}\mu_z &= \left\langle k, m = j \left| T^{\lambda=1}_{\mu=0} \right| k, m = j \right\rangle \\ &= \left[g^\ell \left\langle k, m = j \left| \hat{\ell}_z \right| k, m = j \right\rangle + g^s \left\langle k, m = j \left| \hat{s}_z \right| k, m = j \right\rangle\right] \mu_N\end{aligned} \tag{5.2}$$

where we see that the one-body tensor operates separately on the spatial (with $\hat{\ell}_z$) and spin (with $\hat{s}_z$) components of the wavefunction. This means that we must decompose the wavefunction for a single-particle orbital k in terms of space $\theta(l, m_l)$ and spin $\sigma(m_s)$. With quantum numbers (l, j, m), this proceeds as follows

$$|l, j, m_j\rangle = \sum_{m_l, m_s} \left\langle l, m_l, s, m_s \mid j, m_j \right\rangle |\theta(l, m_l), \sigma(s, m_s)\rangle \tag{5.3}$$

We know that the spin and orbital angular momenta can be aligned ($j = l + 1/2$) or anti-aligned ($j = l - 1/2$). For the case where $j = l + 1/2$ and $m_j = j$, the sum in Eq. 5.3 has only 1 contributing Clebsch-Gordon coefficient corresponding to $m_l = l$ and $m_s = 1/2$, which is evaluated as 1, and we have:

$$\left| l, j = l + \frac{1}{2}, m_j = j \right\rangle = \left| \theta(l, m_l = l), \sigma\left(m_s = \frac{1}{2}\right) \right\rangle \tag{5.4}$$

For the case where $j = l - 1/2$ and $m_j = j$, the sum in Eq. 5.3 involves spin-orbit projection pairings of $(m_l = l - 1, s = 1/2)$ and $(m_l = l, s = -1/2)$, and their corresponding Clebsch-Gordon coefficients yield:

$$\left| l, j = l - \frac{1}{2}, m_j = j \right\rangle = \frac{1}{\sqrt{2l+1}} \left| \theta(l, l-1), \sigma\left(\frac{1}{2}\right) \right\rangle - \sqrt{\frac{2l}{2l+1}} \left| \theta(l, l), \sigma\left(-\frac{1}{2}\right) \right\rangle \tag{5.5}$$

Applying both Eqs. 5.4 and 5.5 to Eq. 5.2 we calculate the eigenvalue of the magnetic dipole moment:

$$\frac{\mu_z}{\mu_N} = \underbrace{l g^\ell + \frac{g^s}{2}}_{j=l+\frac{1}{2}} \qquad \text{and} \qquad \underbrace{\frac{(2l-1)(l+1)}{2l+1} g^\ell - \frac{2l-1}{4l+2} g^s}_{j=l-\frac{1}{2}} \tag{5.6}$$

Taking into account the coupled single-particle angular momentum $j = \ell \pm 1/2$, these results can be rewritten in a compact form as:

$$\frac{\mu}{\mu_N} = j \left[g^\ell \pm \frac{g^s - g^\ell}{2\ell + 1} \right] \tag{5.7}$$

where the term with $(+)$ corresponds to $j = l - \frac{1}{2}$, the term with $(-)$ corresponds to $j = l + \frac{1}{2}$, and the term in brackets is called the g-factor:

$$g = \left[g^\ell \pm \frac{g^s - g^\ell}{2\ell + 1} \right] = \frac{\mu}{\mu_N j} \tag{5.8}$$

Following the application of the projection theorem starting at Eq. 18.26 in [5], one can find that n nucleons, all in the same single-particle orbital $j = \ell \pm s$ - each individually having g-factors $g(j)$ - coupled up to a total angular momentum J will have a g-factor of (Eq. 18.32 of [5]):

$$g(j^n, J) = g(j) \tag{5.9}$$

If the configuration states that describe the wavefunctions for the ground states of each of these nuclei involved couplings between different single-particle orbits, then one would not expect the g-factors for each of these orbits to be identical for a given nuclear spin J. The physical intuition behind this result can be explained in terms of the pairing component of the strong interaction. When an even number of fermions are in the same single-particle orbit, the pairing interaction between them couples fermions with opposite angular momentum projection m_j so that together

Table 5.1 Experimental dipole moment values (μ_N) and the corresponding calculations from the new p35-i3 and older jj44a and n50j Hamiltonians for A = 79 - 89.

Nucleus	J^π	Exp	p35-i3	jj44a	n50j
^{79}Cu	$5/2^-$		1.329	1.329	1.329
^{80}Zn	2^+		1.317	1.256	1.236
^{81}Ga	$5/2^-$	1.747(5)[29]	1.328	1.382	1.330
^{82}Ge	2^+		1.501	1.818	1.304
^{83}As	$5/2^-$		1.361	1.487	1.313
^{84}Se	2^+		2.395	2.118	1.792
^{85}Br	$3/2^-$		3.295	2.681	3.136
^{86}Kr	2^+	2.2(4)[30]	2.6	2.2	2.2
^{86}Kr	4^+	4.1(6)[30]	4.1	5.6	3.6
^{87}Rb	$3/2^-$	2.75131(12)[31]	2.86469	2.77036	3.10328
^{88}Sr	2^+	2.44(22)[32]	2.17	2.21	2.43
^{89}Y	$1/2^-$	-0.1374154(3)[33]	-0.17814	-0.20371	-0.17663
^{89}Y	$9/2^+$	6.37(4)[34]	6.27	6.23	6.19

they do not contribute any angular momentum to the nucleus as a whole. This notion of fermions coupling to each other in the same orbit is expressed in the language of seniority, and in the state consisting of two fermions coupling to $J = 0$ we refer to this as a seniority $\nu = 0$. As discussed in the first chapter, one of the key components of the strong interaction is the pairing interaction. The concept of seniority was introduced by Racah [35] in the context of atomic physics to distinguish states of many-body electronic systems with the same orbital, spin, and total angular momentum. For $[nlj]^n$ configurations, seniority ν is a good quantum number. In the particular case of the odd-even nuclei shown in Figure 5.7, this means that the magnetic moment of the nucleus as a whole comes from the nucleon that is unpaired; as such, these states are considered to have a seniority of $\nu = 1$. In this sense, the uniformity of the magnetic moments for the odd n nuclei in Figure 5.7 with the same J-values is a manifestation of the dominant $[nlj]^n$ configurations present in their respective wavefunctions. In Figure 5.7, we see that for the experimental data in the region

with $A \geq 91$, there is a small systematic deviation between experiment and theory that will be addressed towards the end of this section.

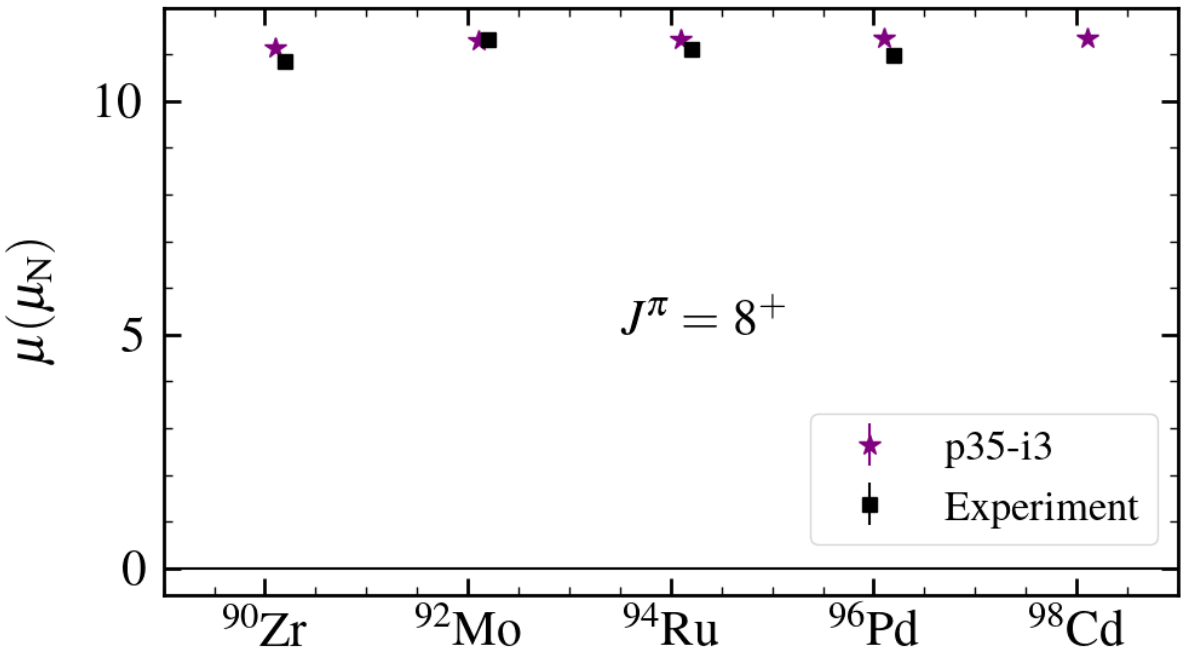

Figure 5.8 A comparison between the experiment and theory for the magnetic dipole moments of 8^+ isomeric states in even-even nuclei from ^{90}Zr to ^{98}Cd.

For the 8^+ isomeric states in Figure 5.8, we can see a similar level of uniformity in the magnetic moments for these even-even nuclei. The reason for the uniformity of magnetic moments in these nuclei is similar to the low-lying states in the odd-even nuclei: The wavefunctions describing the states of these even n nuclei are heavily dominated by configurations of the form $[0g_{9/2}]^n$, and pairing restricts the contributions to the nuclear magnetic moment to come from the two unpaired nucleons. The difference between the 8^+ isomers and those discussed previously for odd-even nuclei is that these states involve breaking a pair of protons in this orbit, which means that these states are seniority $\nu = 2$ excitations in the $0g_{9/2}$ orbit. It should be noted that the 8^+ isomeric state of ^{90}Zr is distinct from the even-even nuclei with $A \geq 92$, because the higher mass nuclei are effectively seniority excitations on top of a nearly filled fp orbital space, or a ^{90}Zr core; The excitation in ^{90}Zr is effectively a seniority $\nu = 2$ excitation on top of a partially filled fp shell (a ^{88}Sr core).

Applying Equation 5.9 to the even-even nuclei, we know that the g-factors for the 8^+ states in Figure 5.8 are the same as the g-factors for the single-particle configurations involved in the $9/2^+$ states for the odd-even nuclei in the same single-particle orbits. It follows from Equation 5.7 that the ratio of the magnetic moments for the 8^+ states to the $9/2^+$ states is as follows:

$$\frac{\mu_{9/2^+}}{9/2 * \mu_N} = \frac{\mu_{8^+}}{8 * \mu_N} \quad \longrightarrow \quad \frac{\mu_{8^+}}{\mu_{9/2^+}} \approx 1.778$$

Indeed, if we take the ratio of the experimental magnetic moment for the first 8^+ state in ^{92}Mo to the first $9/2^+$ state in ^{91}Nb, we obtain $\mu_{8^+}/\mu_{9/2^+} \approx 1.733$. There is only a 2.5% difference between the experiment and the approximation of pure configuration states of the form $\left[0g_{9/2}\right]^n$ for these nuclei. Our wavefunctions for these states involve configuration mixing, but even with this they predict a ratio $\mu_{8^+}/\mu_{9/2^+} \approx 1.779$, that is only a 0.1% difference from the approximation of pure configuration states.

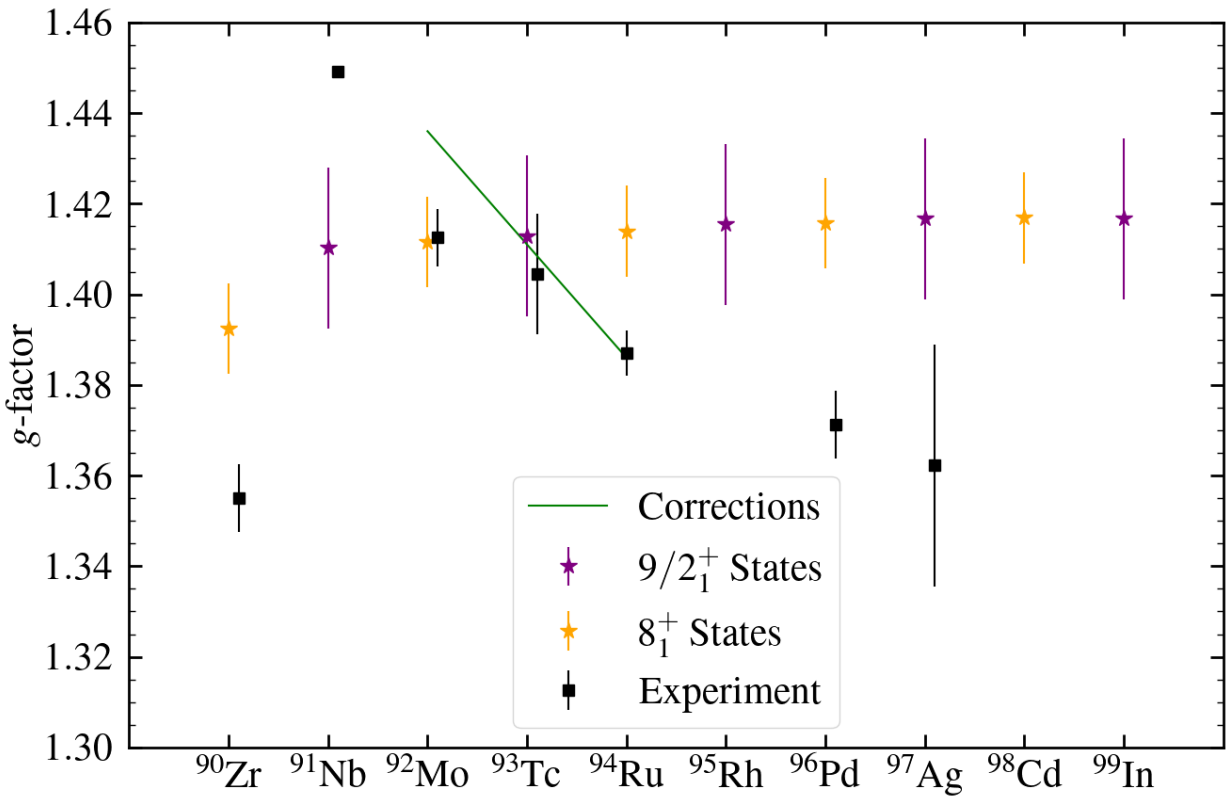

Figure 5.9 Comparisons of g-factors for all nuclei with $A \geq 90$. Corrections in green come from configurations outside of the model space used in [36].

As mentioned above, there is a systematic discrepancy between the experimental dipole moments and the calculations from theory for the odd-even nuclei with $A \geq 91$ in Figure 5.7. Additionally, the same discrepancy is observed for the $A \geq 90$ even-even nuclei in Figure 5.8. On the scale of these magnetic moments, this discrepancy is small, but we can consider a zoomed in look at the discrepancy by considering the plot of g-factors in Figure 5.9. This plot contains a number of features that are worth considering. First, we see a uniformity in the predicted g-factors for all nuclei with $A \geq 91$, which agrees well with the assumptions in Eq. 5.9. Second, we can see a systematic deviation between the experimental and theoretical values. The origins of this discrepancy are the core-polarization effects that go beyond effects captured by our effective g-factors. These core-polarization effects are contributions to a given electromagnetic observable from configurations that are not included in a truncated model space. The curve shown in green are the results obtained for ^{92}Mo and ^{94}Ru when Z-dependent corrections are explicitly added arising from configurations outside of the model space [36]. The core polarization diagrams used in [36] connect the lower $0g_{9/2}$ and upper $0g_{7/2}$ orbits.

The p35-i3 Hamiltonian wavefunctions predict that the low-lying spectra of the nuclei in the $\pi j4$ model space are dominated by k^n configurations, and the consequences can be seen visually in the structure of the magnetic moments. We observe that, in general, there are multiple k^n configurations (corresponding to multiple values of n) involved in each nuclear state, as previously discussed with the example of ^{89}Y.

5.2.3 Electric Quadrupole Moments

The electric quadrupole moment is defined as the diagonal matrix element of the $O(E2)$ operator for states with $M = J$ as shown in Eq. 2.29. The electric quadrupole moment is a measure of both the spatial charge distribution (deformation) of a nucleus in a state and a measure of the collectivity of a given state, which is the large scale correlated motion of nucleons as opposed to independent motion. Looking back to Eq. 2.17 we can see that this operator depends on the effective charge parameter, which we apply to renormalize our $E2$ calculations. We apply the minimal assumption of a single effective charge parameter e_p to all calculations, resulting in an $O(E2)$ operator in the

Table 5.2 Experimental dipole moment values (μ_N) and the corresponding calculations from the new p35-i3 and older jj44a and n50j Hamiltonians for A = 90 - 99.

Nucleus	J^π	Exp	p35-i3	jj44a	n50j
^{90}Zr	2^+	2.5(4)[37]	2.6	2.7	2.6
^{90}Zr	5^-	6.25(13)[38]	6.04	6.02	5.59
^{90}Zr	3^-	3.0(2)[37]	3.6	3.3	3.4
^{90}Zr	8^+	10.84(6)[39]	11.14	11.02	10.85
^{91}Nb	$9/2^+$	6.521(2)[40]	6.346	6.346	6.346
^{91}Nb	$1/2^-$	-0.101(2)[40]	-0.192	-0.205	-0.201
^{91}Nb	$(13/2)^-$	8.14(13)[41]	8.16	8.11	7.64
^{91}Nb	$(17/2)^-$	10.82(14)[42]	10.92	10.89	10.42
^{91}Nb	$(21/2)^-$	12.4(19)[43]	14.5	14.3	14.0
^{92}Mo	2^+	2.3(3)[44]	2.8	2.8	2.7
^{92}Mo	8^+	11.30(5)[42]	11.29	11.29	11.29
^{92}Mo	11^-	13.9(3)[42]	14.4	14.9	13.9
^{93}Tc	$9/2^+$	6.32(6)[45]	6.36	6.36	6.36
^{93}Tc	$(17/2)^-$	10.46(5)[42]	10.75	10.46	10.46
^{94}Ru	2^+		2.790	2.812	2.802
^{94}Ru	6^+	8.124(48)[42]	8.477	8.477	8.487
^{94}Ru	8^+	11.096(40)[42]	11.311	11.311	11.321
^{95}Rh	$9/2^+$		6.369	6.364	6.369
^{96}Pd	(8^+)	10.97(6)[46]	11.33	11.33	11.33
^{97}Ag	$(9/2)^+$	6.13(12)[47]	6.38	6.38	6.38
^{98}Cd	2^+		2.799	2.823	2.847
^{99}In	$9/2^+$		6.375	6.375	6.375

form of the rank-2 tensor:

$$\hat{T}^{\lambda=2}_{\mu=0} = \hat{Q} = \sqrt{\frac{16\pi}{5}} e_p r^2 Y^2(\theta, \phi) e \tag{5.10}$$

As shown in Eq. 2.20, our wavefunctions can be separated into radial and angular components, and the evaluation of radial matrix elements is performed using Skrme energy density functionals (EDF's) [11] for our radial wavefunctions. The value of our effective charge is fitted to reproduce well-determined quadrupole moments, and the results are shown in Figures 5.10 and 5.11. An effective charge is an essential parameter for calculations in a truncated model space because the wavefunctions used to represent physical states in each nucleus do not include orbital configurations which would otherwise be connected by the $O(E2)$ operator; for example, configurations from the $0f_{7/2}$ orbit below our model space and the $\{0g_{7/2}, 1d_{5/2}\}$ orbits above it would all be connected by the $O(E2)$ operator to configurations in the $\pi j4$ model space, and would contribute to the calculated value of each electric quadrupole moment were they included. In addition, there are $2\hbar\omega$ excitations (with respect to the Harmonic Oscillator basis) that are also connected by the $O(E2)$ operator, for example, $0g_{9/2} \rightarrow \{1g_{9/2}, 2d_{5/2}\}$ excitations. The "free proton" model assumes that the effective charge of the proton is $e_p = 1$; with our truncated wavefunctions, this assumption results in a large systematic discrepancy between experiment and theory, as shown in Figure 5.10.

Since the quadrupole moments scale linearly in the effective charge (as do the $M = \sqrt{B(E2)}$ values), the effective charge in the $O(E2)$ calculations of quadrupole moments can be fit to well-determined experimental quadrupole moments. The best fit was a value of $e_p = 1.8$, and the results are shown in Figure 5.11. This value is used in all the calculations presented for electric quadrupole moments and $B(E2)$ transition strengths in this work.

Figure 5.12 shows a collection of electric quadrupole moments for the low-lying states of odd-even nuclei in our model space. As in Figure 5.7, all values shown correspond to ground states with the exception of the $9/2^+$ state in ^{89}Y. Moving from left to right across the figure, the plot is divided into segments of a given J^π, in the same form as the plots of magnetic dipole moments. For a given J^π value we see that there is a roughly linear increase in the quadrupole moment as we increase the mass number (in this case as we add protons). This can be explained in terms

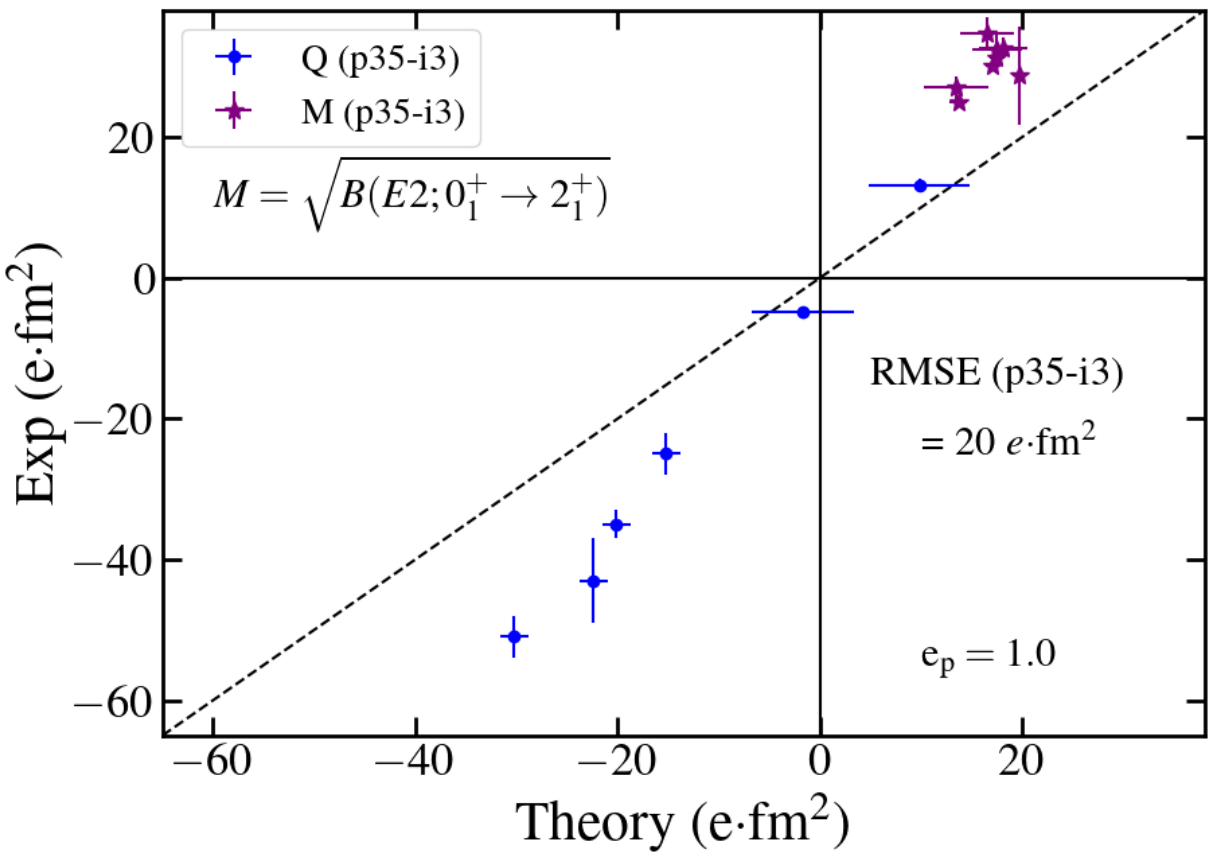

Figure 5.10 Comparison between known experimental quadrupole moments (Q) and $M = \sqrt{B(E2)}$ for first $0^+ \rightarrow 2^+$ transitions in the N=50 region and their corresponding predicted values using the new p35-i3 Hamiltonian with an effective charge $e_p = 1.0$ (free proton). The dashed line indicates a perfect agreement between the two.

of the increasing orbital occupation numbers for the ground states of these nuclei as we increase the number of protons and as a result of the relative dominance of the k^n configurations in the wavefunctions of these nuclei. For example, in our model space ^{79}Cu is a single proton in the $0f_{5/2}$ orbit with a quadrupole moment of:

$$Q\left(k, 0f_{5/2}\right) = -\frac{4}{7}\left\langle 0f_{5/2}\left|r^2\right|0f_{5/2}\right\rangle e_q e \tag{5.11}$$

where the effective charge $e_q = 1.8$, giving the ground state of ^{79}Cu an oblate shape. At the other end of the $J^\pi = 5/2^-$ panel is the ground state of ^{83}As, which is effectively a single hole in the filled $0f_{5/2}$ orbit with a quadrupole moment of:

$$Q\left(k^{-1}, 0f_{5/2}\right) = \frac{4}{7}\left\langle 0f_{5/2}\left|r^2\right|0f_{5/2}\right\rangle e_q e \tag{5.12}$$

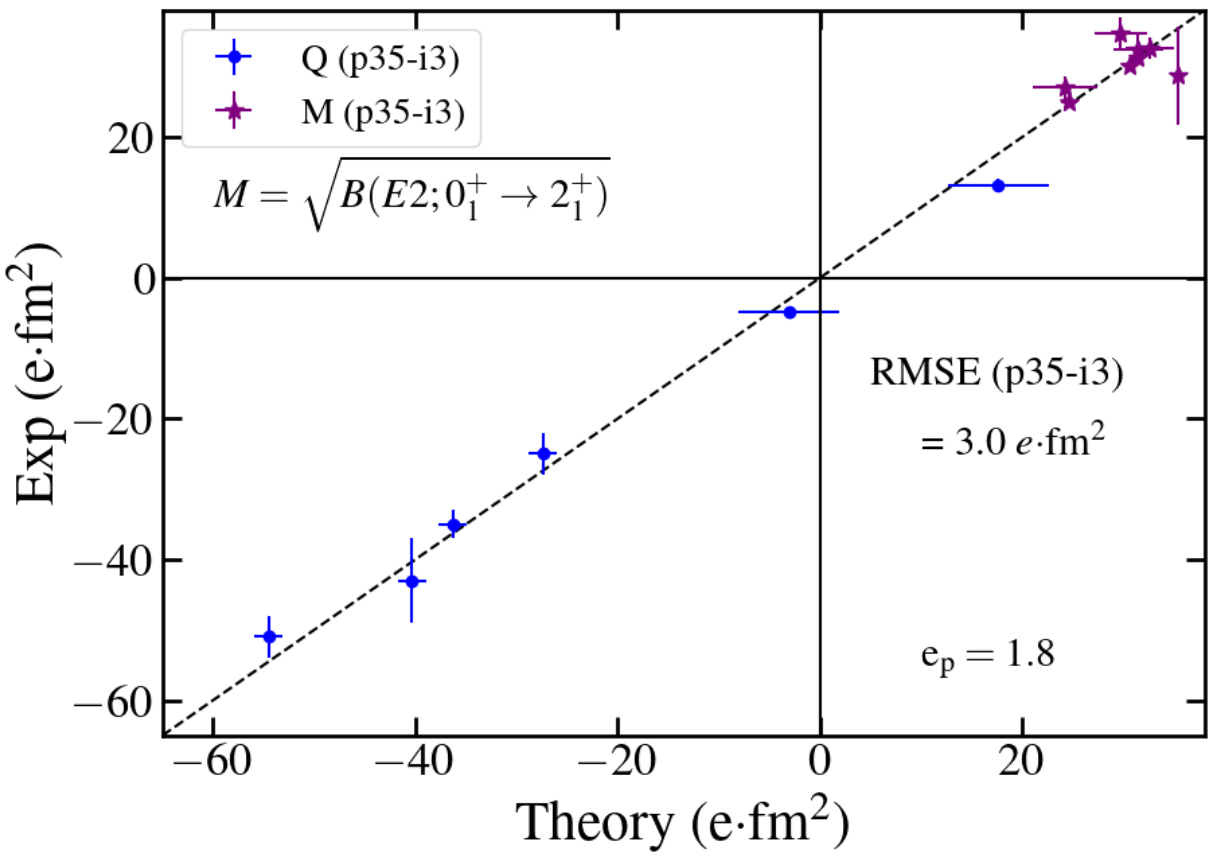

Figure 5.11 Comparison between known experimental quadrupole moments (Q) and $M = \sqrt{B(E2)}$ for first $0^+ \rightarrow 2^+$ transitions in the N=50 region and their corresponding predicted values using the new r35c Hamiltonian with an effective charge $e_p = 1.8$. The dashed line indicates a perfect agreement between the two.

giving the ground state of ^{83}As a prolate shape. As we increase the number of protons occupations in these orbits we move between the extremes of a single particle in a given orbital shell, and a single hole in the filled orbital shell. This pattern repeats for the ground states of nuclei in each of the orbital shells of the model space; for the $1p_{1/2}$ orbit we can see that the quadrupole moment of ^{89}Y is 0 because the quadrupole operator Q is of rank 2, and the triangle condition $\Delta(1/2, \lambda, 1/2)$ forbids the overlap of $J = 1/2$ with operators of this rank.

One can spatially understand the sign and magnitude of the electric quadrupole by expressing the quadrupole operator in cartesian coordinates:

$$\hat{Q} = \left(2\hat{z}^2 - \hat{x}^2 - \hat{y}^2\right) \tag{5.13}$$

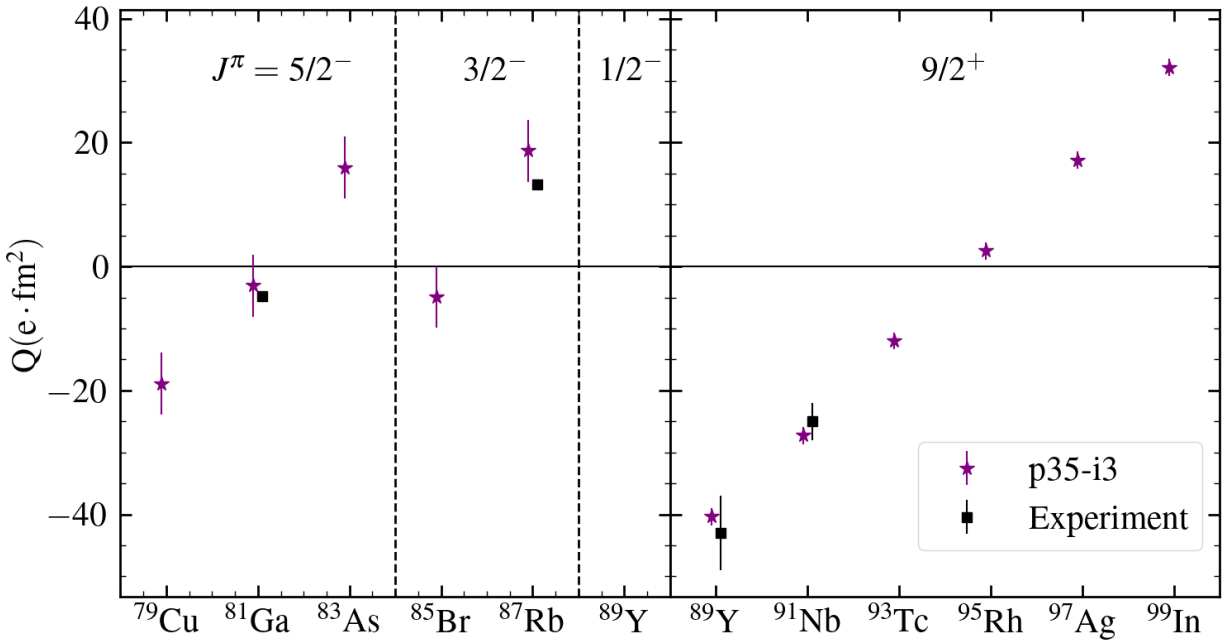

Figure 5.12 A comparison between the experiment and theory for the low-lying electric quadrupole moments in odd-even nuclei from ^{79}Cu to ^{99}In. The vertical separators indicate the nuclear spins of each of these states, and with the exception of the $9/2^+$ state in ^{89}Y, all of the shown values correspond to the ground state.

Here, all orbital projections m_j are to be taken with respect to orbits j about the z-axis, so the motion (wavefunction density) of a single particle with $m = \pm j$ is concentrated within the (x, y)-plane, resulting in a quadrupole moment with $Q < 0$, called oblate. A visual aid to this discussion is provided in Figure 5.13. The negative sign of the oblate electric quadrupole moments arises from the negative signs on the $\hat{x}$ and $\hat{y}$ operators in Eq. 5.13. Particles in a state with $|m| < j$ have some projected component of their j along the z-axis, and if $|m| \lesssim j/2$ this component will result in the motion (wavefunction densities) being dominant along the z-axis. From Eq. 5.13 this indicates a quadrupole moment with $Q > 0$, called prolate. For wavefunction densities that are spherically uniform $Q = 0$.

These intuitions can be used to explain what is happening in both Figures 5.12 and 5.14: As one moves from left to right for a given J^π value, the low-lying states, which are dominated by the k^n configurations, become filled with protons. Because protons are fermions, each addition to an orbit must acquire a unique orbital projection m_j. The case of a single proton (^{79}Cu in the $0f_{5/2}$

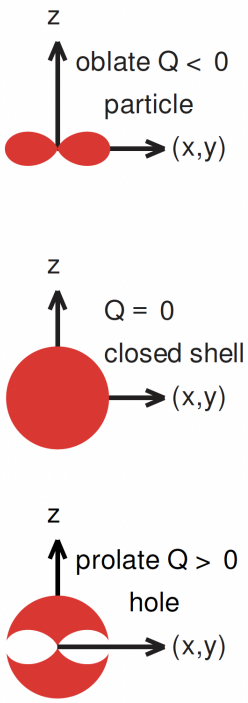

Figure 5.13 The top image shows a density distribution for a single particle with $m = \pm j$, the middle image corresponds to the closed shell, and the bottom image explains a prolate electric quadrupole moment in terms of a hole in a closed shell.

orbit, for example) has that proton that possesses a quantum number $m_j = \pm j$, as in the top image of Figure 5.13. The next added proton (^{80}Zn in this example) will have configurations involving pairs of nucleons with the same $|m_j|$ but opposite sign and will therefore be coupled to $M = 0$ with $Q = 0$. This process continues until the last paired protons in the orbit (in ^{83}As here) have the quantum numbers $m_j = +1/2$ and $m_j = -1/2$ in the xy-plane, with the last unpaired proton having the quantum number $|m| = 5/2$. One can consider this state as a single-hole in the closed $0f_{5/2}$ orbital, as in the bottom image of Figure 5.13. This also explains why nuclei whose wavefunctions are dominated by $k^n = [nlj]^n$ configurations with larger l-values have the largest corresponding ranges and magnitudes of electric quadrupole moments.

Returning to the analysis of my calculations, the right panel of Figure 5.12 shows what can be approximated as seniority $\nu = 1, J^\pi = 9/2^+$ states for the odd-even nuclei, while Figure 5.14 shows what can be approximated as $\nu = 2, J^\pi = 8^+$ isomers in even-even nuclei, because both involve

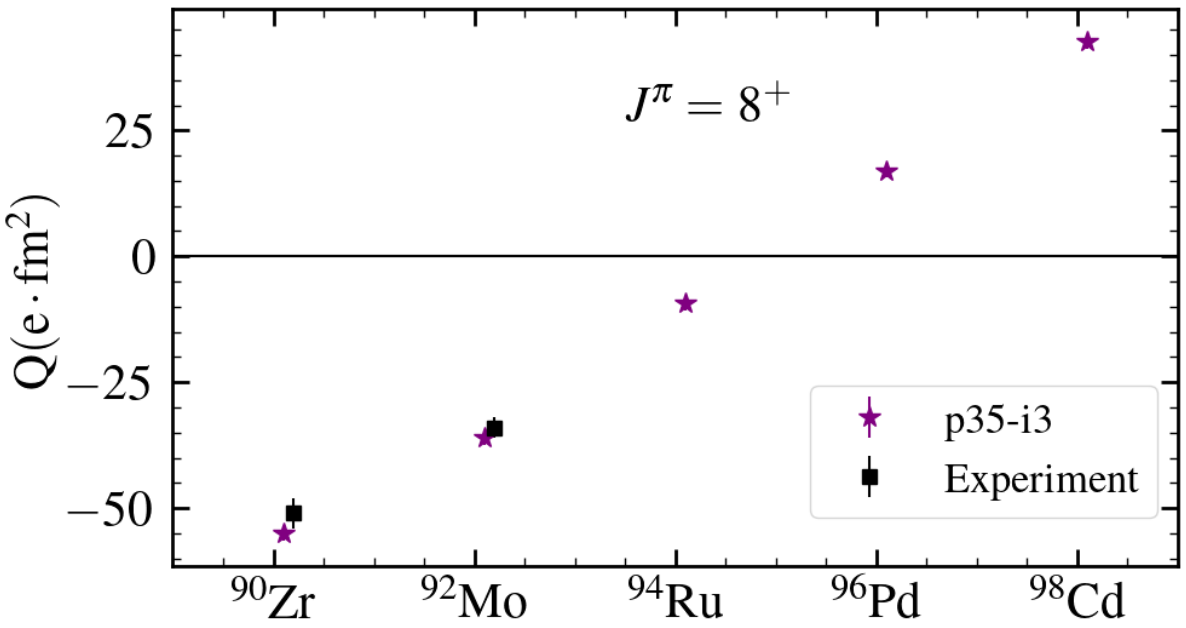

Figure 5.14 A comparison between the experiment and theory for the electric quadrupole moments of 8^+ isomeric states in even-even nuclei from ^{90}Zr to ^{98}Cd.

relatively pure $[0g_{9/2}]^n$ configurations in their wavefunctions. The single-particle wavefunctions for protons involved in these configurations are

$$|k, m\rangle \equiv |k, j = 9/2, m\rangle \tag{5.14}$$

where $k \equiv 0g_{9/2}$. The two-particle wavefunction for the seniority $v = 2$ state is given by

$$\left|k^2, M = 8\right\rangle = |k, m = 9/2\rangle|k, m = 7/2\rangle \tag{5.15}$$

As a reminder, the two particles must have different quantum numbers m because they are fermions and must obey Fermi-Dirac statistics, in particular the Pauli Exclusion Principle. The quadrupole operator is a one-body operator, and under the assumption that the wavefunctions for these states involved relatively pure configurations in a single $k = (n, l, j) = 0g_{9/2}$ orbit on a partially filled fp shell (a ^{88}Sr core with a wavefunction $|C\rangle$), the overlap takes the form:

$$\begin{aligned} Q\left(Ck^n\right) &= \underbrace{\cancel{\left\langle C\left|T^{\lambda=2}_{\mu=0}\right|C\right\rangle}^{0}}_{Q(C)=0} + \left\langle k^n, M\left|T^{\lambda=2}_{\mu=0}\right|k^n, M\right\rangle \\ &= \sum_i^n \left\langle k\text{'}m_i\left|T^{\lambda=2}_{\mu=0}\right|k, m_i\right\rangle = Q\left(k^n\right) \end{aligned} \tag{5.16}$$

where the quadrupole moment of the $J^\pi = 0^+$ state in the partially filled fp shell C is 0, so we will drop the C term in the equations following. For the $J^\pi = 9/2^+$ ground state of ^{91}Nb, the only term in the sum involves the $m = 9/2$ state, while the $J^\pi = 8^+$ excited state of ^{92}Mo involves $m = 9/2$ and $m = 7/2$. Because both of these nuclear states involve overlaps of single-particle states with the same j-value with a spherical tensor, we can make use of the Wigner-Eckart theorem to express overlaps with various m-states in terms of the ground state configuration in ^{91}Nb, denoted $Q(k)$:

$$\begin{aligned} Q(k) &= \left\langle k, m = 9/2 \left| T^2_0 \right| k, m = 9/2 \right\rangle \\ &= \langle k, m = 9/2, \lambda = 2, \mu = 0 | k, m = 9/2 \rangle \left\langle k \left\| T^2 \right\| k \right\rangle \end{aligned} \tag{5.17}$$

With the evaluation of the quadrupole moment for ^{91}Nb and the corresponding Clebsch-Gordon coefficient, one can take their ratio to obtain the reduced matrix element denoted by the overlap with double bars. From this the single-particle quadrupole moment for the $m = 7/2$ state in the $J^\pi = 8^+$ seniority isomer of ^{92}Mo is the quadrupole moment of the $m = 9/2$ state proportional to a ratio of their Clebsch-Gordon coefficients:

$$\left\langle k, m = 7/2 \left| T^2_0 \right| k, m = 7/2 \right\rangle = \frac{\langle k, m = 7/2, 2, 0 | k, m = 7/2 \rangle}{\langle k, m = 9/2, 2, 0 | k, m = 9/2 \rangle} Q(k) = \frac{Q(k)}{3} \tag{5.18}$$

With this we can express the quadrupole moment of the $J^\pi = 8^+$ seniority isomer of ^{92}Mo as:

$$Q(k^2) = Q(k) + \frac{Q(k)}{3} = \frac{4}{3} Q(k) \tag{5.19}$$

For comparison, the ratio of the experimental quadrupole moment of ^{92}Mo to that of ^{91}Nb is 1.322, which agrees with this calculation to within 1%. The wavefunctions given by Eqs. 5.14 and 5.15 correspond to the approximation that these states are pure k^n configurations; The p35-i3 wavefunctions contain many more configurations for these states, and the ratio of the associated quadrupole moments is 1.320, indicating that the approximation of k^n configurations is accurate for the associated states in these nuclei.

5.2.4 Electromagnetic Transition Strengths

The $B(M1)$ is calculated from the $O(M1)$; unlike the magnetic dipole moment, which is a diagonal matrix element, the $B(M1)$ concerns how the $O(M1)$ operator connects different initial

Table 5.3 Experimental quadrupole moment values (e·fm^2) and the corresponding calculations from the new p35-i3 and older jj44a and n50j interactions for A = 79 - 99.

Nucleus	J^π	Exp (e·fm^2)	p35-i3	jj44a	n50j
^{79}Cu	$5/2^-$		-18.91	-18.91	-18.91
^{80}Zn	2^+		-6.50	-0.56	0.77
^{81}Ga	$5/2^-$	-4.8(8)[29]	-3.09	-1.40	-1.27
^{82}Ge	2^+		-21.36	-10.27	-18.62
^{83}As	$5/2^-$		15.95	4.20	16.95
^{84}Se	2^+		-20.56	-33.80	-19.08
^{85}Br	$3/2^-$		-4.93	20.26	-8.23
^{86}Kr	2^+		-10.39	-15.95	-21.50
^{87}Rb	$3/2^-$	13.2(1)[48]	18.68	17.80	14.15
^{88}Sr	2^+		27.63	27.79	21.53
^{89}Y	$9/2^+$	-43(6)[33]	-40.62	-37.91	-33.67
^{90}Zr	8^+	-51(3)[39]	-55.09	-52.62	-51.59
^{91}Nb	$9/2^+$	-25(3)[40]	-27.24	-27.40	-27.24
^{92}Mo	8^+	-34(2)[49]	-35.96	-36.46	-32.53
^{93}Tc	$9/2^+$		-12.00	-12.10	-9.31
^{94}Ru	8^+		-9.39	-9.73	-7.27
^{95}Rh	$9/2^+$		2.55	2.65	4.07
^{96}Pd	8^+		17.00	16.83	17.42
^{97}Ag	$9/2^+$		17.18	17.23	17.68
^{98}Cd	8^+		42.59	42.59	42.59
^{99}In	$9/2^+$		32.12	32.12	32.12

and final states. The $B(M1)$ is generally sensitive to the single-particle motion of nucleons in the nucleus, which can be seen in the $M1$ transition strengths typically being of order $\sim 0.1 - 1$ Weisskopf Units (W.U.). This is because the $O(M1)$ operator explicitly depends on the intrinsic spin and orbital configurations of the nucleons composing the wavefunctions involved in a transition.

Since the $O(M1)$ operator in Eq. 5.1 has an explicit orbital dependence coming from the $\hat{\ell}$ operator, the only transitions connected by it are between single-particle configurations with the same single-particle orbital quantum number l. This restriction has consequences for the $0f_{5/2}$ and $0g_{9/2}$ orbitals, because there is only one "f" orbit ($l = 3$) and one "g" orbit ($l = 4$) in our model space. This means that the only $M1$ transitions that occur involving these orbitals are to and from the same orbital: $0f_{5/2} \leftrightarrow 0f_{5/2}$ and $0g_{9/2} \leftrightarrow 0g_{9/2}$. On the other hand, the two "p" orbitals ($l = 1$) in the $\pi j4$ model space are connected by the $M1$ operator to each other and themselves: $1p_{3/2} \leftrightarrow 1p_{3/2}$, $1p_{1/2} \leftrightarrow 1p_{1/2}$, and $1p_{3/2} \leftrightarrow 1p_{1/2}$. The nuclei with $A \leq 88$ are most sensitive to the allowed $M1$ transitions mentioned within the fp orbits, while nuclei with $A > 88$ are most sensitive to the $M1$ transitions involving $0g_{9/2} \leftrightarrow 0g_{9/2}$.

A collection of $B(M1)$ values that compare the experiment with various Hamiltonian predictions is displayed in Table 5.4. Here, one can see that there is excellent agreement between predictions from the p35-i3 Hamiltonian and experimental results for the $M1$ transitions that have been measured.

The $B(E2)$ is calculated from the same operator as the quadrupole moment, but it is not the diagonal matrix elements of this operator. Similarly to the relation between the $B(M1)$ and the $O(M1)$ operator, the $B(E2)$ calculation uses the $O(E2)$ operator to connect different initial and final states. The $B(E2)$ is a measure of the collectivity involved in a transition between states. This can be seen in the form of the $O(E2)$ operator given by Eqs. 5.10 and 5.13, which depends explicitly on the spatial distribution of the nuclear wavefunction. As mentioned in Section 5.2.3, we adopt the effective charge of $e_p = 1.8$ for our $O(E2)$ operator.

Figure 5.15 shows the transition strengths from the first 0^+ state to the first 2^+ state in the even-even nuclei of the $\pi j4$ model space. One can see that the p35-i3 Hamiltonian is an improvement

Table 5.4 Experimental values for $M1$ transition strengths and the corresponding calculations from the new p35-i3 and older jj44a and n50j interactions. Experimental data are all from [18]

			$B(M1; J_i^\pi \rightarrow J_f^\pi)(\mu_N^2)$			
Nucleus	J_i^π	J_f^π	Exp	p35-i3	jj44a	n50j
^{86}Kr	2_2^+	2_1^+	0.154(20)	0.165	0.131	0.39
^{87}Rb	$5/2_1^-$	$3/2_1^-$	0.008(5)	0.0094	0.014	742
^{87}Rb	$1/2_1^-$	$3/2_1^-$	0.64(7)	1.04	0.42	960
^{88}Sr	2_2^+	2_1^+	0.074(5)	0.078	0.033	0.014
^{88}Sr	1_1^+	0_1^+	0.33(3)	0.43	0.54	0.26
^{88}Sr	3_1^+	2_1^+	0.008(4)	0.010	0.007	0.00014
^{88}Sr	3_1^+	2_2^+	0.027(5)	0.046	0.027	0.0023
^{88}Sr	2_3^+	2_2^+	0.09(2)	0.041	0.021	0.91
^{88}Sr	3_2^-	3_1^-	0.014(4)	0.016	0.006	0.051

over the older n50j and jj44a Hamiltonians for the $0_1^+ \rightarrow 2_1^+$ transitions. The $B(E2; 0_1^+ \rightarrow 2_1^+)$ values of 2 nuclei within this plot deserve further experimental examination: The value for ^{82}Ge is within the overlap in uncertainty between experiment and theory, but it's value is still significantly higher than what is predicted by any of the available Hamiltonians; The value of the transition in ^{94}Ru simply has a very high degree of uncertainty.

Shifting focus away from these two data, both experiment and theory agree that there are 2 peaks in the collectivity of these types of $E2$ transitions across the even-even nuclei: These peaks are for transitions in ^{84}Se, corresponding to the half-filling of the fp model subspace, and for transitions in ^{94}Ru, corresponding to the half-filling of the $0g_{9/2}$ orbit (along with the complete filling of the fp model subspace). The $B(E2; 0_1^+ \rightarrow 2_1^+)$ in ^{90}Zr is the smallest value and, as mentioned, this nucleus corresponds to the complete filling of the fp shell. The reason why the largest and smallest values of transition collectivity are located where they are has to do with the availability of different configurations in unfilled orbital shells in the 0^+ and 2^+ states of these systems. The low lying spectra of ^{84}Se and ^{86}Kr involve considerable configuration mixing in the fp orbits, which are close to each other in energy, and the low lying spectrum of ^{94}Ru similarly

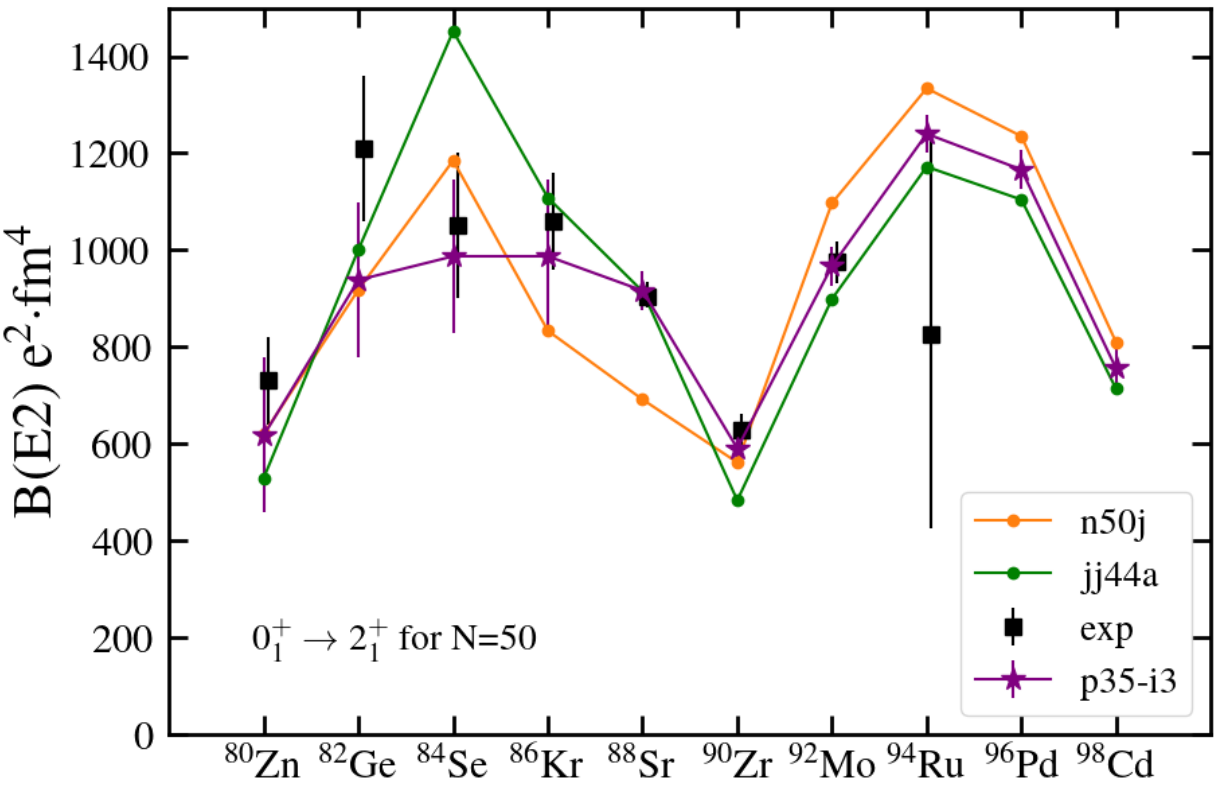

Figure 5.15 The transition strengths from the first 0^+ state to the first 2^+ strength in even-even nuclei for both experiment and a collection of theoretical calculations. In particular, the older jj44a and n50j Hamiltonians are to be compared with the newer p35-i3 Hamiltonian.

involves considerable configuration mixing in the $0g_{9/2}$ orbital. The effect of configuration mixing is to incorporate particle-hole configurations in the wavefunction describing a nuclear state, and such configurations can describe nuclear deformations which, when added together, contribute to a nuclear wavefunction with a large quadrupole moment. These quadrupole moments have a pronounced enhancement of the collective response of protons involved in a transition, especially from a state with high collectivity to a spherically symmetric state like the 0^+. In contrast, the 2^+ excited state of ^{90}Zr involves particle-hole excitations across the $fp - 0g_{9/2}$ shell gap and particle-hole excitations from the $\{0f_{5/2}, 1p_{3/2}\}$ orbitals into the $1p_{1/2}$ orbital. This hinders the amount of configuration mixing involved in the wavefunction, leading to a less pronounced quadrupole moment, resulting in a reduction in the collective response of protons involved in the transition. In this way, ^{90}Zr is similar to doubly magic nuclei.

The $B(E2)$ uncertainties shown in Figure 5.5 are uncertainties with respect to downward transitions $B(E2\downarrow)$; the theoretical $B(E2\uparrow)$ for upward transitions in this section have uncertainties related to downward transitions. From Eq. 2.19 and the fact that

$$\left|\left\langle J_f \,\|B(E2)\|\, J_i\right\rangle\right|^2 = \left|\left\langle J_i \,\|B(E2)\|\, J_f\right\rangle\right|^2 \tag{5.20}$$

we know that the $B(E2)$ up and down between states of given J-value have a simple scaling relation to each other:

$$B(E2; f \rightarrow i) = \left(\frac{2J_i + 1}{2J_f + 1}\right) B(E2; i \rightarrow f) \tag{5.21}$$

This means that the uncertainties between $B(E2\downarrow)$ and $B(E2\uparrow)$ also have the same simple scaling relation from the propagation of uncertainty:

$$\sigma(E2; f \rightarrow i) = \left(\frac{2J_i + 1}{2J_f + 1}\right) \sigma(E2; i \rightarrow f) \tag{5.22}$$

To be explicit, given the uncertainty in the downward transition $B(E2\downarrow; 2_1^+ \rightarrow 0_1^+)$ from Figure 5.5, the uncertainty in the corresponding upward transition $B(E2\uparrow; 0_1^+ \rightarrow 2_1^+)$ is given by:

$$\begin{aligned}\sigma(E2\uparrow; 0_1^+ \rightarrow 2_1^+) &= 5 * \sigma(E2\downarrow; 2_1^+ \rightarrow 0_1^+) \\ &\approx \underline{155\ \mathrm{e}^2 \cdot \mathrm{fm}^4}(A < 88) \quad \text{or} \quad \underline{40\ \mathrm{e}^2 \cdot \mathrm{fm}^4}(A \geq 88)\end{aligned} \tag{5.23}$$

Figure 5.16 shows the values of $B(E2)$ in downward transitions from 8_1^+ to 6_1^+ for even-even nuclei with $Z \geq 40$. The p35-i3 Hamiltonian performs comparably well with the n50j and jj44a Hamiltonians for the $8_1^+ \rightarrow 6_1^+$ transitions compared to the experimental data in this region of nuclei. There appears to be a large disparity between the various model predictions for the $8_1^+ \rightarrow 6_1^+$ transition in ^{90}Zr, and jj44a agrees closely with the experimental results. The spread in these calculations at ^{90}Zr is due to differences in the orbital occupations of the fp and $0g_{9/2}$ orbits between these Hamiltonians, differences in the TBME connecting these orbits, and due to the increased configuration mixing between these orbits for ^{90}Zr. Table 5.5 details a larger comparison of $E2$ transitions comparing theory and experiment. For states with good seniority, the $B(E2)$ between the j^n configurations with ν=2 is given by [50]:

$$B\left(E2; j^n, J_i \rightarrow J_f\right) = \left[\frac{2j + 1 - 2n}{2j + 1 - 2\nu}\right]^2 B\left(E2; j^2, J_i \rightarrow J_f\right) \tag{5.24}$$

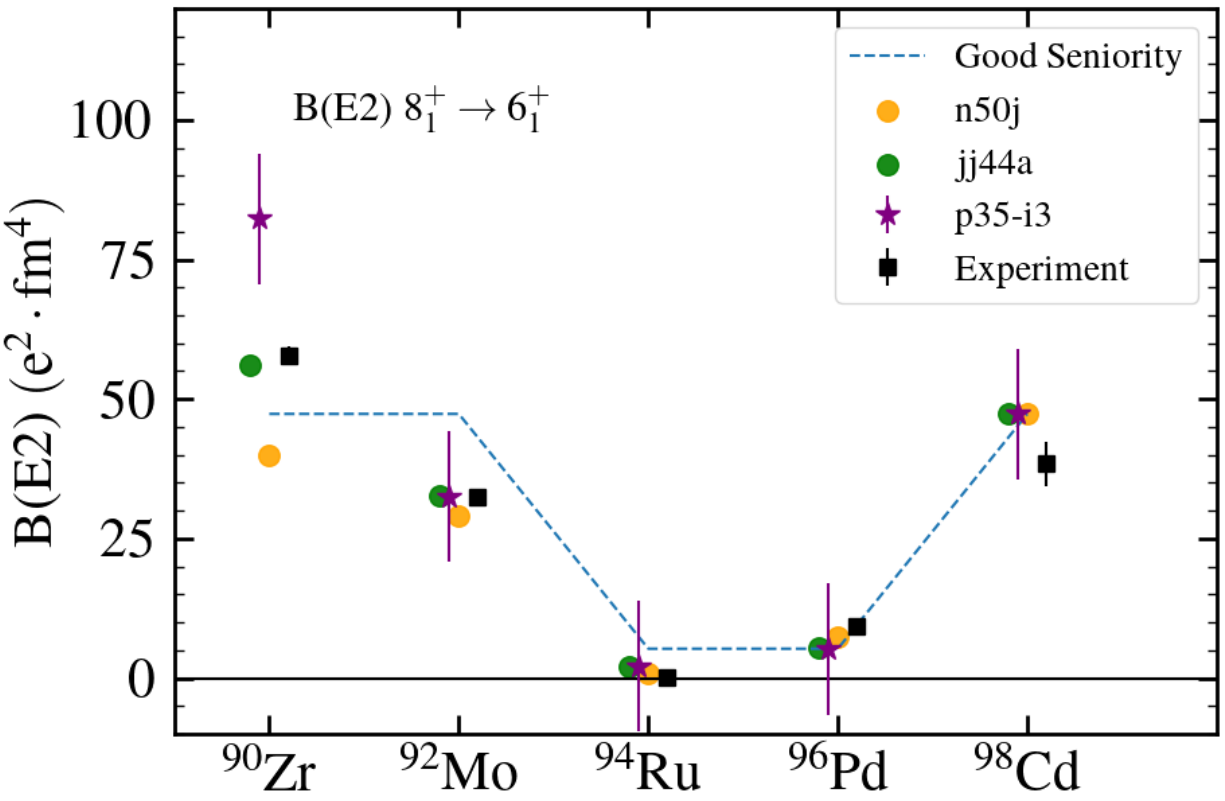

Figure 5.16 The transition strengths from the first 8^+ state to the first 6^+ strength in even-even nuclei for both experiment and a collection of theoretical calculations. In particular, the older jj44a and n50j Hamiltonians are to be compared with the newer p35-i3 Hamiltonian. The blue dashed curve is calculated using Eq. 5.24 given by [50].

In addition to the Hamiltonian predictions shown in Figure 5.16, there is a blue dashed curve showing the results calculated from Equation 5.24. Assuming $\left[0g_{9/2}\right]^2$ configurations, the value of $B(E2; 8_1^+ \rightarrow 6_1^+)$ in this dashed curve is taken from the transition between states in ^{98}Cd using the p35-i3 wavefunctions as a reference nucleus. ^{98}Cd was selected as the reference nucleus because the 8_1^+ state in this nucleus is a pure $[0g_{9/2}]^{-2}$ configuration in ^{100}Sn. The curve can be seen to level off at ^{90}Zr, this is because the 8_1^+ state in ^{90}Zr is also a $\left[0g_{9/2}\right]^2$ configuration; As mentioned in Sect. 5.2.2 the ^{90}Zr k^n configurations are different from the k^n configurations in $A \geq 92$ even-even nuclei, because this configuration state involves a ^{88}Sr core. The 8_1^+ states for even-even nuclei with $A \geq 92$ all involve a broken pair of protons on top of a dominantly filled fp model space, while the broken pair in ^{90}Zr is coupled to the dominantly filled $\left\{0f_{5/2}, 1p_{3/2}\right\}$ orbitals. Both the data and model predictions agree well with the approximation that these wavefunctions are well described

as $\left[0g_{9/2}\right]^n$ configurations with good seniority and even n, in particular with seniority $\nu = 2$.

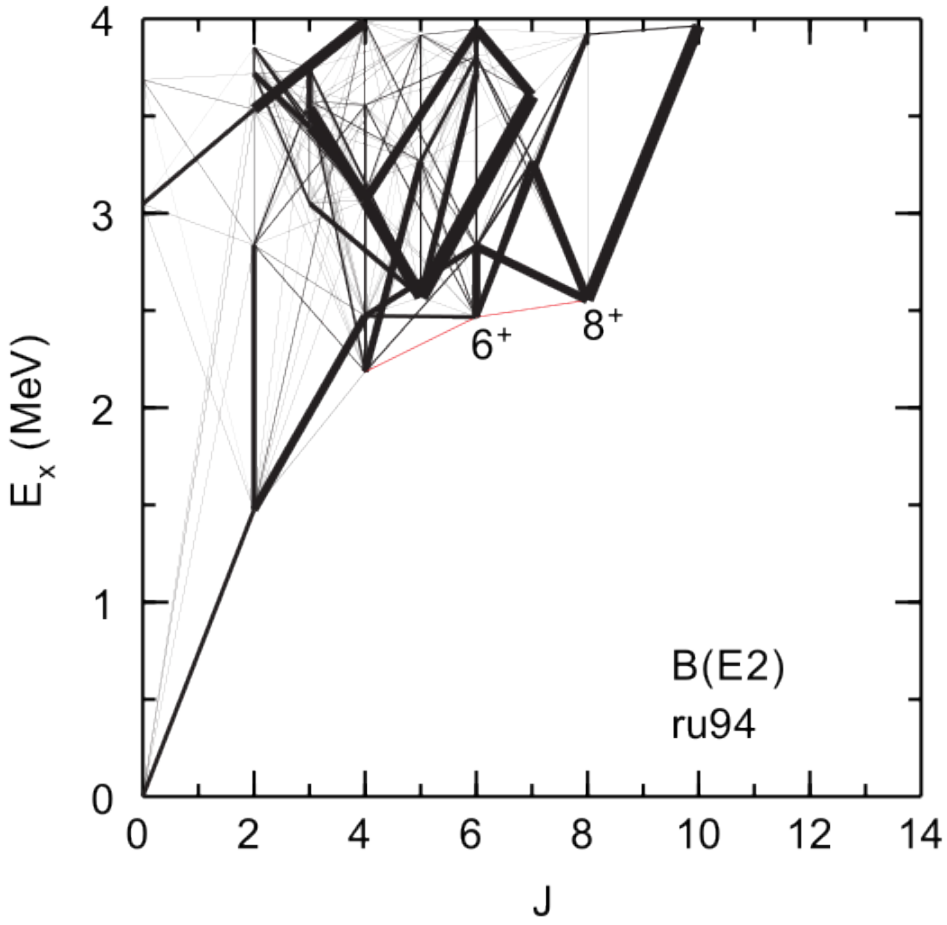

Figure 5.17 A collection of all $E2$ transitions between states in the ^{94}Ru nucleus obtained from the p35-i3 interaction. The width of the black lines indicates the magnitude of the $B(E2)$ corresponding to that transition. The thin red lines correspond to weak transitions for which there is mixing with a nearby transition between states with the same J, but with a much larger transition strength.

Looking at Table 5.5, an interesting set of discrepancies between experiment and theory can be seen for a collection of transitions. First, the $B(E2; 8_1^+ \rightarrow 6_1^+)$ values for ^{94}Ru are predicted to be substantially stronger for the three Hamiltonians than the experimental value. Looking at the $B(E2; 21/2_1^+ \rightarrow 17/2^+)$ transitions in ^{95}Rh, we see that across the three Hamiltonians shown, the $21/2_1^+ \rightarrow 17/2_1^+$ predictions are substantially weaker than the experimental results, while the $21/2_1^+ \rightarrow 17/2_2^+$ transition is predicted to be nearly double the experimental results.

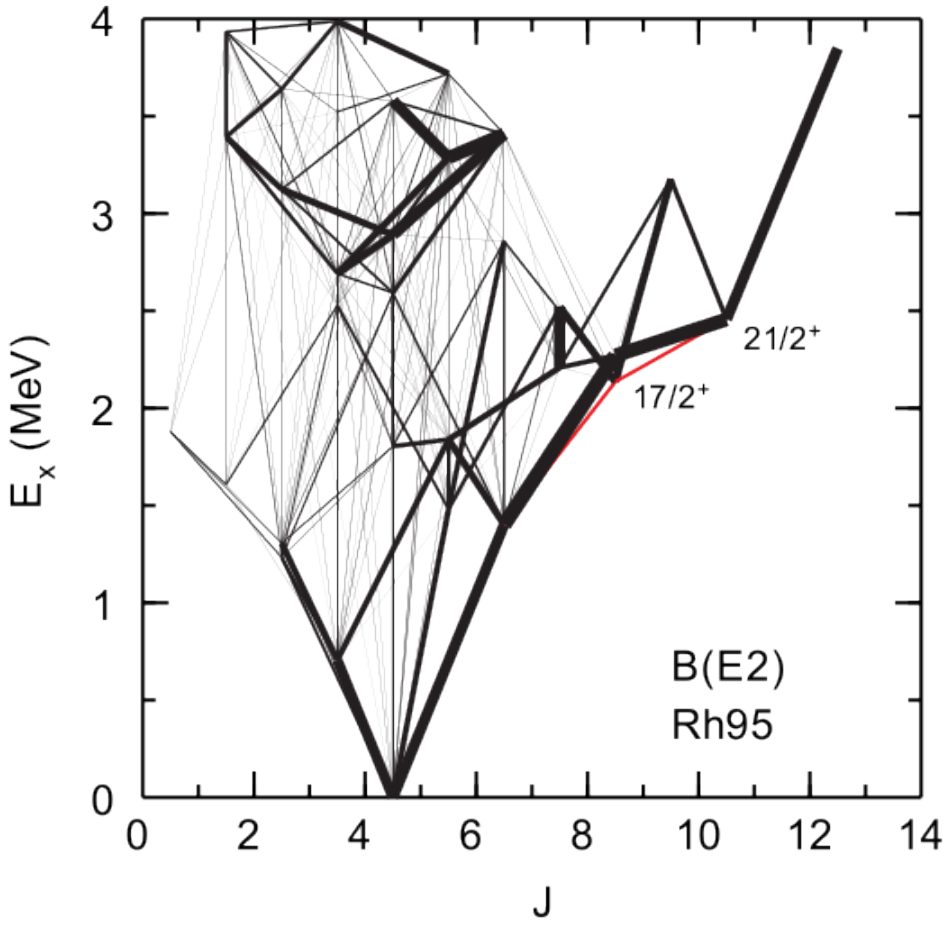

Figure 5.18 A collection of all $E2$ transitions between states in the ^{95}Rh nucleus obtained from the p35-i3 interaction. The width of the black lines indicates the magnitude of the $B(E2)$ corresponding to that transition. The thin red lines correspond to weak transitions for which there is mixing with a nearby transition between states with the same J, but with a much larger transition strength.

We can trace the origin of these discrepancies to mixing with nearby levels with the same spin that have very large $B(E2)$. In ^{94}Ru there are two 6^+ states within 250 keV of the 8^+ that feeds into them. Looking at Figure 5.17, we see that the $B(E2; 8^+_1 \rightarrow 6^+_1)$ shown in red is near the much stronger upward transition strength $B(E2; 8^+_1 \rightarrow 6^+_2)$ shown in black immediately above this red line. In ^{95}Rh the two $17/2^+$ states are only separated by 120 keV, which is a smaller separation than the theoretical uncertainty of our Hamiltonian. In Figure 5.18 we see that the $B(E2; 21^+_1 \rightarrow 17^+_1)$ shown in red is near the much stronger transition to the second $17/2^+$ state, with a transition strength

$B(E2; 21_1^+ \rightarrow 17_2^+)$ shown in black immediately above the red line. The $B(E2; 21_1^+ \rightarrow 17_1^+)$ is smaller because it corresponds to a seniority $\nu = 2 \rightarrow \nu = 2$ transition as in Equation 5.24, while the $B(E2; 21_1^+ \rightarrow 17_2^+)$ involves a stronger collective response with a seniority $\nu = 2 \rightarrow \nu = 4$ transition. With this perspective, the discrepancies between experiment and theory can be resolved by perturbative mixing in our Hamiltonian of the 6^+ states in ^{94}Ru or the $17/2^+$ states in ^{95}Rh. A first-order perturbation of approximately 26 keV could mix these states in their respective nuclei to reproduce the corresponding experimental results; in principle, such perturbations could arise from 2-, 3-, and many-body forces not included explicitly in our Hamiltonian

Table 5.5 Experimental values for $E2$ transitions and the corresponding calculations from the new p35-i3 and older jj44a and n50j interactions with $e_p = 1.8$.

			$B(E2; J_i^\pi \rightarrow J_f^\pi)(e^2\ \mathrm{fm}^4)$			
Nucleus	J_i^π	J_f^π	Exp	p35-i3	jj44a	n50j
^{80}Zn	0_1^+	2_1^+	730(90)[51]	585	529	518
^{82}Ge	0_1^+	2_1^+	1210(150)[52]	883	1001	742
^{84}Se	0_1^+	2_1^+	1050(150)[52]	986	1452	960
^{86}Kr	0_1^+	2_1^+	1060(100)[53]	1058	1108	675
^{88}Sr	0_1^+	2_1^+	$903^{(+32)}_{(-23)}$[54]	933	915	560
^{90}Zr	0_1^+	2_1^+	627(34)[54]	604	483	454
^{92}Mo	0_1^+	2_1^+	975(43)[54]	987	899	889
^{94}Ru	0_1^+	2_1^+	825(400)[55]	1250	1172	919
^{96}Pd	0_1^+	2_1^+		1162	1104	1000
^{98}Cd	0_1^+	2_1^+		749	713	655
^{92}Mo	4_1^+	2_1^+	$132^{(+7)}_{(-6)}$[56]	135	126	87
^{92}Mo	6_1^+	4_1^+	81(2)[56]	81	85	72
^{92}Mo	8_1^+	6_1^+	28.6(3)[56]	32.0	32.7	28.9
^{93}Tc	$17/2_1^+$	$13/2_1^+$	88(18)[56]	117	117	96
^{93}Tc	$21/2_1^+$	$17/2_1^+$	73(5)[56]	61	66	60
^{94}Ru	4_1^+	2_1^+	38(3), 103(24)[56]	12.0	7.2	1.7
^{94}Ru	6_1^+	4_1^+	3.0(2)[56]	5.0	6.3	4.8
^{94}Ru	8_1^+	6_1^+	0.09(1)[56]	1.42	1.98	0.73
^{95}Rh	$21/2_1^+$	$17/2_1^+$	24(2)[56]	4.992	0.004	0.23
^{95}Rh	$21/2_1^+$	$17/2_2^+$	113(13)[56]	185	200	194
^{96}Pd	(6_1^+)	(4_1^+)	20.4(2.9)[57]	16.1	15.5	16.8
^{96}Pd	(8_1^+)	(6_1^+)	9.4(1.0)[57]	6.0	5.4	7.4
^{98}Cd	(4_1^+)	(2_1^+)	98(50)[58]	165	169	169
^{98}Cd	(6_1^+)	(4_1^+)	110(5)[58]	117	118	118
^{98}Cd	(8_1^+)	(6_1^+)	39(4)[58]	47	47	47

CHAPTER 6

CONCLUSION

Within the framework of the nuclear Shell Model, we have constructed a new effective interaction in the form of a Hamiltonian called p35-i3 [1]. In the process of producing this Hamiltonian, I have implemented the Monte Carlo Cross Validation method (MCCV) as a means of both diagnosing the bias-variance trade-off of the fit, as well as a means of demonstrating which ab initio interactions extrapolate well to nuclei in the $\pi j4$ model space. This was done by examining the RMSD of the parameters between ab initio values and fitted values as an increasing number of linear combinations of parameters are fitted to the data. The resulting set of wavefunctions for this Hamiltonian reproduce the experimentally known energy-spin spectra of the $\pi j4$ nuclei to within an RMSD of 150 keV, down from the 1 MeV RMSD between experiment and theory arising from the wavefunctions from ab initio Hamiltonians. In addition, these wavefunctions predict the binding energies as well as the excitation energies and spins of many unobserved states in every nucleus in the $\pi j4$ model space, including the binding energy of ^{100}Sn. We predict the $9/2^+$ excited state of ^{79}Cu, corresponding to the single-particle energy of the $0g_{9/2}$ orbital, and also the excited states of ^{99}In corresponding to the single-hole states in ^{100}Sn.

In addition to predicting the energies and spins of nuclear states, the p35-i3 Hamiltonian wavefunctions were used to predict the electromagnetic properties of every nucleus in the $\pi j4$ model space. The magnetic moment of each state in each nucleus was predicted, and agrees with the known experimental magnetic moments for all nuclei in the model space to within 0.50 (μ_N). The low-lying magnetic moments (and their corresponding g-factors) have a relative uniformity for a given J^π value, which indicates that each of these states contains dominant contributions from several configurations of the form $k^n = [nlj]^n$. The electric quadrupole moment of each state in each nucleus was predicted and agrees with the known experimental quadrupole moments to within and RMSD of 3 ($e \cdot \mathrm{fm}^2$). We observe the consequences of these k^n dominant configurations in the electric quadrupole moments by observing their smooth increase in Figures 5.12 and 5.14 as the number of protons occupying each orbital k increases. The $B(M1)$ and $B(E2)$ values for transitions

between all states are predicted and agree within the experimental and theoretical uncertainties. We predict 2 regions of enhanced collectivity in the $E2$ transitions for the nuclei in the $\pi j4$ model space. These regions correspond to nuclei whose low-lying states are dominated by configurations in a half-filled fp shell and those with a filled fp shell and a half-filled $0g_{9/2}$ orbital.

Little experimental information is known about the spin-energy structure or electromagnetic properties of nuclei at the edges of this model space. These predictions are a motivation for future experiments on the neutron-rich side of the model space, toward ^{78}Ni, and on the proton rich side, toward ^{100}Sn. Several astrophysical processes are thought to pass through the $\pi j4$ model space, with the doubly magic ^{78}Ni being important for the r-process and the doubly magic ^{100}Sn being important for the rp-process. Calculations with our Hamiltonian will supplement the experimental nuclear data needed for astrophysical applications.

BIBLIOGRAPHY

[1] J. A. Purcell et al. “Improving the predictive power of empirical shell-model Hamiltonians”. In: *Phys. Rev. C* 111 (4 Apr. 2025), p. 044313. DOI: 10.1103/PhysRevC.111.044313. URL: https://link.aps.org/doi/10.1103/PhysRevC.111.044313.

[2] NNDC. In: (2025). URL: https://www.nndc.bnl.gov/.

[3] G. Gamow and Ernest Rutherford. “Mass defect curve and nuclear constitution”. In: *Proceedings of the Royal Society of London. Series A, Containing Papers of a Mathematical and Physical Character* 126.803 (1930), pp. 632–644. DOI: 10.1098/rspa.1930.0032. eprint: https://royalsocietypublishing.org/doi/pdf/10.1098/rspa.1930.0032. URL: https://royalsocietypublishing.org/doi/abs/10.1098/rspa.1930.0032.

[4] Wikimedia Commons. *File:Liquid drop model.svg — Wikimedia Commons, the free media repository*. [Online; accessed 22-May-2025]. 2024. URL: https://commons.wikimedia.org/w/index.php?title=File:Liquid_drop_model.svg&oldid=962675187.

[5] B. Alex Brown. “Lecture Notes in Nuclear Structure Physics”. In: (2024). URL: https://people.frib.msu.edu/~brown/xx/brown-lecture-notes-2024.

[6] E.F. Saeed. “Utilizing a Visual Method, Focuses on the Modeling of the Semi-empirical Mass Formula "SEMF" in Nuclear Physics”. In: *J. Radiol Oncol.* 8 (2024), pp. 051–054. DOI: 10.29328/journal.jro.1001064. URL: https://www.radiooncologyjournal.com/articles/jro-aid1064.php.

[7] Maria Goeppert Mayer. “Nuclear Configurations in the Spin-Orbit Coupling Model. II. Theoretical Considerations”. In: *Phys. Rev.* 78 (1 Apr. 1950), pp. 22–23. DOI: 10.1103/PhysRev.78.22. URL: https://link.aps.org/doi/10.1103/PhysRev.78.22.

[8] B. Alex Brown. “Nuclear Pairing Gap: How Low Can It Go?” In: *Phys. Rev. Lett.* 111 (16 Oct. 2013), p. 162502. DOI: 10.1103/PhysRevLett.111.162502. URL: https://link.aps.org/doi/10.1103/PhysRevLett.111.162502.

[9] A. Magilligan and B. A. Brown. “New isospin-breaking “USD” Hamiltonians for the sd shell”. In: *Phys. Rev. C* 101 (6 June 2020), p. 064312. DOI: 10.1103/PhysRevC.101.064312. URL: https://link.aps.org/doi/10.1103/PhysRevC.101.064312.

[10] Xiangdong Ji and B. H. Wildenthal. “Shell-model predictions for electromagnetic properties of N=50 nuclei”. In: *Phys. Rev. C* 38 (6 Dec. 1988), pp. 2849–2859. DOI: 10.1103/PhysRevC.38.2849. URL: https://link.aps.org/doi/10.1103/PhysRevC.38.2849.

[11] S. Typel and B. A. Brown. “Skyrme Hartree-Fock calculations for the α-decay Q values of superheavy nuclei”. In: *Phys. Rev. C* 67 (3 Mar. 2003), p. 034313. DOI: 10.1103/

PhysRevC.67.034313. URL: https://link.aps.org/doi/10.1103/PhysRevC.67.034313.

[12] I. Talmi and I. Unna. "Energy levels and configuration interaction in Zr90 and related nuclei". In: *Nuclear Physics* 19 (1960), pp. 225–242. ISSN: 0029-5582. DOI: https://doi.org/10.1016/0029-5582(60)90234-0. URL: https://www.sciencedirect.com/science/article/pii/0029558260902340.

[13] Xiangdong Ji and B. H. Wildenthal. "Effective interaction for N=50 isotones". In: *Phys. Rev. C* 37 (3 Mar. 1988), pp. 1256–1266. DOI: 10.1103/PhysRevC.37.1256. URL: https://link.aps.org/doi/10.1103/PhysRevC.37.1256.

[14] A. F. Lisetskiy et al. "New $T = 1$ effective interactions for the $f_{52}\ p_{32}\ p_{12}\ g_{92}$ model space: Implications for valence-mirror symmetry and seniority isomers". In: *Phys. Rev. C* 70 (4 Oct. 2004), p. 044314. DOI: 10.1103/PhysRevC.70.044314. URL: https://link.aps.org/doi/10.1103/PhysRevC.70.044314.

[15] R.Overstreet L.Jacobson. "Mass Assignment of the Chain 65d ^{95}Zr - 35d ^{95}Nb and Notes on Other Niobium Activities". In: *Nat. Nucl. Ener. Ser.* 9 (1951), p. 735.

[16] K. -L. Kratz et al. "Neutron-rich isotopes around the r-process "waiting-point"nuclei2979Cu50 and3080Zn50". In: *Zeitschrift für Physik A Hadrons and Nuclei* 340.4 (1991), pp. 419–420. DOI: 10.1007/BF01290331. URL: https://doi.org/10.1007/BF01290331.

[17] R. Schneider et al. "Production and identification of100Sn". In: *Zeitschrift für Physik A Hadrons and Nuclei* 348.4 (1994), pp. 241–242. DOI: 10.1007/BF01305875. URL: https://doi.org/10.1007/BF01305875.

[18] "From ENSDF database as of January5, 2025. Version available at http://www.nndc.bnl.gov/ensarchivals/". In: (2025). URL: http://www.nndc.bnl.gov/ensarchivals/.

[19] S. M. Mullins, D. L. Watson, and H. T. Fortune. "^{82}Se(t,p)^{84}Se reaction at 17 MeV". in: *Phys. Rev. C* 37 (2 Feb. 1988), pp. 587–594. DOI: 10.1103/PhysRevC.37.587. URL: https://link.aps.org/doi/10.1103/PhysRevC.37.587.

[20] Morten Hjorth-Jensen, Thomas T.S. Kuo, and Eivind Osnes. "Realistic effective interactions for nuclear systems". In: *Physics Reports* 261.3 (1995), pp. 125–270. ISSN: 0370-1573. DOI: https://doi.org/10.1016/0370-1573(95)00012-6. URL: https://www.sciencedirect.com/science/article/pii/0370157395000126.

[21] Z. H. Sun et al. "Shell-model coupled-cluster method for open-shell nuclei". In: *Phys. Rev. C* 98 (5 Nov. 2018), p. 054320. DOI: 10.1103/PhysRevC.98.054320. URL: https://link.aps.org/doi/10.1103/PhysRevC.98.054320.

[22] S. Ragnar Stroberg et al. "Nonempirical Interactions for the Nuclear Shell Model: An

Update". In: *Annual Review of Nuclear and Particle Science* 69.Volume 69, 2019 (2019), pp. 307–362. ISSN: 1545-4134. DOI: https://doi.org/10.1146/annurev-nucl-101917-021120. URL: https://www.annualreviews.org/content/journals/10.1146/annurev-nucl-101917-02

[23] K. Hebeler et al. "Improved nuclear matter calculations from chiral low-momentum interactions". In: *Phys. Rev. C* 83 (3 Mar. 2011), p. 031301. DOI: 10.1103/PhysRevC.83.031301. URL: https://link.aps.org/doi/10.1103/PhysRevC.83.031301.

[24] B. C. He and S. R. Stroberg. "Factorized approximation to the in-medium similarity renormalization III group IMSRG(3)". In: *Phys. Rev. C* 110 (2024), p. 044317.

[25] Qing-Song Xu and Yi-Zeng Liang. "Monte Carlo cross validation". In: *Chemometrics and Intelligent Laboratory Systems* 56.1 (2001), pp. 1–11. ISSN: 0169-7439. DOI: https://doi.org/10.1016/S0169-7439(00)00122-2. URL: https://www.sciencedirect.com/science/article/pii/S0169743900001222.

[26] Ping Zhang. "Model Selection Via Multifold Cross Validation". In: *The Annals of Statistics* 21.1 (1993), pp. 299–313. ISSN: 00905364, 21688966. URL: http://www.jstor.org/stable/3035592 (visited on 06/30/2025).

[27] V. Vaquero et al. "Fragmentation of Single-Particle Strength around the Doubly Magic Nucleus ^{132}Sn and the Position of the $0f_{5/2}$ Proton-Hole State in ^{131}In". In: *Phys. Rev. Lett.* 124 (2 Jan. 2020), p. 022501. DOI: 10.1103/PhysRevLett.124.022501. URL: https://link.aps.org/doi/10.1103/PhysRevLett.124.022501.

[28] Xiangdong Ji and B. H. Wildenthal. "Shell-model predictions for electromagnetic properties of N=50 nuclei". In: *Phys. Rev. C* 38 (6 Dec. 1988), pp. 2849–2859. DOI: 10.1103/PhysRevC.38.2849. URL: https://link.aps.org/doi/10.1103/PhysRevC.38.2849.

[29] B. Cheal et al. "Nuclear Spins and Moments of Ga Isotopes Reveal Sudden Structural Changes between $N = 40$ and $N = 50$". In: *Phys. Rev. Lett.* 104 (25 June 2010), p. 252502. DOI: 10.1103/PhysRevLett.104.252502. URL: https://link.aps.org/doi/10.1103/PhysRevLett.104.252502.

[30] G. J. Kumbartzki et al. "Transition from collectivity to single-particle degrees of freedom from magnetic moment measurements on $^{82}_{38}\mathrm{Sr}_{44}$ and $^{90}_{38}\mathrm{Sr}_{52}$". In: *Phys. Rev. C* 89 (6 June 2014), p. 064305. DOI: 10.1103/PhysRevC.89.064305. URL: https://link.aps.org/doi/10.1103/PhysRevC.89.064305.

[31] H.T. Duong et al. "Atomic beam magnetic resonance apparatus for systematic measurement of hyperfine structure anomalies (Bohr-Weisskopf effect)". In: *Nuclear Instruments and Methods in Physics Research Section A: Accelerators, Spectrometers, Detectors and Associated Equipment* 325.3 (1993), pp. 465–474. ISSN: 0168-9002. DOI: https://doi.org/10.1016/0168-9002(93)90392-U. URL: https://www.sciencedirect.

com/science/article/pii/016890029390392U.

[32] G. J. Kumbartzki et al. “Structure of the Sr-Zr isotopes near and at the magic $N = 50$ shell from g-factor and lifetime measurements in $^{88}_{40}$Zr and $^{84,86,88}_{38}$Sr”. In: *Phys. Rev. C* 85 (4 Apr. 2012), p. 044322. DOI: 10.1103/PhysRevC.85.044322. URL: https://link.aps.org/doi/10.1103/PhysRevC.85.044322.

[33] C. Haßler, J. Kronenbitter, and A. Schwenk. “89Yttrium nuclear magnetic resonance studies”. In: *Zeitschrift für Physik A Atoms and Nuclei* 280.2 (1977), pp. 117–123. DOI: 10.1007/BF01409538. URL: https://doi.org/10.1007/BF01409538.

[34] B. Cheal et al. “The shape transition in the neutron-rich yttrium isotopes and isomers”. In: *Physics Letters B* 645.2 (2007), pp. 133–137. ISSN: 0370-2693. DOI: https://doi.org/10.1016/j.physletb.2006.12.053. URL: https://www.sciencedirect.com/science/article/pii/S037026930601608X.

[35] Giulio Racah. “Theory of Complex Spectra. III”. in: *Phys. Rev.* 63 (9-10 May 1943), pp. 367–382. DOI: 10.1103/PhysRev.63.367. URL: https://link.aps.org/doi/10.1103/PhysRev.63.367.

[36] O. Häusser et al. “Magnetic moments of N=48–50 nuclei and proton core polarization”. In: *Hyperfine Interactions* 4.1 (1978), pp. 196–200.

[37] G. Jakob et al. “First measurements of the g factors of the 2+1 and 3â1 states of semi-magic 9040Zr”. In: *Physics Letters B* 494.3 (2000), pp. 187–192. ISSN: 0370-2693. DOI: https://doi.org/10.1016/S0370-2693(00)01197-7. URL: https://www.sciencedirect.com/science/article/pii/S0370269300011977.

[38] R. Eder, E. Hagn, and E. Zech. “Magnetic moment of the 0.8s 5â isomer 90mZr”. In: *Nuclear Physics A* 468.2 (1987), pp. 348–356. ISSN: 0375-9474. DOI: https://doi.org/10.1016/0375-9474(87)90521-5. URL: https://www.sciencedirect.com/science/article/pii/0375947487905215.

[39] O. Häusser et al. “Magnetic moments of N=48–50 nuclei and proton core polarization”. In: *Hyperfine Interactions* 4.1 (1978), pp. 196–200. DOI: 10.1007/BF01021824. URL: https://doi.org/10.1007/BF01021824.

[40] B. Cheal et al. “Laser Spectroscopy of Niobium Fission Fragments: First Use of Optical Pumping in an Ion Beam Cooler Buncher”. In: *Phys. Rev. Lett.* 102 (22 June 2009), p. 222501. DOI: 10.1103/PhysRevLett.102.222501. URL: https://link.aps.org/doi/10.1103/PhysRevLett.102.222501.

[41] Pramila Raghavan. “Table of nuclear moments”. In: *Atomic Data and Nuclear Data Tables* 42.2 (1989), pp. 189–291. ISSN: 0092-640X. DOI: https://doi.org/10.1016/0092-640X(89)90008-9. URL: https://www.sciencedirect.com/science/article/

pii/0092640X89900089.

[42] O. Häusser et al. “Magnetic moments of N = 50 isotones and proton core polarization”. In: *Nuclear Physics A* 293.1 (1977), pp. 248–268. ISSN: 0375-9474. DOI: https://doi.org/10.1016/0375-9474(77)90490-0. URL: https://www.sciencedirect.com/science/article/pii/0375947477904900.

[43] Andrzej BaÅanda et al. “The g-factor of the 21/2$^+$ state in ^{91}Nb”. eng. In: *Acta Physica Polonica. B* 8.2 (1977), 147â152. ISSN: 0587-4254. URL: https://ruj.uj.edu.pl/xmlui/handle/item/312544..

[44] P. F. Mantica et al. “g factors of the first 2$^+$ states in the transitional $^{92,94,96,98,100}Mo$ isotopes and the onset of collectivity”. In: *Phys. Rev. C* 63 (3 Feb. 2001), p. 034312. DOI: 10.1103/PhysRevC.63.034312. URL: https://link.aps.org/doi/10.1103/PhysRevC.63.034312.

[45] B. Hinfurtner et al. “Measurements of magnetic moments of Tc isotopes and the hyperfine field of Tc in Fe and Ni”. In: *Zeitschrift für Physik A Hadrons and Nuclei* 350.4 (1995), pp. 311–318. DOI: 10.1007/BF01291188. URL: https://doi.org/10.1007/BF01291188.

[46] H. Grawe and H. Haas. “The lifetime and g-factor of the 8+ state in 96Pd”. In: *Physics Letters B* 120.1 (1983), pp. 63–66. ISSN: 0370-2693. DOI: https://doi.org/10.1016/0370-2693(83)90623-8. URL: https://www.sciencedirect.com/science/article/pii/0370269383906238.

[47] R. Ferrer et al. “In-gas-cell laser ionization spectroscopy in the vicinity of 100Sn: Magnetic moments and mean-square charge radii of N=50â54 Ag”. In: *Physics Letters B* 728 (2014), pp. 191–197. ISSN: 0370-2693. DOI: https://doi.org/10.1016/j.physletb.2013.11.055. URL: https://www.sciencedirect.com/science/article/pii/S0370269313009611.

[48] D. Feiertag and G. zu Putlitz. “Hyperfine structure,gjfactors and lifetimes of excited2P1/2 states of Rb”. In: *Zeitschrift für Physik A Hadrons and nuclei* 261.1 (1973), pp. 1–12.

[49] P. Raghavan et al. “$E2$ Effective Charges of $g_{\frac{9}{2}}$ Nucleons Derived from Quadrupole Moments of High-Spin Isomers in $^{88,90,91}Zr$ and $^{90,92,94}Mo$”. In: *Phys. Rev. Lett.* 54 (24 June 1985), pp. 2592–2595. DOI: 10.1103/PhysRevLett.54.2592. URL: https://link.aps.org/doi/10.1103/PhysRevLett.54.2592.

[50] Bhoomika Maheshwari and Kosuke Nomura. “Overview of Seniority Isomers”. In: *Symmetry* 14.12 (2022). ISSN: 2073-8994. DOI: 10.3390/sym14122680. URL: https://www.mdpi.com/2073-8994/14/12/2680.

[51] J. Van de Walle et al. “Low-energy Coulomb excitation of neutron-rich zinc isotopes”. In:

Phys. Rev. C 79 (1 Jan. 2009), p. 014309. DOI: 10.1103/PhysRevC.79.014309. URL: https://link.aps.org/doi/10.1103/PhysRevC.79.014309.

[52] A. Gade et al. "Collectivity at $N = 50$: ^{82}Ge and ^{84}Se". In: *Phys. Rev. C* 81 (6 June 2010), p. 064326. DOI: 10.1103/PhysRevC.81.064326. URL: https://link.aps.org/doi/10.1103/PhysRevC.81.064326.

[53] B. Pritychenko et al. "Tables of E2 transition probabilities from the first states in even–even nuclei". In: *Atomic Data and Nuclear Data Tables* 107 (Jan. 2016), pp. 1–139. ISSN: 0092-640X. DOI: 10.1016/j.adt.2015.10.001. URL: http://dx.doi.org/10.1016/j.adt.2015.10.001.

[54] B. Pritychenko, M. Birch, and B. Singh. "Revisiting Grodzins systematics of B(E2) values". In: *Nuclear Physics A* 962 (2017), pp. 73–102. ISSN: 0375-9474. DOI: https://doi.org/10.1016/j.nuclphysa.2017.03.011. URL: https://www.sciencedirect.com/science/article/pii/S037594741730057X.

[55] R. M. Pérez-Vidal et al. "Evidence of Partial Seniority Conservation in the $\pi g_{9/2}$ Shell for the $N = 50$ Isotones". In: *Phys. Rev. Lett.* 129 (11 Sept. 2022), p. 112501. DOI: 10.1103/PhysRevLett.129.112501. URL: https://link.aps.org/doi/10.1103/PhysRevLett.129.112501.

[56] M. Ley et al. "Lifetime measurements in ^{92}Mo: Investigation of seniority conservation in the $N = 50$ isotones". In: *Phys. Rev. C* 108 (6 Dec. 2023), p. 064313. DOI: 10.1103/PhysRevC.108.064313. URL: https://link.aps.org/doi/10.1103/PhysRevC.108.064313.

[57] D. Alber et al. "Nuclear structure studies of the neutron deficientN=50 nucleus96Pd". In: *Zeitschrift für Physik A Atomic Nuclei* 332.2 (1989), pp. 129–135. DOI: 10.1007/BF01289767. URL: https://doi.org/10.1007/BF01289767.

[58] G. Zhang et al. "Approaching 100Sn: Structural evolution in 98,100Cd via lifetime measurements". In: *Physics Letters B* 863 (2025), p. 139378. ISSN: 0370-2693. DOI: https://doi.org/10.1016/j.physletb.2025.139378. URL: https://www.sciencedirect.com/science/article/pii/S0370269325001388.

APPENDIX A

ENERGY SPECTRA

Below are a collection of the energy spectra for all of the nuclei involved in the $\pi j4$ model space. The figures are divided into two regions: the left region shows the experimental spin-energy data and the right region shows the corresponding predictions that come from our p35i3 effective interaction. Each figure spans the energy range from 0 MeV (the ground state) to 6 MeV; it should be noted that both experimental data and predictions can extend beyond this range, but we cut off at 6 MeV for illustrative purposes. In addition, each nuclear energy level has a line whose length indicates the spin value and whose color indicates the parity (red for positive and blue for negative). Some levels are shown with enlarged circles on the ends; these are the data that were used to fit our interaction. Some levels are shown with a black dot at the ends; this indicates that the spin-parity is tentatively assigned from experiment. Some levels are shown with no line and only a black dot; this indicates that there are observed nuclear excitations of known energy, but the corresponding spin-parity is not experimentally known. Finally, there are a few states marked with a black X, the two states between 2 MeV and 3 MeV in ^{84}Se, for example; these states have experimental evidence of being intruder states and contain a substantial contribution from configurations outside of the model space such as neutron particle-hole excitations across the shell gap.

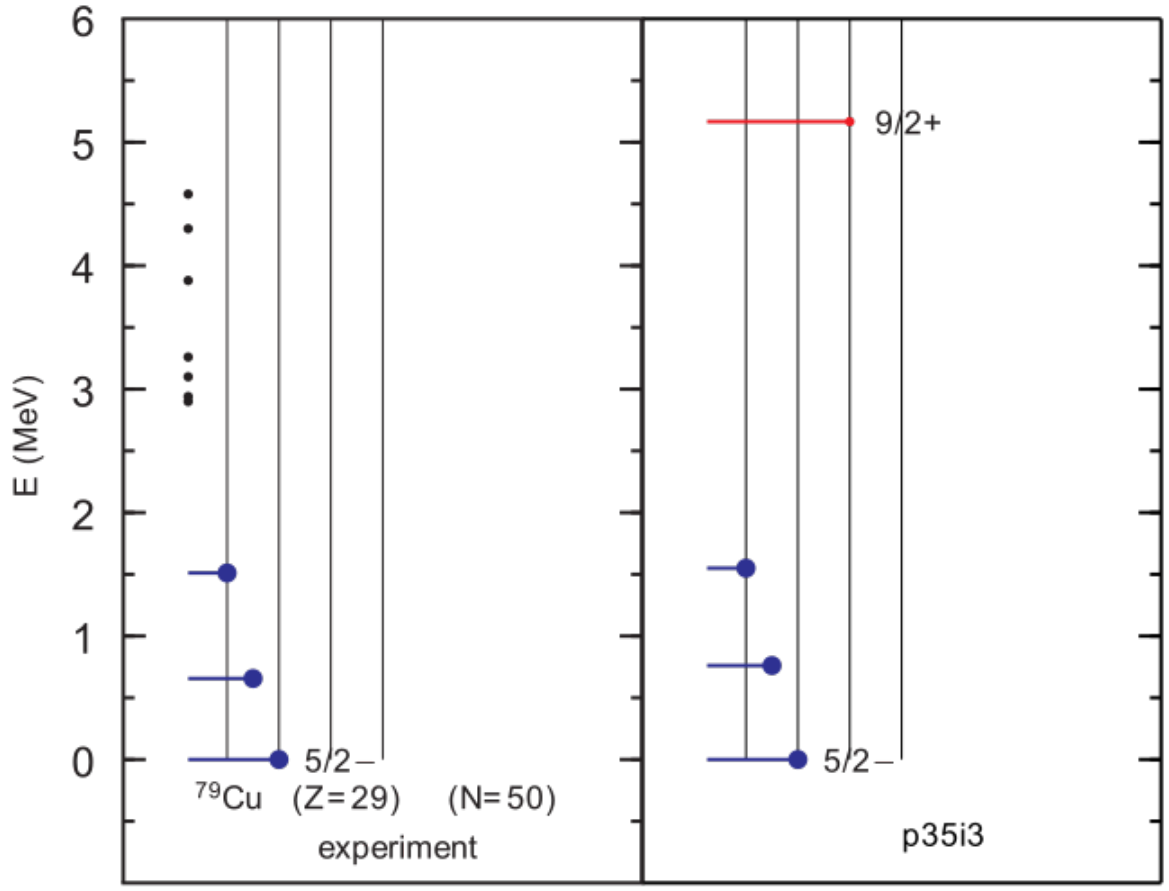

Figure A1 Energy Spectrum of ^{79}Cu.

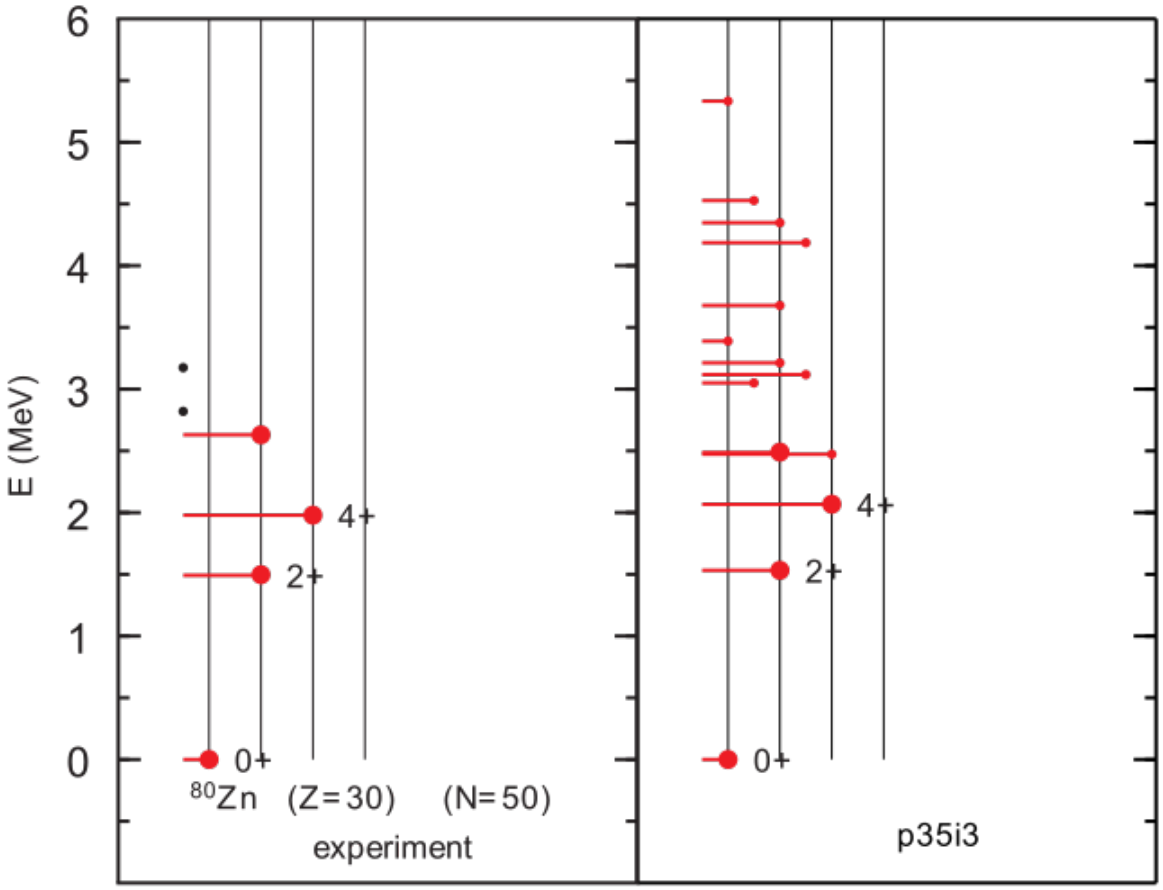

Figure A2 Energy Spectrum of ^{80}Zn.

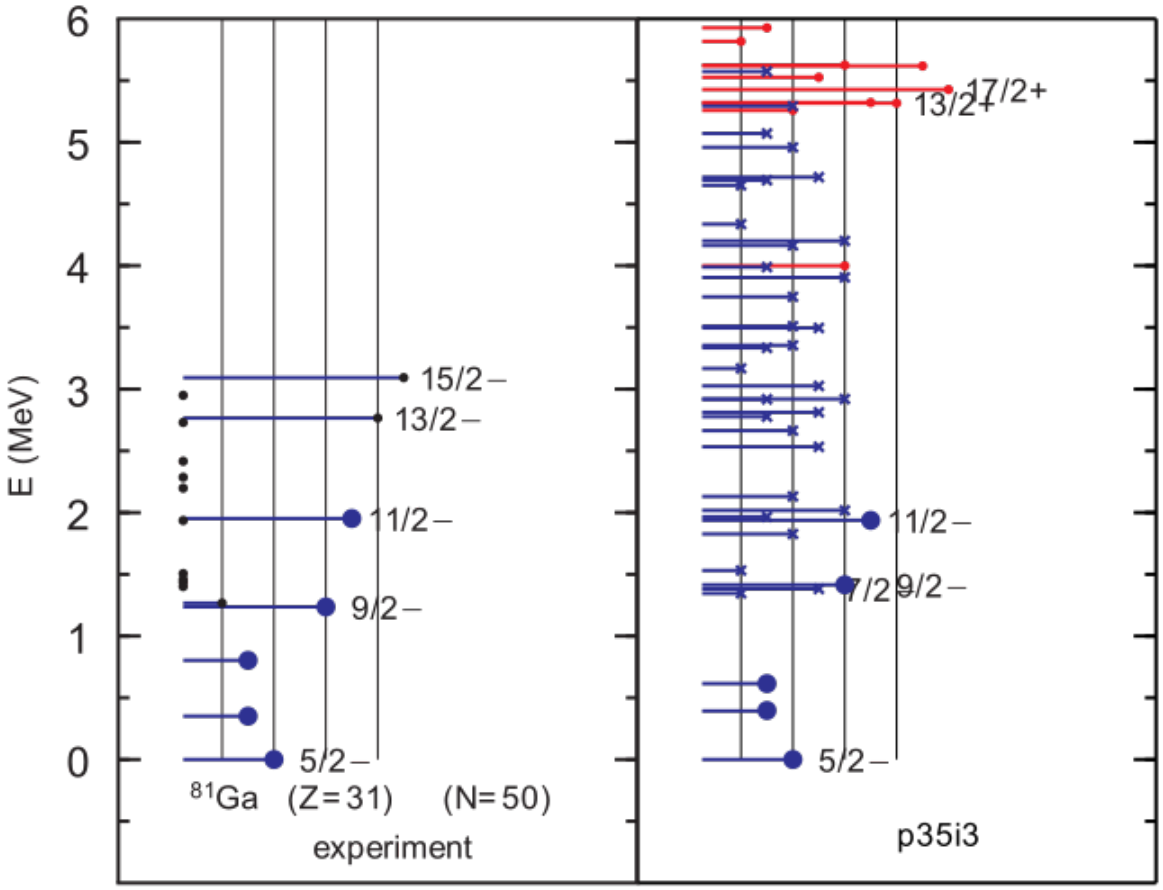

Figure A3 Energy Spectrum of ^{81}Ga.

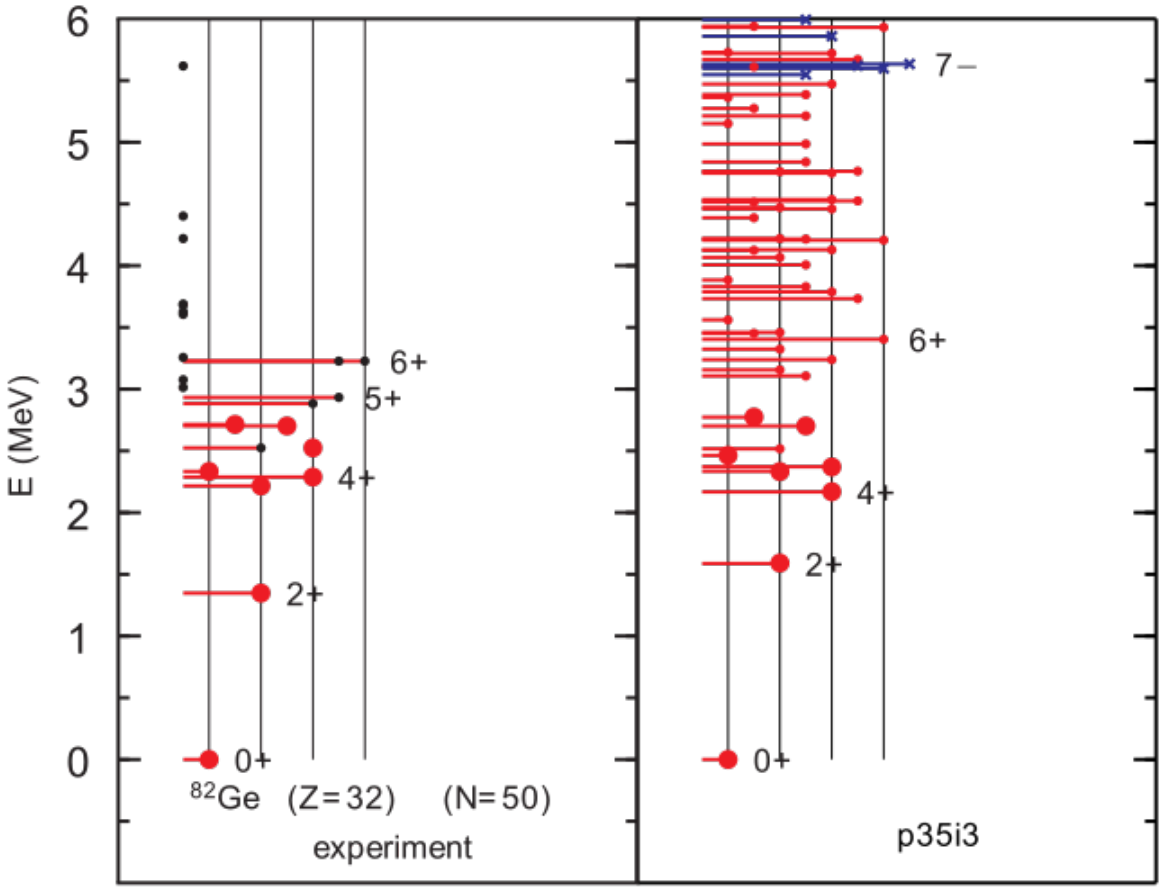

Figure A4 Energy Spectrum of ^{82}Ge.

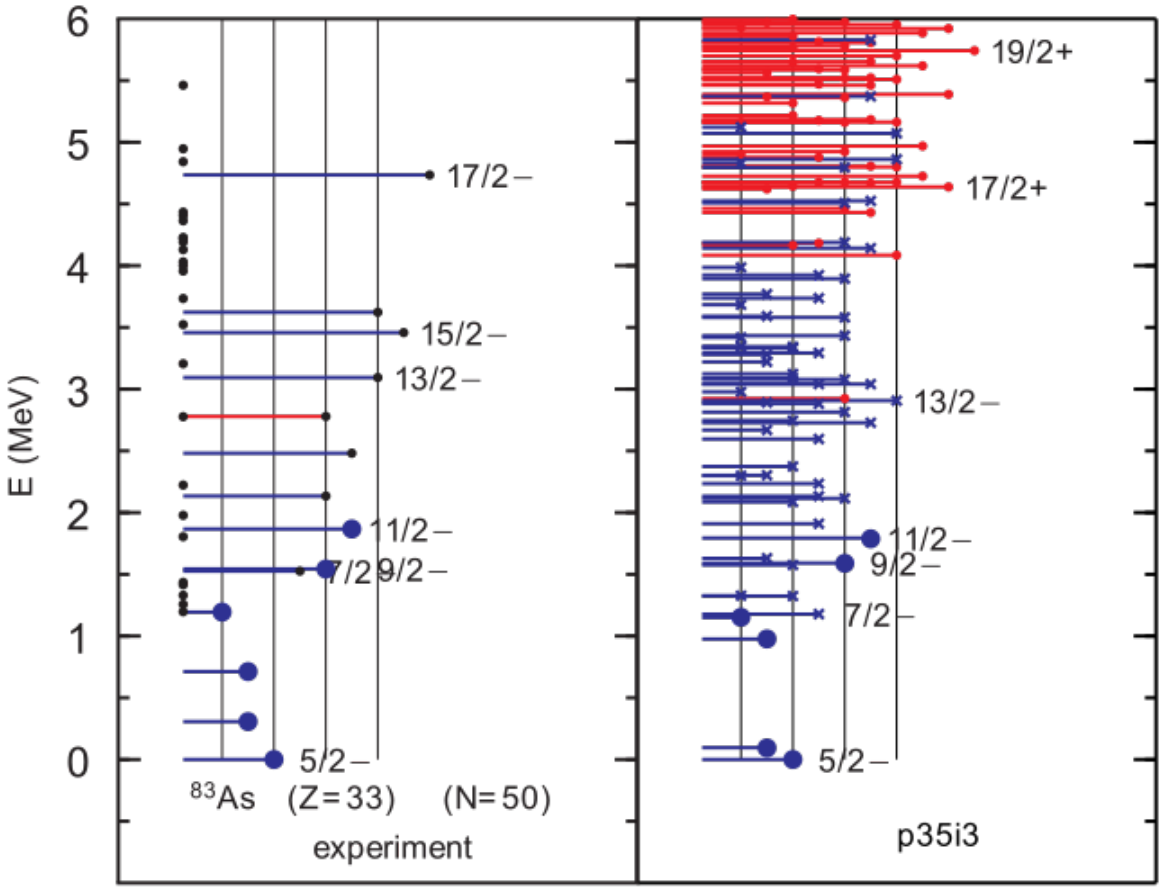

Figure A5 Energy Spectrum of ^{83}As.

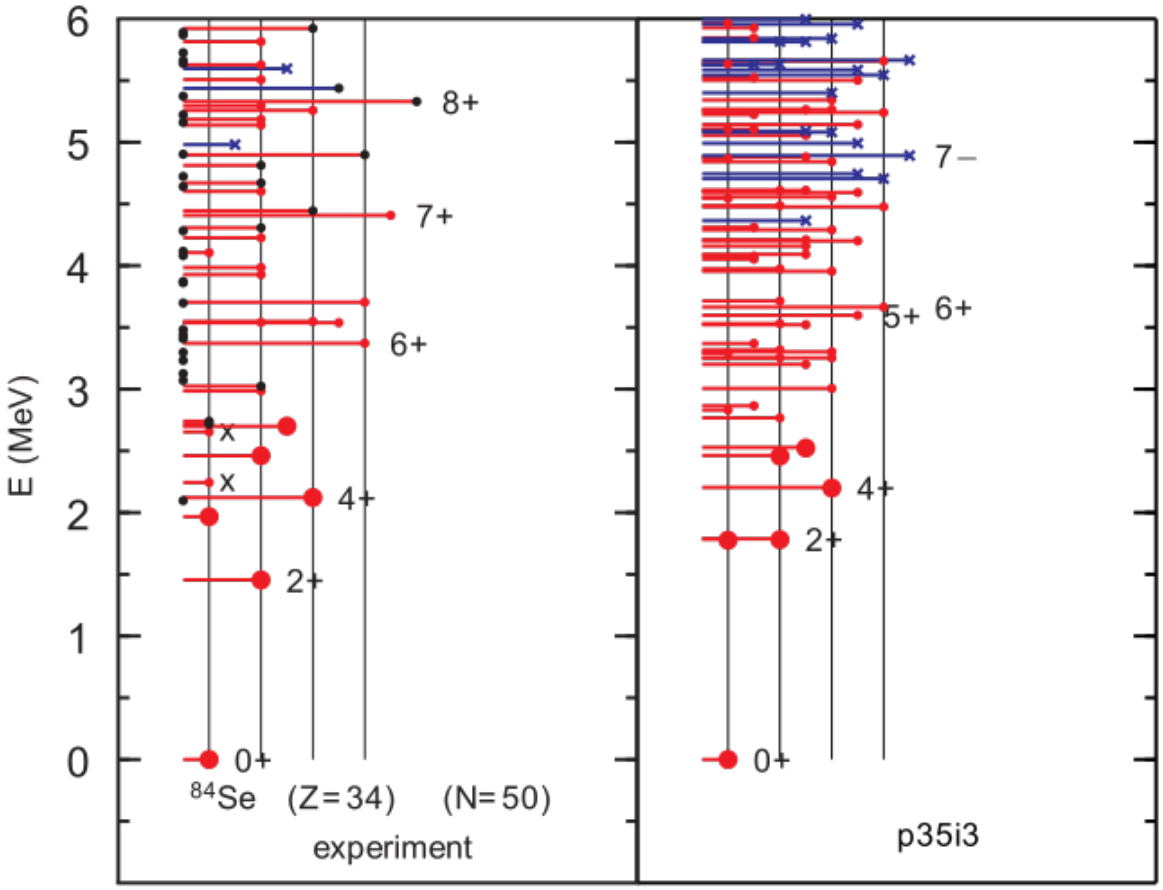

Figure A6 Energy Spectrum of ^{84}Se.

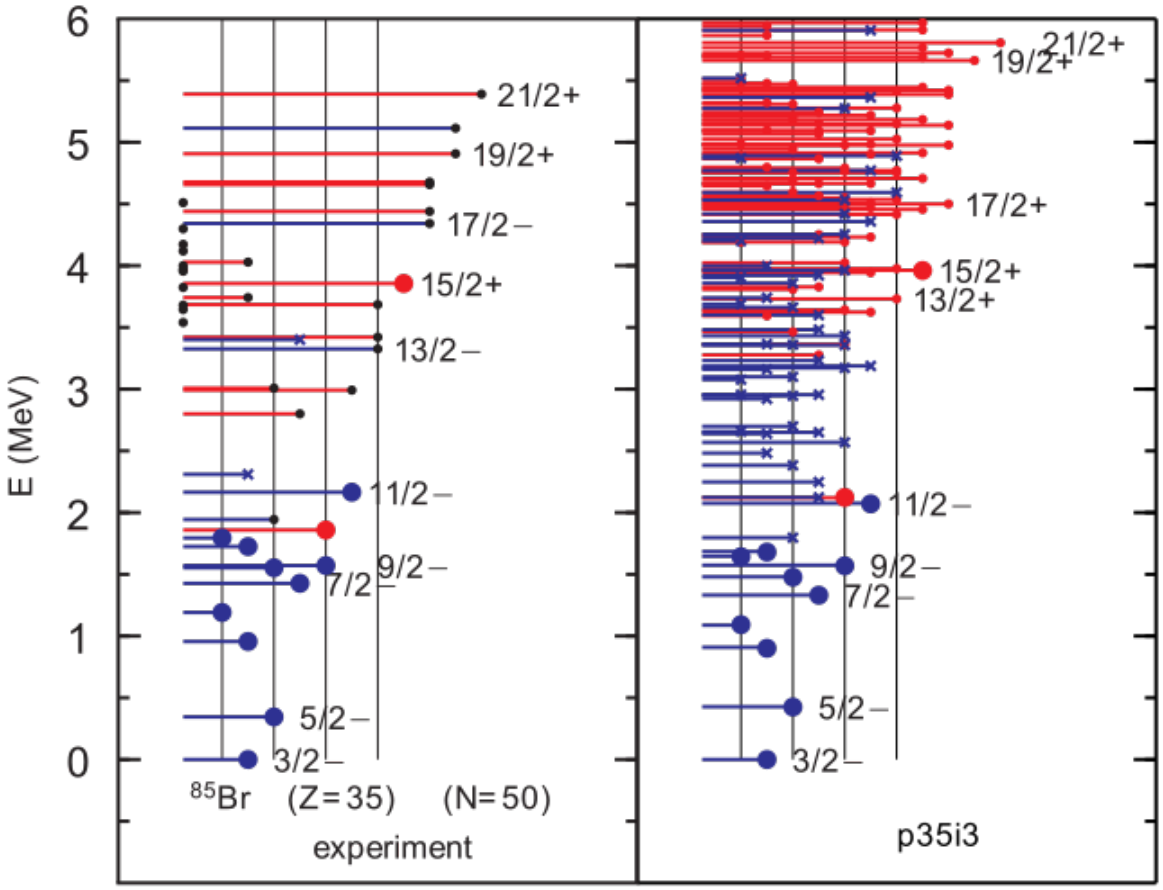

Figure A7 Energy Spectrum of ^{85}Br.

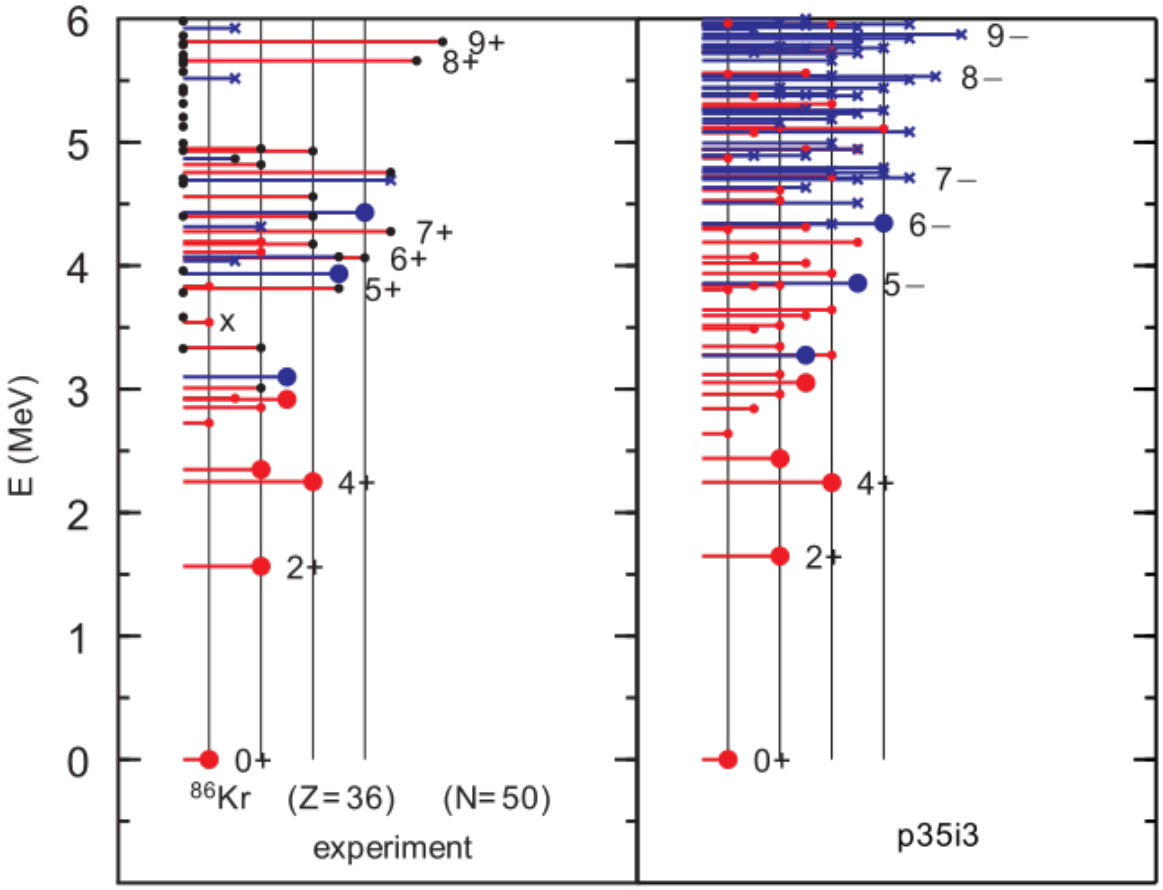

Figure A8 Energy Spectrum of ^{86}Kr.

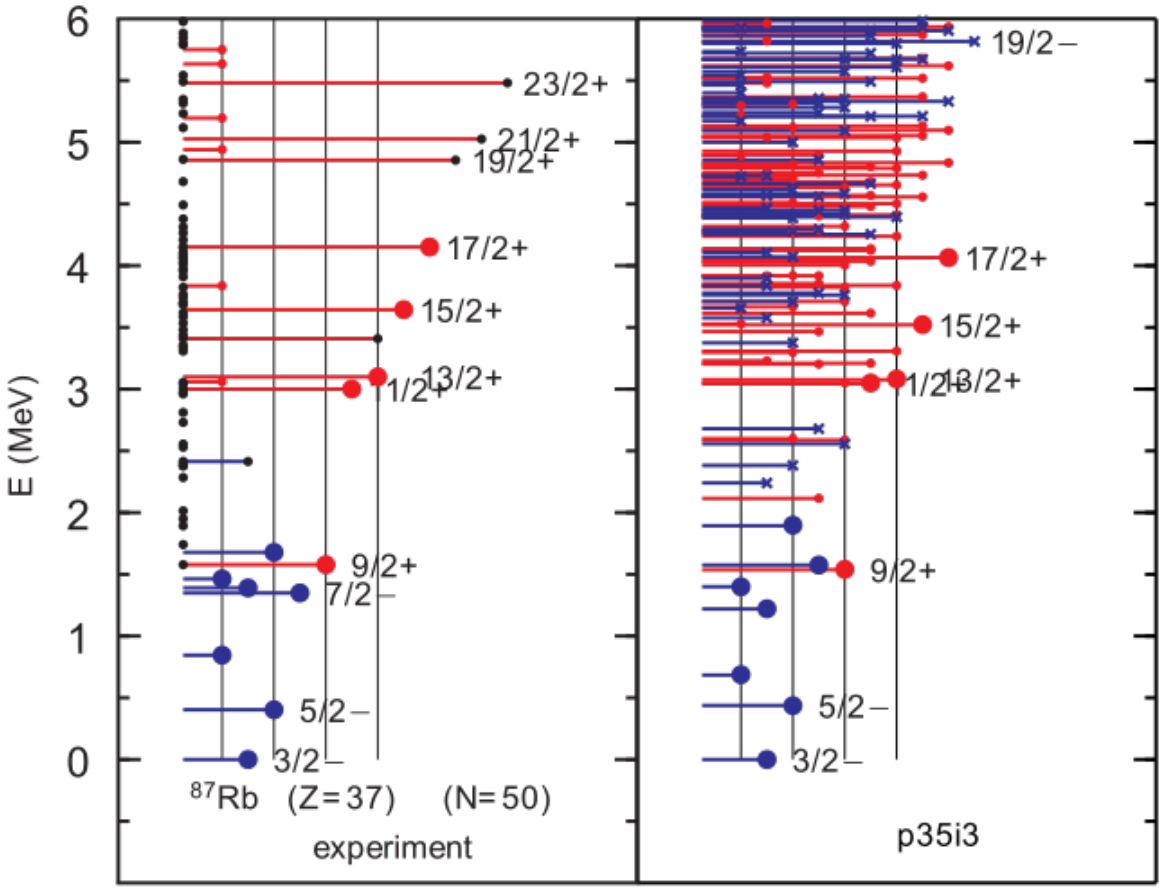

Figure A9 Energy Spectrum of ^{87}Rb.

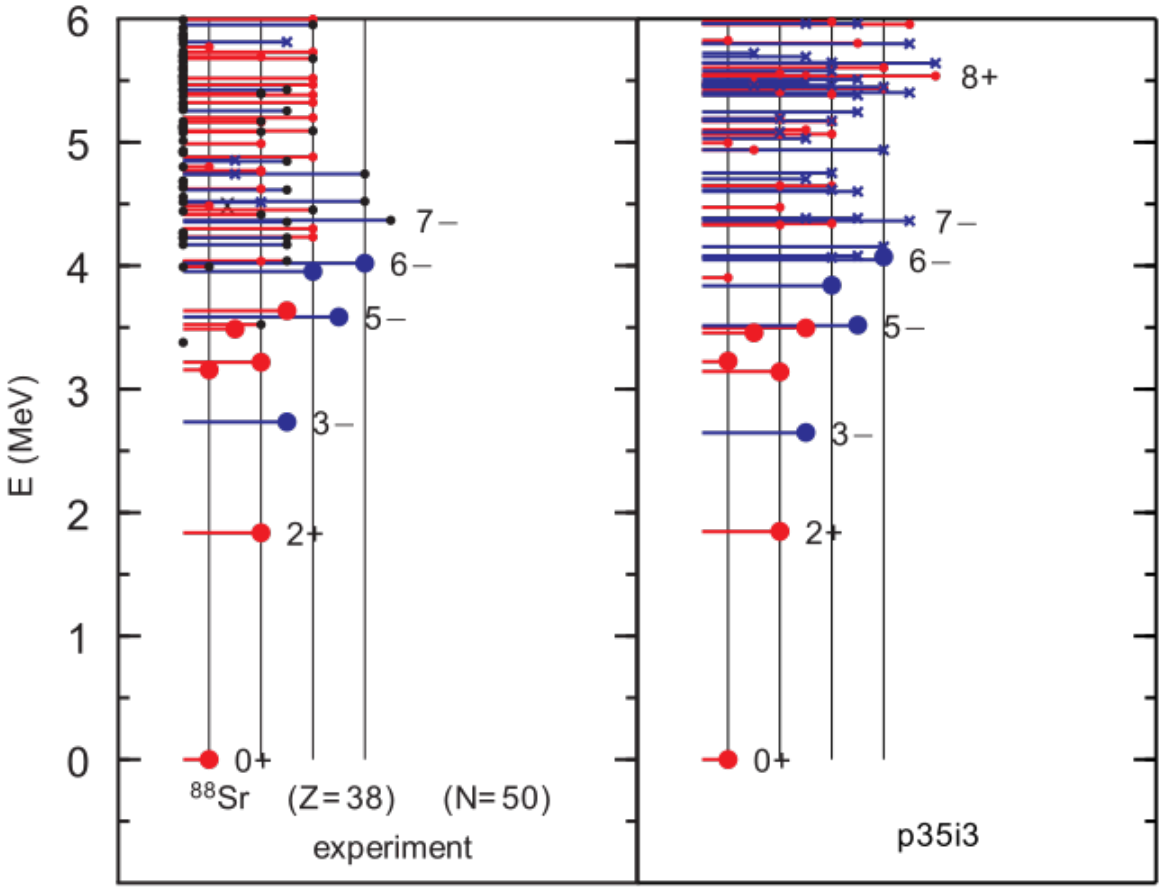

Figure A10 Energy Spectrum of ^{88}Sr.

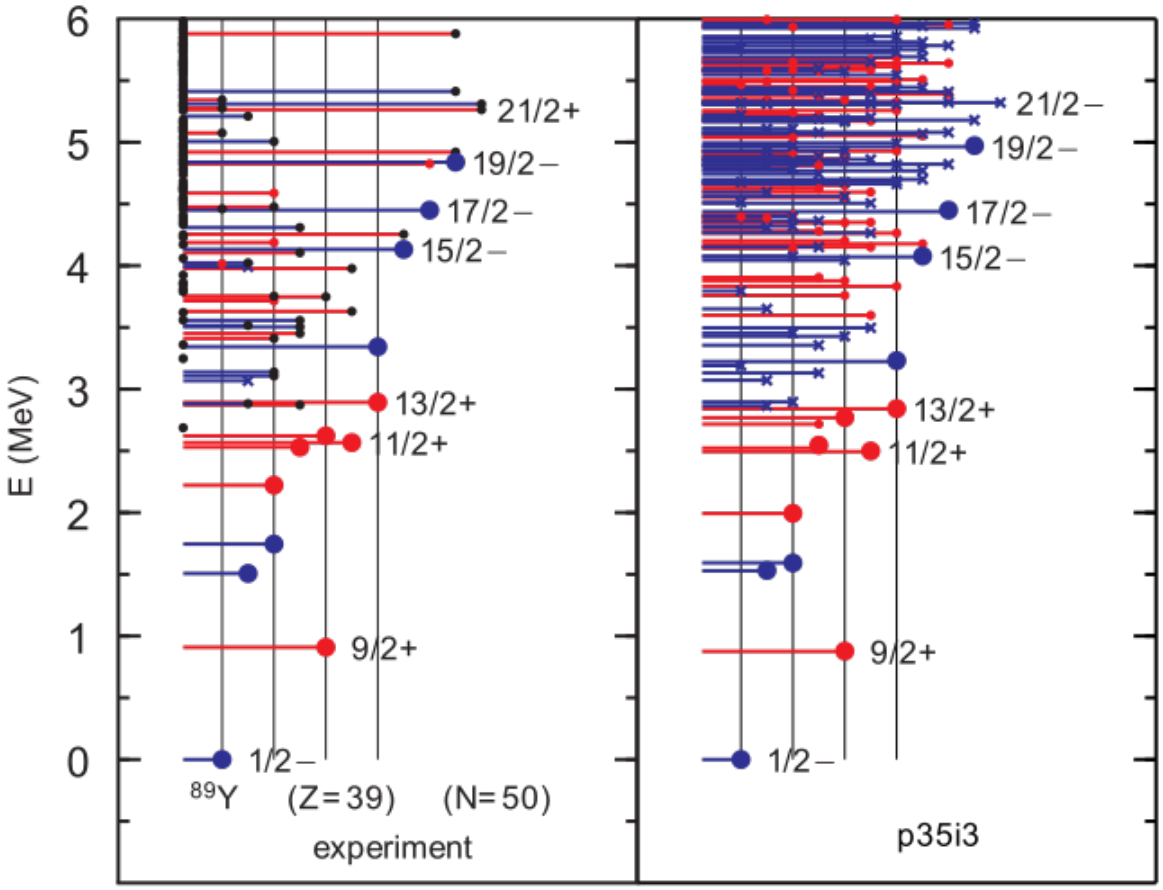

Figure A11 Energy Spectrum of ^{89}Y.

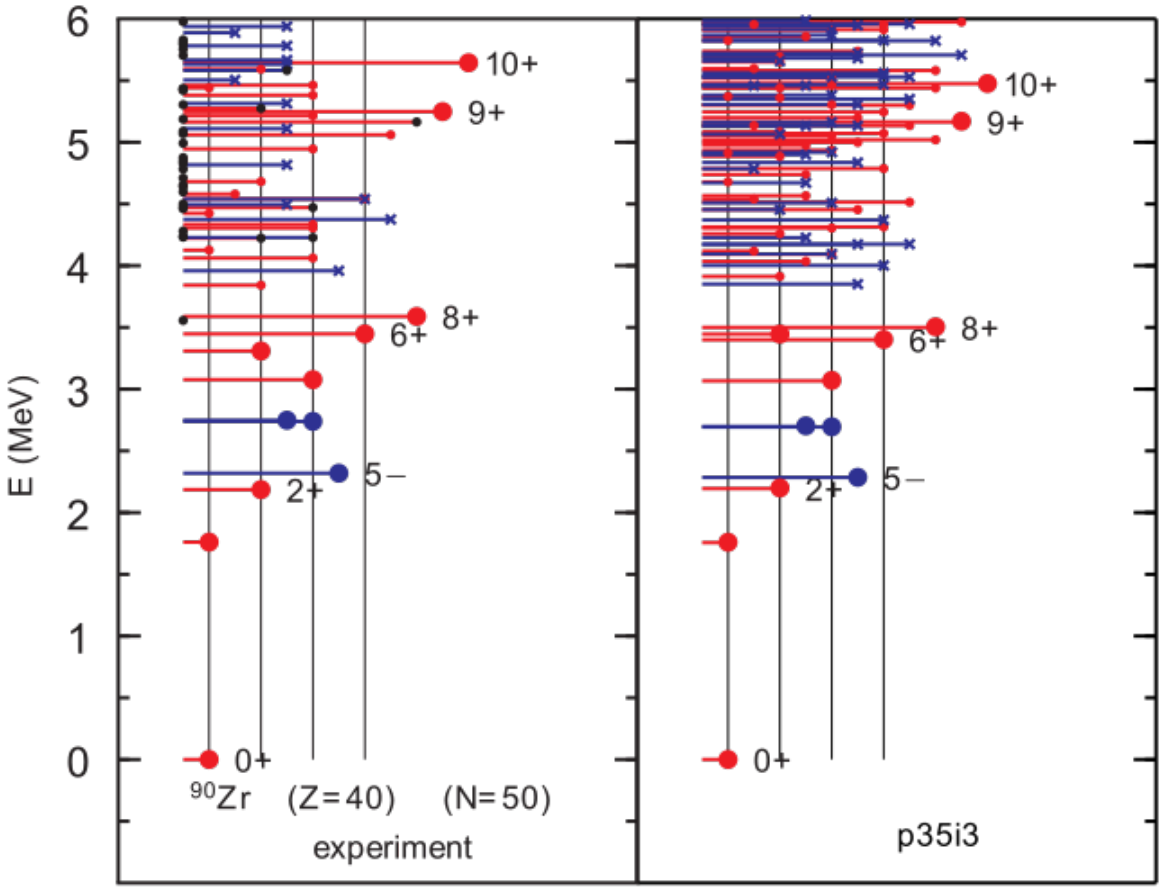

Figure A12 Energy Spectrum of ^{90}Zr.

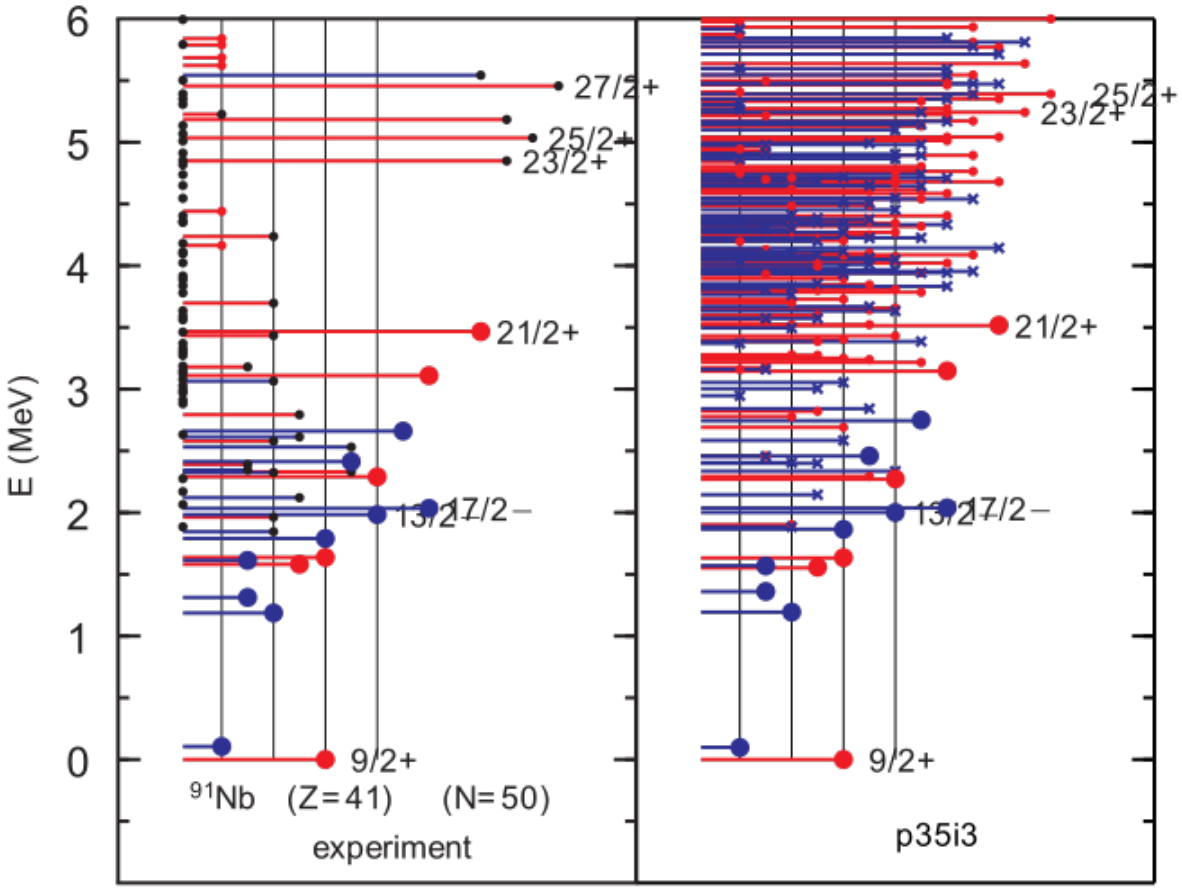

Figure A13 Energy Spectrum of ^{91}Nb.

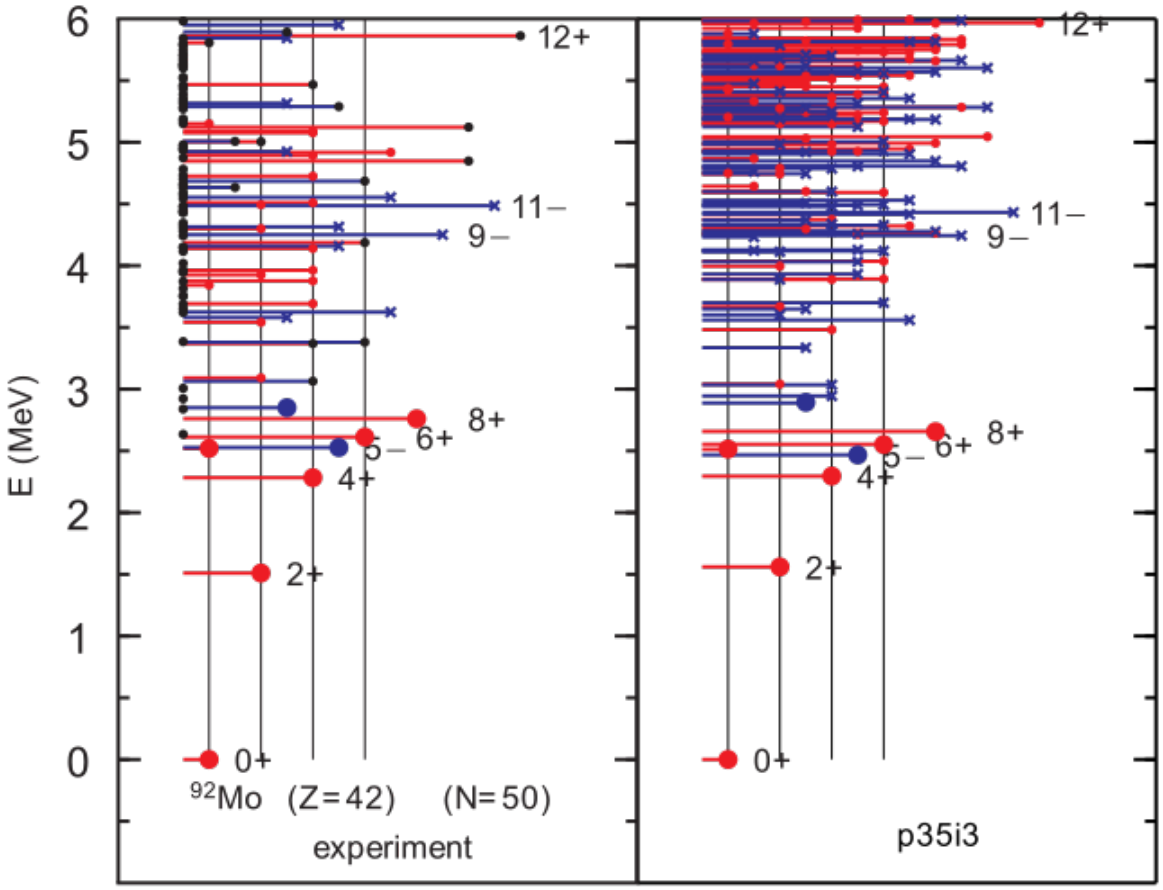

Figure A14 Energy Spectrum of ^{92}Mo.

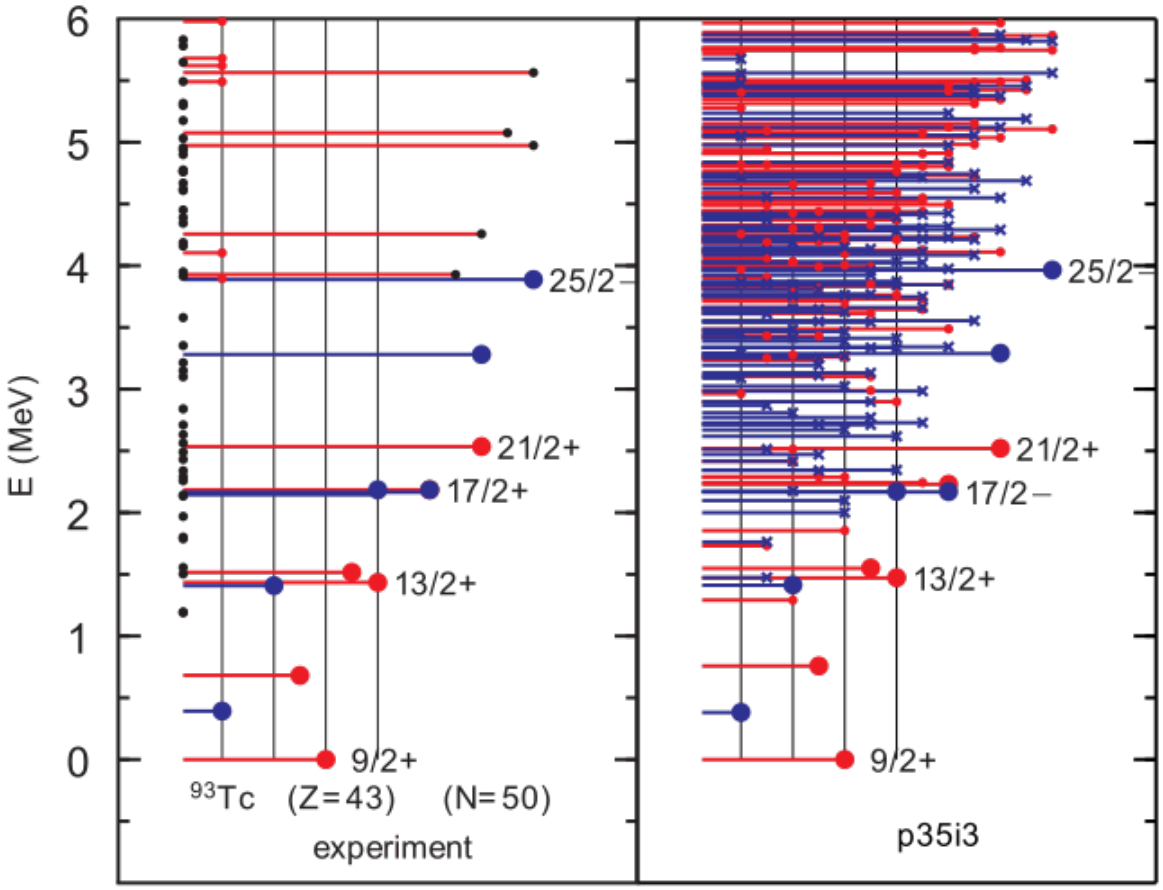

Figure A15 Energy Spectrum of ^{93}Tc.

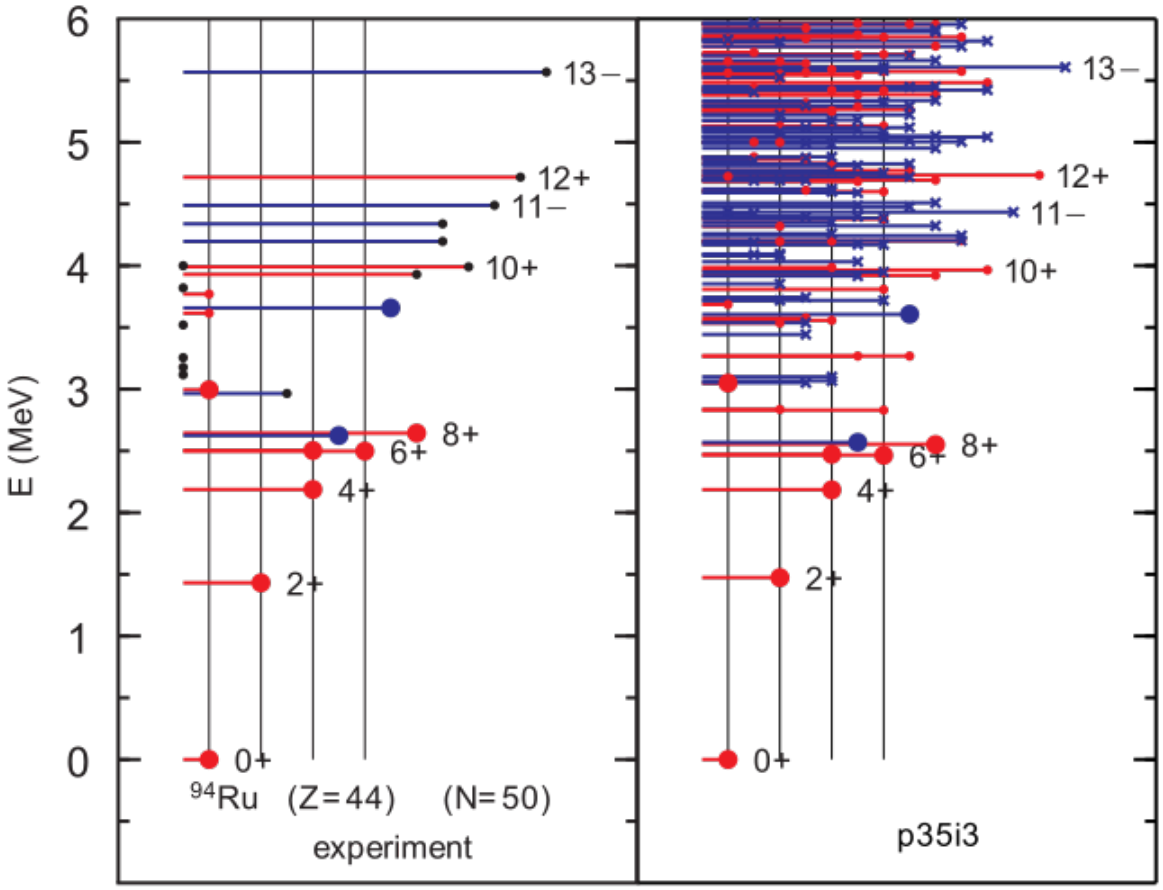

Figure A16 Energy Spectrum of ^{94}Ru.

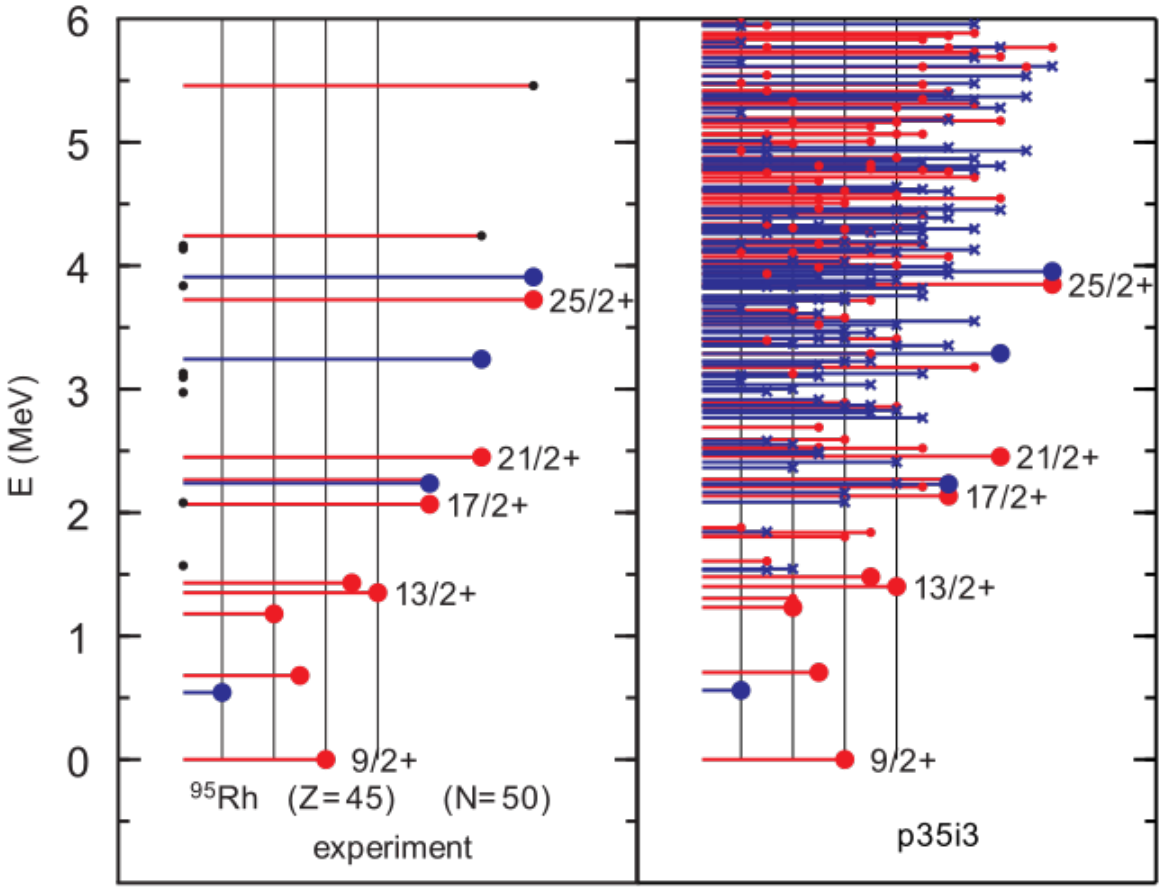

Figure A17 Energy Spectrum of ^{95}Rh.

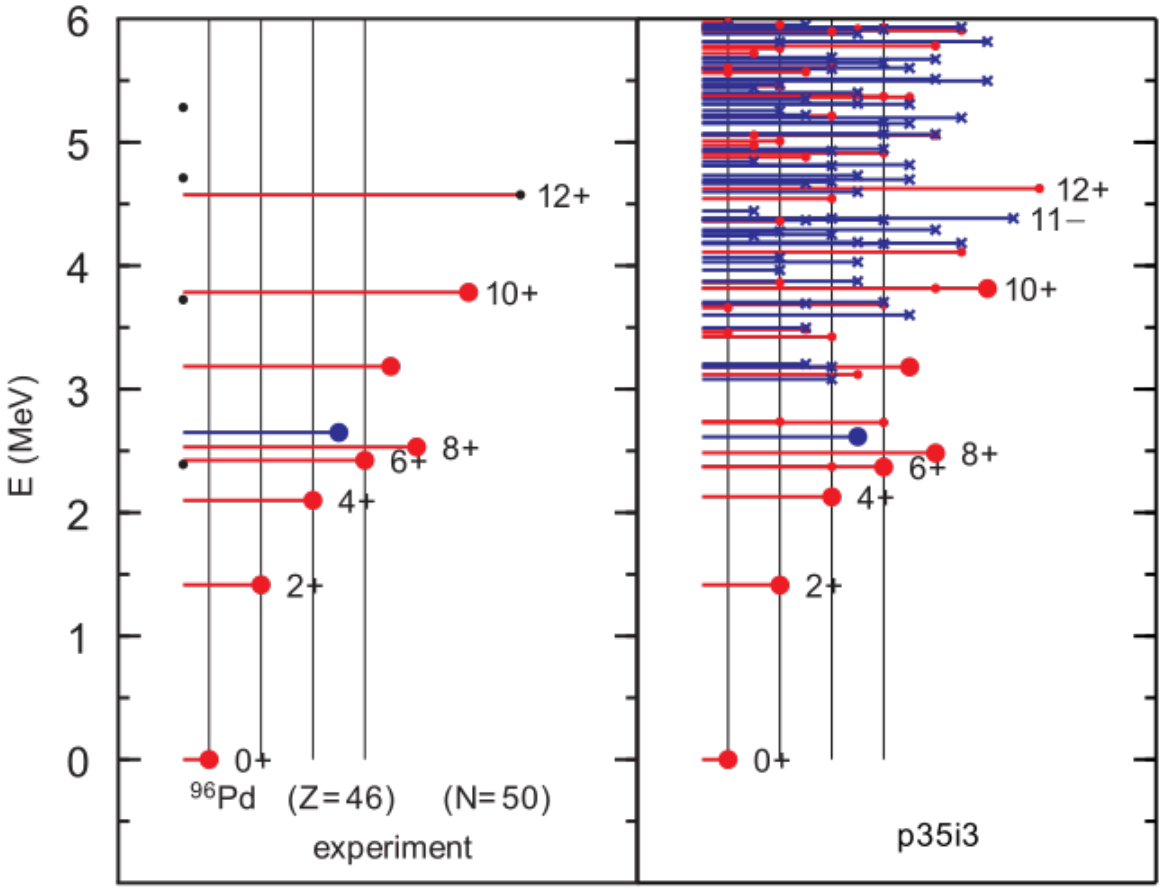

Figure A18 Energy Spectrum of ^{96}Pd.

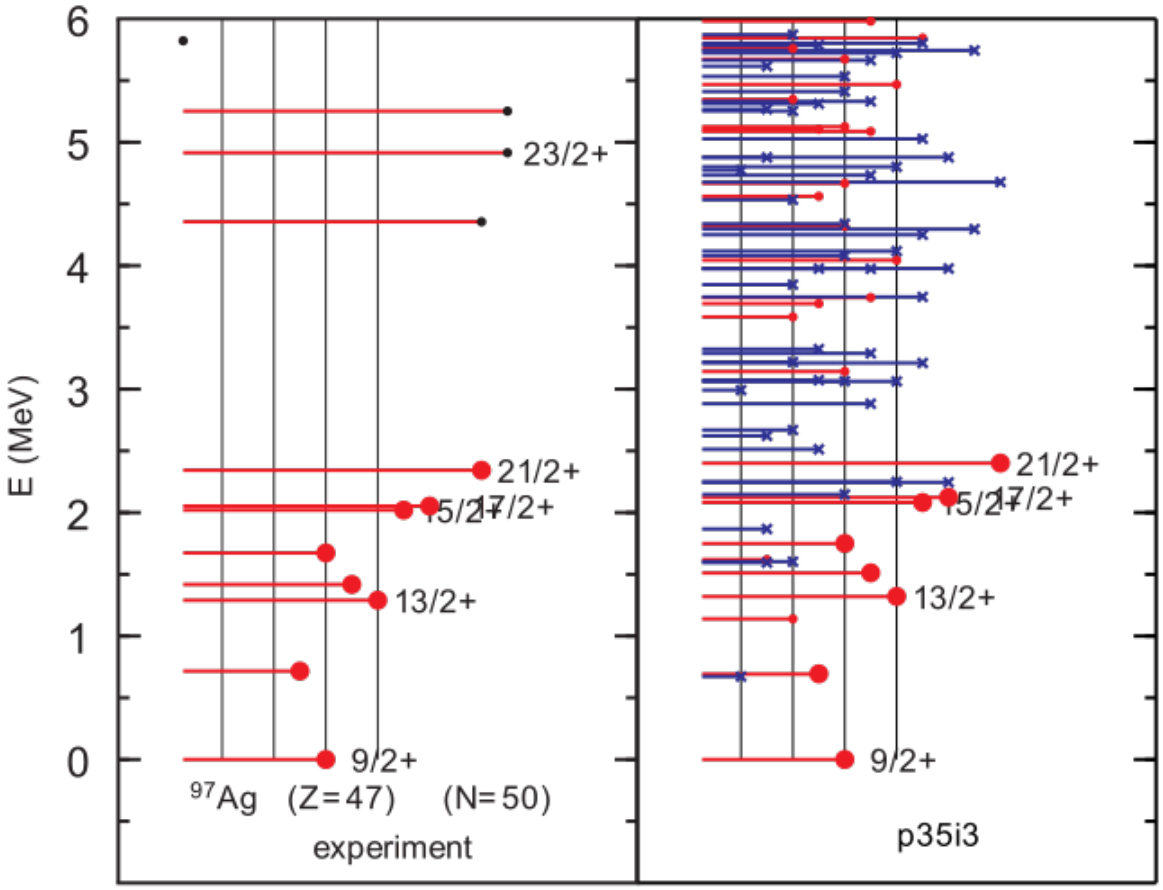

Figure A19 Energy Spectrum of ^{97}Ag.

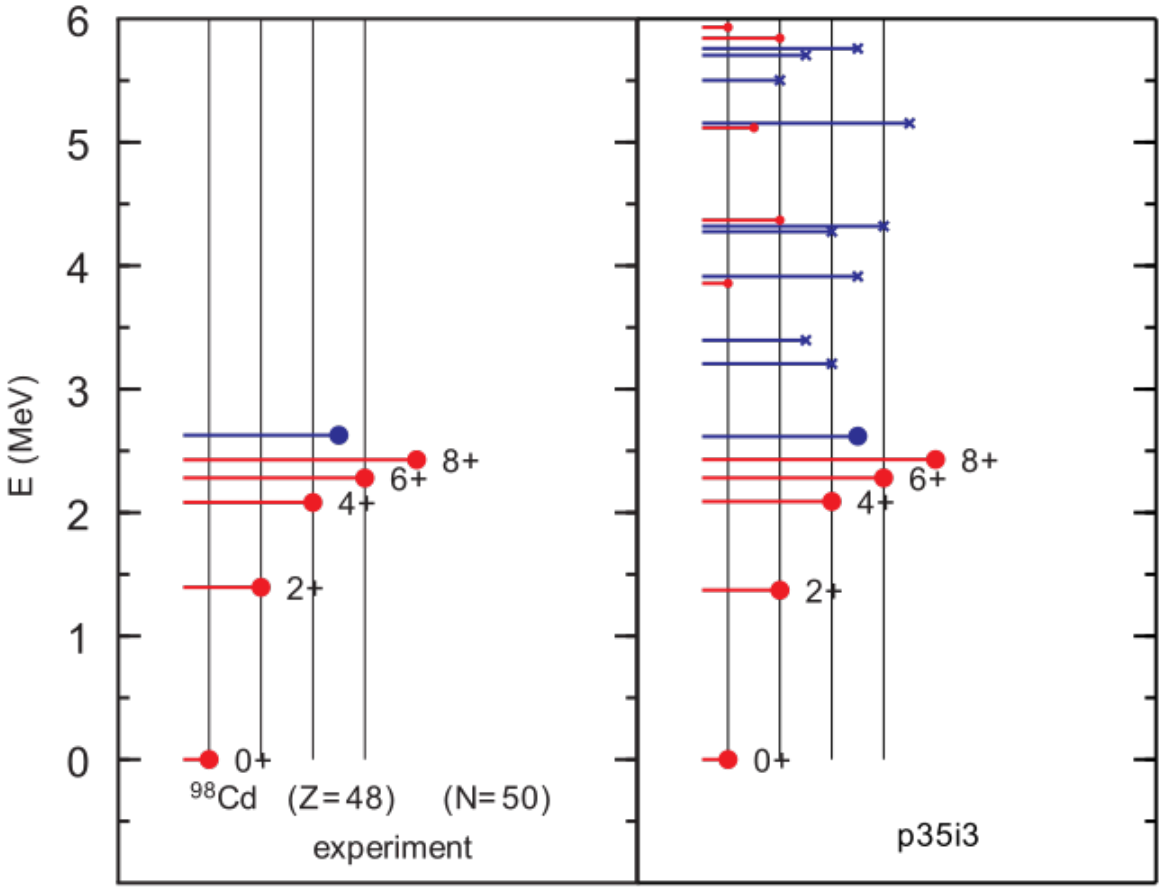

Figure A20 Energy Spectrum of ^{98}Cd.

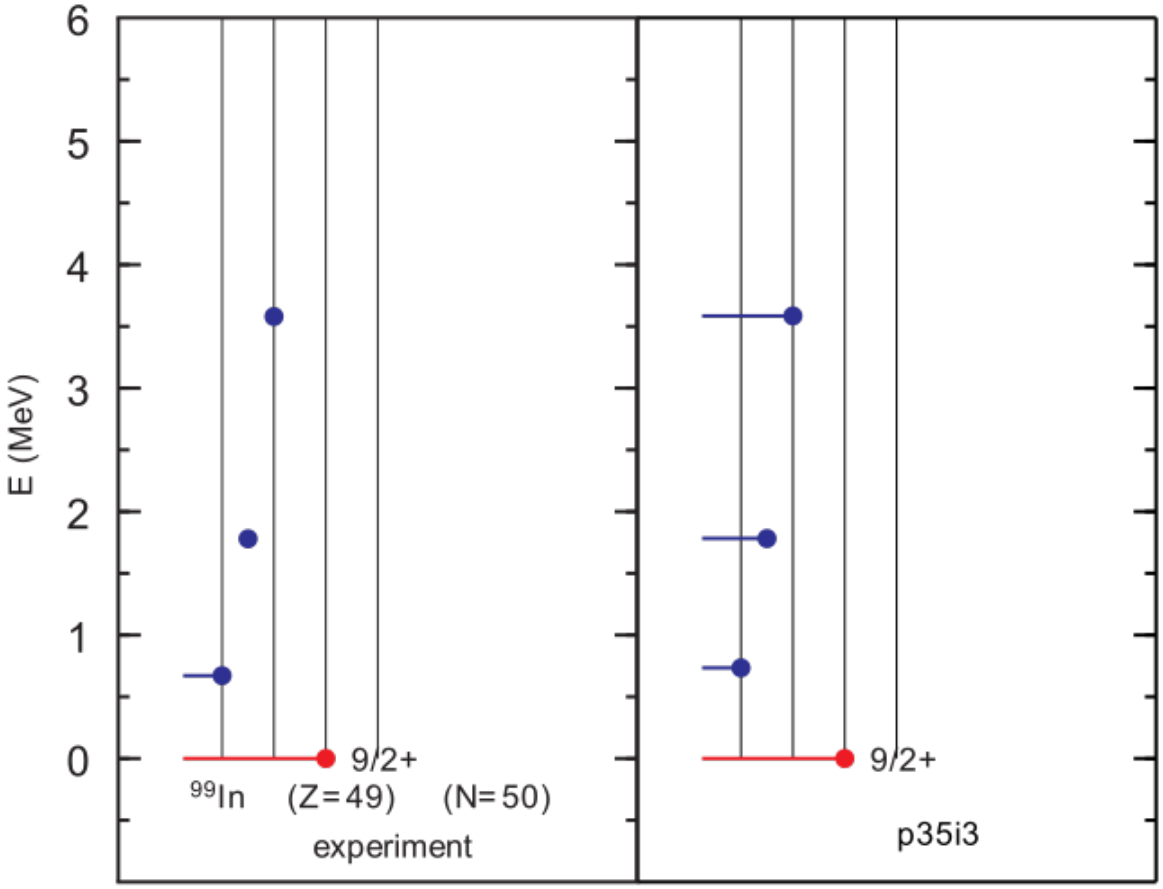

Figure A21 Energy Spectrum of ^{99}In.

APPENDIX B

ELECTROMAGNETIC OBSERVABLES EXAMPLE OUTPUT

Shown below is an example of an output set of calculations for the electromagnetic properties of ^{81}Ga. At the top of the file are the input specifics for the calculation, including the model space (n50), the effective interaction (p35-i3), effective charges and g-factors for protons and neutrons, and the potential used in calculation of radial matrix elements (skx). Below, the specific information pertaining to each state is shown, including the energy of the i'th state E_i, the spin J_i, the order of occurrence for that spin n_i, the half-life in picoseconds $T_{1/2}$, the decay width energy, and the electromagnetic moments of that state. Below each of these values for an initial state i are the details of decay to all possible final states f. The ground state has no decay channels, but if we look at the $n_i = 2$ state of $J^\pi = 3/2^-$ with 616 keV, we see that it can decay to the $n_i = 1$ lower $3/2^-$ state and the ground state with $J^\pi = 5/2^-$. Below the $T_{1/2}$ value of the 616 keV state we see the branching ratios (BR) to each of the final states, and we see in this example that the stronger branching ratio is to the $n_f = 1$ state with $J^\pi = 3/2^-$ with $\sim 74\%$. Below the width column we see the energy difference E_g between the initial and final states. Finally we see the $B(M1)$ under the $M1$ moment column and the $B(E2)$ under the Q moment column for each transition. The units for each number are given under the heading of each column at the top of the file. This output is cut off at 2 MeV for brevity and illustrative purposes. In general the cutoff energy can be extended for these files, and we have a .deo file for all nuclei in the $\pi j4$ model space. All of the predictions in this work which were presented from p35-i2, p35-3, jj44a, and n50j Hamiltonians were extracted from these .deo files.

---

gamma decay, moments for ga81 states up to 2 MeV

! model space = n50

! interaction = p35-i3

! e_p = 1.800 e_n = 0.800 E2

! g_sp = 4.694 g_sn = -3.826 M1 spin

! g_lp = 1.100 g_ln = 0.000 M1 orbital

! type of potential = skx

Ei (MeV)	Ji	ni	T_(1/2) (psec)	width (eV)	M1 moment (u_N)	Q moment (e^2 fm^2)
0.000	5/2-	1	0.000000	0.0000E+00	1.32829	-3.09
0.393	3/2-	1	0.2917E+03	0.1563E-05	2.8314	-9.79

Ef	Jf	nf	BR	Eg	del	B(M1)	B(E2)
0.000	5/2-	1	100.0000	0.393	0.42	0.1895E-02	0.3053E+02

Ei (MeV)	Ji	ni	T_(1/2) (psec)	width (eV)	M1 moment (u_N)	Q moment (e^2 fm^2)
0.616	3/2-	2	5.763536	0.7913E-04	1.53301	9.44

Ef	Jf	nf	BR	Eg	del	B(M1)	B(E2)
0.000	5/2-	1	25.8982	0.616	-3.26	0.6495E-03	0.2620E+03
0.393	3/2-	1	74.1018	0.223	-0.02	0.4563E+00	0.4624E+02

Ei (MeV)	Ji	ni	T_(1/2) (psec)	width (eV)	M1 moment (u_N)	Q moment (e^2 fm^2)
1.346	1/2-	1	0.049113	0.9287E-02	-0.27205	0.00

Ef	Jf	nf	BR	Eg	del	B(M1)	B(E2)
0.000	5/2-	1	0.0011	1.346	999.00	0.0000E+00	0.2974E-01

	0.393	3/2-	1	99.9943	0.953	0.16	0.9032E+00	0.3634E+03
	0.616	3/2-	2	0.0045	0.730	-0.55	0.7128E-04	0.5886E+00
1.382	7/2-	1		1.028164	0.4436E-03		3.92020	-18.16
	Ef	Jf	nf	BR	Eg	del	B(M1)	B(E2)
	0.000	5/2-	1	75.0663	1.382	-1.36	0.3811E-02	0.5325E+02
	0.393	3/2-	1	24.5331	0.989	999.00	0.0000E+00	0.1426E+03
	0.616	3/2-	2	0.4006	0.766	999.00	0.0000E+00	0.8356E+01
1.416	9/2-	1		1.148706	0.3970E-03		2.56298	-6.39
	Ef	Jf	nf	BR	Eg	del	B(M1)	B(E2)
	0.000	5/2-	1	99.9997	1.416	999.00	0.0000E+00	0.8649E+02
	1.382	7/2-	1	0.0003	0.034	-0.01	0.3031E-02	0.2777E+01
1.532	1/2-	2		0.025266	0.1805E-01		-0.21724	0.00
	Ef	Jf	nf	BR	Eg	del	B(M1)	B(E2)
	0.000	5/2-	1	4.4644	1.532	999.00	0.0000E+00	0.1184E+03
	0.393	3/2-	1	67.4908	1.139	0.01	0.7116E+00	0.1078E+01
	0.616	3/2-	2	28.0448	0.916	0.03	0.5682E+00	0.7129E+01
	1.346	1/2-	1	0.0000	0.186	0.00	0.5111E-04	0.0000E+00
1.827	5/2-	2		0.281366	0.1621E-02		3.41712	7.04
	Ef	Jf	nf	BR	Eg	del	B(M1)	B(E2)

0.000	5/2-	1	14.9232	1.827	5.31	0.1172E-03	0.1423E+02
0.393	3/2-	1	11.2506	1.434	1.52	0.1611E-02	0.2604E+02
0.616	3/2-	2	53.5288	1.211	-0.59	0.3119E-01	0.1076E+03
1.346	1/2-	1	0.0106	0.481	999.00	0.0000E+00	0.8263E+01
1.382	7/2-	1	20.2851	0.445	-0.06	0.3211E+00	0.7385E+02
1.416	9/2-	1	0.0001	0.411	999.00	0.0000E+00	0.9275E-01
1.532	1/2-	2	0.0017	0.295	999.00	0.0000E+00	0.1537E+02

1.938	11/2-	1	16.042120	0.2843E-04	5.62495	-27.55

Ef	Jf	nf	BR	Eg	del	B(M1)	B(E2)
1.382	7/2-	1	27.0495	0.556	999.00	0.0000E+00	0.1795E+03
1.416	9/2-	1	72.9505	0.522	0.17	0.1224E-01	0.1848E+02

1.966	3/2-	3	0.123705	0.3687E-02	1.03443	10.02

Ef	Jf	nf	BR	Eg	del	B(M1)	B(E2)
0.000	5/2-	1	5.9511	1.966	2.82	0.2787E-03	0.8228E+01
0.393	3/2-	1	19.8661	1.573	-3.02	0.1604E-02	0.8501E+02
0.616	3/2-	2	53.7028	1.350	0.21	0.6659E-01	0.2269E+02
1.346	1/2-	1	16.8504	0.620	0.03	0.2248E+00	0.9376E+01
1.382	7/2-	1	0.0794	0.584	999.00	0.0000E+00	0.5344E+02
1.532	1/2-	2	2.3188	0.434	0.09	0.8961E-01	0.5112E+02
1.827	5/2-	2	1.2314	0.139	-0.00	0.1459E+01	0.1744E+01